INAUGURAL DISSERTATION

zur

Erlangung der Doktorwürde

der

Naturwissenschaftlich–Mathematischen

Gesamtfakultät

der

Ruprecht–Karls–Universität

Heidelberg

vorgelegt von

Dipl.-Phys. Christoph Gund

aus Heidelberg

Tag der mündlichen Prüfung: 2. Mai 2000

Das sechsfach segmentierte MINIBALL Modul
Simulation und Experiment

Gutachter : Prof. Dr. Dirk Schwalm
Prof. Dr. Dietrich Pelte

Dissertation
submitted to the
Combined Faculties for the Natural Sciences and for Mathematics
of the
Rupertus Carola University of
Heidelberg, Germany
for the degree of
Doctor of Natural Sciences

The 6-fold Segmented MINIBALL Module Simulation and Experiment

presented by
Diplom-Physicist : Christoph Gund
born in : Heidelberg, Germany

Heidelberg, 2. May 2000
Referees : Prof. Dr. Dirk Schwalm
Prof. Dr. Dietrich Pelte

Abstract

Das Sechsfach Segmentierte MINIBALL Modul – Simulation und Experiment

MINIBALL, das neue Gammaspektrometer für REX-ISOLDE und andere Experimente mit radioaktiven Strahlen besteht aus 42 gekapselten, sechsfach segmentierten Germaniummodulen vom EUROBALL-Typ. Je drei Module sind in einem Kryostaten zusammengefaßt (3-Cluster). Durch die hohe Effizienz des Spektrometers wird Gammaspektroskopie bei niedrigen Strahlintensitäten erst möglich. Aufgrund der hohen Granularität erreicht man trotz der großen Geschwindigkeit, bei der die γ-Quanten abgestrahlt werden, eine gute Energieauflösung der dopplerkorrigierten Linien.

Die physikalischen Grenzen der Detektorgranularität wurden in detaillierten Simulationen mittels Pulsformanalyse der Vorverstärkersignale und anhand der Energieverteilung in den Segmenten untersucht. Algorithmen zur Bestimmung des Eintrittspunktes des γ-Quants in den Detektor wurden entwickelt. Besondere Aufmerksamkeit kam dabei der Anwendung dieser Algorithmen auf den 3-Cluster zu. Eine Ortsauflösung des Eintrittspunkts des γ-Quants von 10 mm$\times$10 mm wurde erzielt und experimentell bestätigt. Aus der Ortsauflösung wurden Vorhersagen über die erreichbare Energieauflösung von dopplerkorrigierten Linien abgeleitet.

In einem Testexperiment wurden die Probleme bei Experimenten mit niedriger Strahlintensität und inverser Kinematik untersucht. Der Einsatz von MINIBALL Modulen und dem REX-ISOLDE PPAC erlaubte es, diese Probleme zu lösen und eine gute Energieauflösung und Untergrundreduktion zu erzielen.

The Sixfold Segmented MINIBALL Module – Simulation and Experiment

MINIBALL, the new γ-ray spectrometer for REX-ISOLDE and other radioactive beam experiments consists of 42 encapsulated, six-fold segmented germanium modules of the EUROBALL geometry, clustered in cryostats of three modules (3-Cluster). The high full-energy-peak efficiency of the spectrometer allows γ-ray spectroscopy of low intensity beams, the high granularity permits a good energy resolution after Doppler correction, in spite of the high velocity of the γ-emitting reaction products.

Detailed simulations were performed to investigate the physical limits of the detector granularity using the segment energies and pulse-shape analysis. Algorithms to locate the γ-ray entry point into the detector were developed. Special attention was paid to the application of these algorithms to the 3-Cluster detector. A position resolution of the γ-ray entry point of 10 mm$\times$10 mm was obtained and experimentally verified. Finally predictions for the energy resolution after Doppler correction were deduced.

An experiment was performed to investigate the problems of low-intensity experiments in inverse kinematics. The use of the MINIBALL germanium modules in conjunction with the REX-ISOLDE PPAC allowed to solve these problems, a good energy resolution and a significant background suppresion could be achieved.

Contents

List of Figures

List of Tables

List of Symbols

ADC	analog-to-digital converter
addback	the addback factor is the enhancement factor of the FEP efficiency of a Cluster detector due to inter-module-scattering FEEs
(Alg.1)	$\log(\frac{\lvert q_- \rvert_{\max}}{\lvert q_+ \rvert_{\max}})$ algorithm for angular refinement
(Alg.2)	$\log(\frac{\lvert q_\pm \rvert_{\max}}{q_{\mathrm{seg}}})$ algorithm for angular refinement
CFD	constant fraction discriminator
D	distance between an interaction and the centreline of the core hole of the germanium module
D_1	distance between the first interaction and the centreline of the core hole of the germanium module
DSP	digital signal processor
E_γ	energy of a γ-ray
$\mathrm{E}_{\gamma-\mathrm{lab}}$	γ-ray energy in the laboratory system
$\mathrm{E}_{\gamma-0}$	γ-ray energy in the system of the γ-emitting nucleus
FEE	full-energy event
FEP	full-energy peak
FET	field effect transistor
FIFO	first-in first-out memory
FPGA	field programmable gate array
FWHM	full-width at half maximum
HPGe	high purity germanium
$\mathrm{J}^\pi_\mathrm{n}$	n-th excited level of a nucleus with a spin J and a parity π
MA	main amplifier
NSE	neighbouring two-segment event
OSE	one-segment event
PPAC	parallel plate avalanche counter
pps	particles per second

PSA	pulse-shape analysis
Q	Q-value of the nuclear reaction
q_-	charge pulse of the neighbour segment with the lower index
q_+	charge pulse of the neighbour segment with the higher index
q_{seg}	charge pulse of the entry/reference segment
R	radius coordinate in the germanium module (R,ϕ,z)
R_0	γ-ray entry radius
R_1	first interaction radius
R_{ref}	radius coordinate of the point, where the γ-direction intersects the reference plane z=z_{ref}
R_{main}	main interaction radius
T_{slope}	Time to steepest slope
TDC	time-to-digital converter
TFA	timing filter amplifier
z	depth coordinate in the germanium module (R,ϕ,z)
z_1	first interaction depth
$\langle z_1 \rangle$	mean first interaction depth
z_{ref}	reference depth in the germanium module
σ	total cross section
$\frac{\mathrm{d}\sigma}{\mathrm{d}\Omega}$	differential cross section
ϑ	absolute azimuth angle measured with respect to the beam axis
ϑ_{cm}	absolute angle in the c.m. system
ϑ_{lab}	absolute angle in the laboratory system
θ_γ	relative angle between the direction of γ-emission and the flight direction of the nucleus
ϕ	absolute polar angle measured with respect to the beam axis
ϕ	angle coordinate in the germanium module (R,ϕ,z)
ϕ_0	angle coordinate of the point where the γ-direction intersects the detector frontal plane
ϕ_1	first interaction angle

ϕ_{ref}	angle coordinate of the point, where the γ-direction intersects the reference plane $z{=}z_{\mathrm{ref}}$
ϕ_{coarse}	angle coordinate obtained from the basic angle assignment algorithm
ϕ_{fine}	angle coordinate obtained from an angle refinement algorithm
ϕ(MaxSeg)	segment angle of the segment with the maximum energy deposition
ϕ(Segline)	angle of the segmentation line between two neighbouring segments
weighted ϕ(Segline)	energy weighted mean value of the two segment angles of two neighbouring segments

Chapter 1

Introduction

Our understanding of nuclear structure as we know it today is largely based on a limited set of nuclei – those near the valley of stability and, to a certain extent, the proton rich nuclei. However there are theoretical reasons (and emerging experimental evidence) to suspect that nuclei can be far different entities far away from stability. The exploration of the nuclear landscape far-off the valley of stability has therefore become the paramount challenge for nuclear physics. The key themes of this research with exotic nuclei are *the nature of nucleonic matter* and *the origin of the elements*.

The study of nucleonic matter is a fundamental facet of our search to understand the universe. The investigation of unstable nuclei embraces many new aspects of this quest. It focuses on the exotic properties of loosely-bound quantum systems, often with new geometries, such as nuclei with giant halos or skins of neutron matter, and on regions of nuclei with special structure and symmetries. We expect to encounter new phases of nuclei such as new shell structures and new collective modes. The ultimate goal is the understanding of the nucleus as a finite many-body system. Nuclei far from stability are crucial to this endeavor since they allow us to amplify and isolate particular aspects of the interactions between nucleons, like shell closures, the deformation of nuclei, and proton-neutron pairing.

Exotic nuclei have an enormous astrophysical relevance. They are mainly produced in cataclysmic stellar explosion like supernovae, but decay immediately afterwards. Many of the nuclear reactions in stellar environments, particularly in violent explosive events, involve proton and neutron capture processes that are

sensitive to both the structure of the unstable nuclei involved and to the temperatures, densities, and time-scales of such events. Thorough knowledge of exotic nuclei would thus connote a remarkable improvement for our understanding of the synthesis of the elements and the nature of the stars and their evolution as well [Käp98].

Nuclear physics research with exotic isotopes requires new experimental techniques and facilities. As such nuclei decay within less than a minute, it is impossible to produce targets with exotic nuclei. In consequence nuclear physics experiments with nuclei far-off stability always implies experiments with radioactive beams. The production of exotic nuclei happens in a fragmentation or a fission reaction. A heavy nucleus and a light nucleus collide and the fragments of the heavy nucleus are used for the production of the secondary radioactive beams. There are two main principles to produce such radioactive beams:

In fragment-separator (FRS) facilities like the FRS at GSI[1] heavy nuclei – usually lead or uranium – are accelerated to relativistic energies of 300 MeV$\cdot A$ corresponding to a velocity of $\beta = \frac{v}{c} \approx 0.65$. Very thick production targets ($\sim$g/cm^2) of a light material – typically beryllium – are used for the fragmentation reaction and a beam containing various kinds of fragment nuclei is obtained. With the aid of a fragment separator one or more (cocktail beam) desired exotic nuclei can be extracted. Depending on the selected element and isotope very low secondary beam intensities of only a few particles per second may be encountered. The high energy of the primary beam ensures that the secondary beam is still relativistic, yet a substantial energy spread and considerable scattering of the beam particles is encountered. The high velocity of the secondary beam allows to investigate isotopes of any desired element with a lifetime down to below 1 μs and permits the use of extremely thick reaction targets, so that sufficient reaction rates can be ensured even for extremely low beam intensities.

For fragment-separation experiments the detection of the beam particle in front of the target and behind is customary, permitting the particle identification by measuring the time of flight and the energy loss in the particle detectors. This method is compulsory for experiments with cocktail beams. The high beam velocity and the large energy spread impede particle spectroscopy and require an

[1] Gesellschaft für Schwerionenforschung, Darmstadt

adapted experimental setup for γ-ray spectroscopy. As the emitted γ-rays are strongly Doppler shifted and the energy spread only allows a moderate energy resolution, high efficiency scintillator materials like NaI are mainly used as γ-ray detectors at FRS facilities.

The second kind of facility to produce radioactive beams is an isotope separator facility (Isotope Separator OnLine, ISOL). Here massive targets made of heavy material – e.g. lead or uranium – are bombarded by light nuclei such as 1 GeV protons. As an example for such a facility REX-ISOLDE[2], the radioactive beam experiment at the isotope separator facility at CERN[3] (ISOLDE), which is scheduled to start operation in summer 2000, will be described, since the nuclear physics group at MPI-K[4] is strongly involved in the development and construction of this facility.

The heavy nuclei break into fragments, which diffuse out of the target and are stripped off one electron, accelerated to 60 keV, and separated in a mass-separator. The time needed for this process limits the nuclei available in ISOL facilities to those with a decay time of more than $\sim$10 ms. Furthermore some elements are not available at all as their diffusion out of the target is inhibited.

In REX-ISOLDE the exotic nuclei available from the separator are then accumulated in a trap, charge breeded in an EBIS[5], and finally accelerated to energies of up to 2.2 MeV$\cdot A$ ($\beta = \frac{v}{c} = 6.8\%$). Even higher energies of up to 5 MeV$\cdot A$ ($\beta = 10\%$) are planned for future experiments. Unlike fragment separator facilities ISOL facilities provide high quality beams with a very low energy spread and a sharp focus, so that in principle all spectroscopic tools developed for nuclear physics experiments with stable beams can be applied. But in contrast to stable beam experiments, where the beam intensity is usually limited by the maximum data acquisition rate of the experiment itself, one of the biggest problems of measurements with radioactive beams are the low beam intensities. At REX-ISOLDE stable elements will be available with beam intensities of up to 10^{10} beam particles per second. These intensities decline by a factor of $\approx$20 for

[2]Radioactive beam experiment at ISOLDE

[3]Centre Européen pour la Recherche Nucléaire

[4]Max-Planck-Institut für Kernphysik, Heidelberg

[5]Electron beam ion source

every nucleon step away from the valley of stability. As an example the search for the N=20 shell closure in sodium isotopes is presented: While ^{24}Na with only one excess neutron is produced with a rate of $5.5{\cdot}10^{8}\mathrm{s}^{-1}$, the possible shell closure element ^{31}Na is only produced with a rate of 66 s^{-1}.

The extremely low beam intensities expected for the most exotic nuclei require an experimental setup optimized to achieve both high reaction rates and high detection efficiency without compromising resolution. High resolution particle spectroscopy provides neither high reaction rates nor a high detection efficiency, as very thin targets and high resolution spectrometers, which have a small angular acceptance, are required.

In contrast, γ-ray spectroscopy with a highly efficient detector array offers the possibility to use relatively thick targets (in comparison with targets for particle spectroscopy), while maintaining excellent resolution. However due to the high velocities of the reaction products, a highly granular detector array is needed in order to avoid a loss of resolution due to Doppler broadening.

The stringent efficiency and granularity requirements for γ-ray detectors used in radioactive beam experiments could not be satisfied by standard detector technology. Hence the MINIBALL project [Ebe97] was started in 1995. The aim of this project was the development of a germanium detector array ideally suited for γ-ray spectroscopy at ISOL facilities with a beam velocity of up to $\beta{\approx}0.1$.

In experiments with extremely low beam intensities it is usually difficult to do γ-ray spectroscopy with nuclear reactions, as background γ-rays detected in the detector array may outnumber the nuclear-reaction γ-rays by orders of magnitude. This problem becomes even more pronounced when the exotic beams used are stopped close to the target, as they will produce additional background due to their radioactive decay. It is therefore important to create a signal indicating that a reaction has taken place and to use a time coincidence to achieve a sufficient background suppression. In order not to compromise the high beam quality of REX-ISOLDE, the beam particle should not be detected before it reaches the target. It is therefore more favourable to detect a reaction product behind the target to obtain the desired signal.

In order to achieve an optimized particle detection, the kinematics of the reaction products, which are in return determined by the reaction mechanism, have

to be known. At REX-ISOLDE mainly Coulomb excitation and inverse transfer reactions on light target materials will be used to investigate the collective and single-particle structure of low-lying levels of nuclei with an extreme N/Z-ratio.
In Coulomb excitation experiments the target materials must have a high Z to prevent the nuclei from interacting strongly. Here the excitation of the nucleus stems exclusively from the electromagnetic interaction, which probes mainly the collective properties of the nuclei. As a consequence of the relatively high mass of the target material the excited nucleus can be scattered by large angles. In order to reconstruct the kinematics of such a reaction for Doppler correction, a particle detector measuring the flight direction of the γ-emitting nucleus and covering a large fraction of the solid angle is needed. This detector will also provide the reaction trigger.
Transfer reactions on light target materials are especially sensitive to the single-particle structure of the transfer nucleus. Due to the light target nucleus the transfer nucleus is scattered only by small angles (in contrast to Coulomb excitation), while the light reaction product is usually scattered by large angles. Here a particle detector in forward direction, which covers only a small fraction of the full solid angle, is sufficient as the reaction trigger. In order to avoid excess background γ-rays from β-decay the areal density of this detector must be sufficiently low, so that the beam particles are not stopped in the detector.

This thesis deals with the development and simulation of the MINIBALL γ-array and a feasibility study for transfer experiments at ISOL facilities like REX-ISOLDE.
In the next chapter, the MINIBALL project is presented in detail. The geometry of the detector crystal and the cryostat is shown and possible detector arrangements are discussed. The electronics to fully exploit the information contained in the detector pulses are depicted.
The third chapter is dedicated to the basic principles of germanium detector functioning. The different steps from the interaction of the photon with matter to the production of the detector pulse are reviewed. The simulation techniques needed to calculate pulses are introduced.
In the fourth chapter the detector principles of the preceding chapter are used for

quantitative simulations. The chapter starts with basic properties like detector efficiency, then the physical limitations for the best achievable granularity are discussed. Furthermore the position resolution which can be obtained by segmentation and pulse shape analysis is presented. Finally algorithms to improve the detector granularity are explained and used to calculate the expected energy resolution after the Doppler correction. Whenever possible, simulated quantities are compared with their experimental counterparts.

The feasibility of transfer experiments at REX-ISOLDE is discussed in the fifth chapter. A neutron transfer experiment with a stable beam (adjusted to the beam currents expected at REX-ISOLDE) has been performed to test modules of the MINIBALL germanium array and the new REX-ISOLDE PPAC[6]. Various aspects of the experiment like Doppler correction, background reduction, reaction kinematics, selection of the reaction channel, and expected cross-sections are examined.

The final chapter summarizes the results of this work. Consequences for future experiments are discussed.

[6]Parallel Plate Avalanche Counter

Chapter 2

MINIBALL – a High-Efficiency High-Granularity Germanium Detector Array

In this chapter the MINIBALL project will be presented. Specifications will be deduced from requirements of radioactive beam experiments, then the properties of a single detector module and the 3-module cryostat will be described. Finally the operation of the electronics will be depicted.

2.1 The MINIBALL Specifications

In radioactive beam experiments mainly low-lying levels of exotic nuclei will be studied, so that the γ-array does not have to cope with high multiplicity γ-cascades. It is therefore possible to achieve a high efficiency by placing the germanium detectors very close to the target resulting in a considerable cost reduction per percent efficiency, as only a small number of germanium modules is required. Yet the close geometry has an important disadvantage. The large recoil velocities of the reaction products cause a considerable Doppler broadening, and the width of a Doppler broadened peak grows with the solid angle covered by a single detector module. Internal segmentation of the modules is the best remedy for this problem which does not sacrifice full-energy-peak efficiency[1] while keeping costs low. Based on the experience with the EUROBALL Cluster modules

[1]The full-energy-peak efficiency is the probability that the total energy of a γ-ray, which is isotropically emitted into a solid angle of 4π, is recorded in one or more detectors of the germanium array.

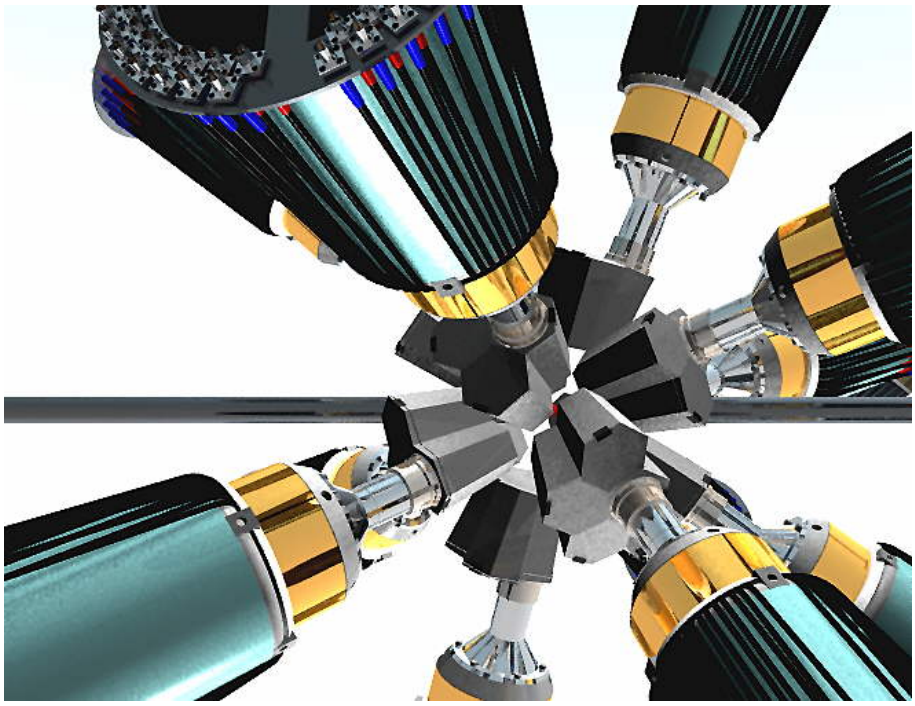

Figure 2.1: The high efficiency setup of the MINIBALL array. The end-caps of the cryostats, which are filled with three or four modules, point at the target position. The supporting frame, which carries the cryostats is omitted. (Courtesy of Universität zu Köln)

[Tho95] a two-fold segmented prototype detector was commissioned at EURISYS MESURES and delivered in late 1995. The results of the tests with this prototype detector [Gun97] were used to develop the six-fold segmentation for the MINIBALL modules. The experience with the first six-fold segmented prototype [Fis97] resulted in further improvement of the encapsulation technique. Finally the MINIBALL collaboration[2] agreed on the following specifications for the MINIBALL array:

[2]Collaborating Institutes: Institut für Kernphysik der Universität zu Köln (IKP), Institut für Kern- und Teilchenphysik der Ludwig-Maximilians-Universität München, Institut für Kern- und Strahlungsphysik der Katholischen Universität Leuven, Max-Planck-Institut für Kernphysik - Heidelberg (MPI-K), Gesellschaft für Schwerionenforschung - Darmstadt, Centre Européen pour la Recherche Nucleaire - Genf (CERN), II. Physikalisches Institut der Universität Göttingen, Institut für Kernphysik der Forschungsanstalt Jülich, Institut für Kernphysik der Technischen Universität Darmstadt, Institut Laue Langevin - Grenoble (ILL), Institut de Recherches Subatomiques - Straßburg (IReS), Daresbury Laboratory.

- A full-energy-peak efficiency of >15% for a γ-energy of 1 MeV at the closest detector arrangement (10.6 cm distance to the target), which is shown in Figure 2.1, should be achieved.

- For beam velocities up to β=0.1 the Doppler-shift related contribution to the energy resolution should be kept below 1% of the energy of the γ-ray detected.

- For the MINIBALL modules the encapsulation technology and the semi-hexaconical shape of the EUROBALL Cluster modules [Tho95] should be employed, so that a combination with the standard EUROBALL Cluster modules remains possible. The length of the modules was therefore set to 78 mm, the diameter to 68 mm.

- In order to achieve sufficient granularity a six-fold segmentation of the outer contact had to be developed. Further granularity was to be gained by the use of sampling electronics and pulse-shape analysis.

- The complete MINIBALL should consist of 42 six-fold segmented detector modules.

- A LEGO-like system of different multiple-capsule cryostats was to be developed to achieve optimized setups for different experiments. The maximum number of modules in the cryostat was limited to four capsules in order to keep electronic crosstalk at a tolerable level, to obtain a weight below 50 kg and to achieve an acceptable alignment of the target direction and the modules' centrelines.

2.2 The MINIBALL Module

The shape of the MINIBALL crystal and capsule can be seen in Figure 2.2 and Figure 2.3, respectively. While the geometrical dimensions do not differ from the ones of the standard EUROBALL Cluster module [Tho95], an additional six-fold segmentation has been added to the MINIBALL modules. The semi-hexaconical shape of the crystal is a compromise between a cylinder with no material loss, but a poor coverage of the solid angle and a truncated pyramid with severe material

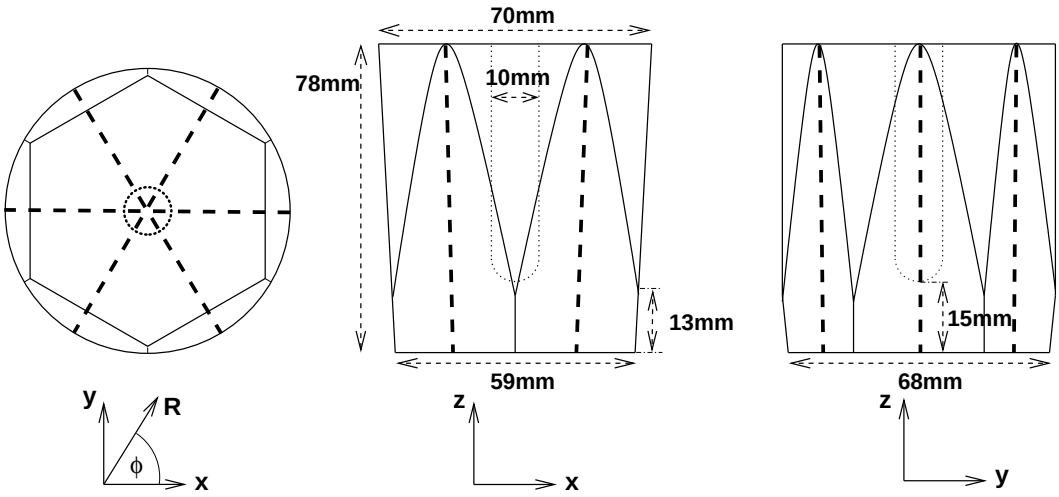

Figure 2.2: Geometry of the MINIBALL crystal. Visible lines are shown as solid lines, inner lines are dotted. The segmentation is depicted with dashed lines. The coordinates used in the text are illustrated (x,y,z,R,ϕ).

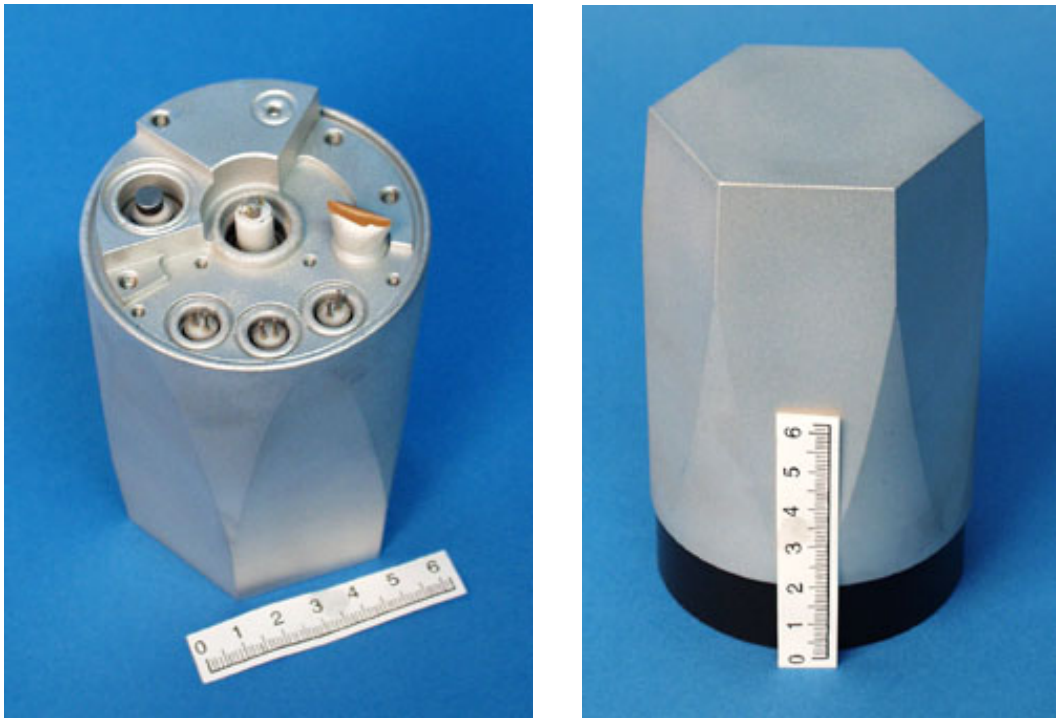

Figure 2.3: Pictures of the MINIBALL module. On the backside of the module (left) the central high voltage feed-through and three pairs of segment feed-throughs are visible. On the left side the electric actuator of the ion getter, on the right side the sealed vacuum flange can be found. The front side of the aluminium housing (right) is shaped in the same way as the crystal.

loss and a full coverage of the solid angle. With the semi-hexaconical shape the solid angle is fully covered by at least 13 mm germanium material depth and the loss of material is limited to 7%.
The shape of the EUROBALL Cluster modules was optimized for a target distance of 42 cm. This design distance was also kept for the MINIBALL modules. A change to a smaller distance was considered, but later dismissed for three reasons:

- The change to another shape would mean an increase of development costs and an additional material loss for each crystal.
- The reshaped crystals would not be compatible with the EUROBALL Cluster modules.
- MINIBALL was planned to be utilized at several target distances, so that the definition of an optimum target distance was hardly possible.

The MINIBALL modules are therefore germanium detectors optimized for the greatest flexibility. They are well suited for a wide variety of different experiments, even if not ideally suited for all of them.
The MINIBALL germanium modules are made of n-type high purity germanium (HPGe) with impurity concentrations between $5\times10^9\text{cm}^{-3}$ and $20\times10^9\text{cm}^{-3}$ [Gut96]. The impurity concentration is usually not constant, but exhibits a radial rise, caused by the crystal growing process. The impurity concentration and the size of the modules determine the high voltage needed to operate the germanium detector; for the MINIBALL modules positive voltages between 3 kV for low and 4.5 kV for high impurity concentrations have to be applied to the central electrode in order to obtain an optimum operation. At these voltages almost the full detector volume becomes sensitive to γ-ray irradiation.

2.3 The MINIBALL Cryostat

During the development phase of MINIBALL, the original idea to build cryostats for 7 individually encapsulated, six-fold segmented germanium detectors of the EUROBALL Cluster type [Tho95] was changed to cryostats containing only three or four crystals for several reasons:

Figure 2.4: The new MINIBALL 3-Cluster cryostat (asymmetric solution). (Courtesy of Universität zu Köln)

1. The geometry of 7 capsules caused problems for the Doppler-shift correction, as the centrelines of the outer capsules were strongly misaligned with respect to the target direction for detector target distances of ∼11 cm required for a 4π geometry.

2. Cryostats with fewer capsules offered a considerably greater flexibility to realize different array geometries.

3. It turned out to be extremely difficult to operate the 49 required preamplifiers in one cryostat.

4. The cryostat with 7 capsules would have had the same weight as the EUROBALL Cluster detector and would have been too heavy to be handled without a crane.

The reduction to smaller cryostats (Figure 2.4) was accompanied by a sacrifice of about 20% of the add-back factor (1.25 instead of 1.44 at 1.3 MeV for the three module cryostat), which will be discussed in more detail in Chapter 4.
As in the EUROBALL project the cryostat development has been done by the nuclear physics group at the Universität zu Köln. Each cryostat consists of the liquid nitrogen tank, the main cold finger, and an end-cap. At the moment the development of the triangular three-module end-cap is finished, the development of a double and a quadruple end-cap has started. The variety of end-caps will give an extra flexibility to achieve an optimum germanium setup for each experiment. A flexible holder frame has been developed at Köln and Straßburg, which allows for a multitude of germanium array setups. On one hand it is possible to have a high efficiency setup which covers a large fraction of the full solid angle ("4π-setup"), which can be seen in Figure 2.1. An efficiency of more than 15% for 1.3 MeV γ-rays is expected for such a setup from simulations. On the other hand it is possible to enlarge the target distance of the cryostats and concentrate the detectors at certain scattering angles. Such a setup permits an improved Doppler correction and is most suitable for angular distribution measurements. In the lifetime setup the germanium detectors are exclusively located close to the beam axis (0° and 180°), so that the flight peak and the stop peak can be easily separated.

2.4 The MINIBALL Electronics

For MINIBALL it was initially planned to use an improved version of the EUROBALL electronics, which was based on a VXI-bus system. Yet this kind of electronics did not offer pulse processing of both the core and the segment signals at an affordable price. In the initial design of these electronics only the core pulse could be fully processed, while an energy and a trigger signal were generated from the segment pulses. When it became obvious that it was also necessary to digitize the segment signals of the detector to achieve an optimized position resolution, the collaboration decided to follow a for high resolution purposes radically new approach.

In contrast to the initial VXI electronics, the new electronics derive all trigger, energy, and position information from the digitized preamplifier pulses of the core and the segments. The new Digital Gamma Finder card (DGF-C produced by X-ray Instrumentation Associates [XIA]) is a single-width fast-CAMAC module with four channels, which has been slightly modified to allow for operation in multi-detector experiments. Two modules are needed to process the signals of one MINIBALL crystal.

The relatively small analogue part of the core and one segment channel is shown in Figure 2.5. While the segment electrodes are directly connected to their respective contacts, a capacitor is needed to separate the signal from the central electrode from the detector high voltage. The current pulses produced on the contacts of the crystal are integrated in charge sensitive preamplifiers, which have been developed by the MPI-K in Heidelberg and the IKP in Köln, the preamplifier charge pulse is obtained. The preamplifiers are operated with a cold FET and a cold feedback circuit mounted directly on the capsule to obtain an optimum energy resolution, and a main board, which is operated at room temperature. They have been especially designed for MINIBALL and have a rise time of $\sim$40 ns (integration time $\sim$16 ns) and a decay time of 50 μs.

In order to avoid ghosts[3] the high frequency components of both the preamplifier signal and the noise are then eliminated by an anti-aliasing filter at the input

[3]When a signal is sampled, signal components above the Nyquist frequency ($f_{sampling}/2$) are transformed into signals below the Nyquist frequency, so that high frequency noise or interference can be transformed into a fake low frequency signal called a ghost.

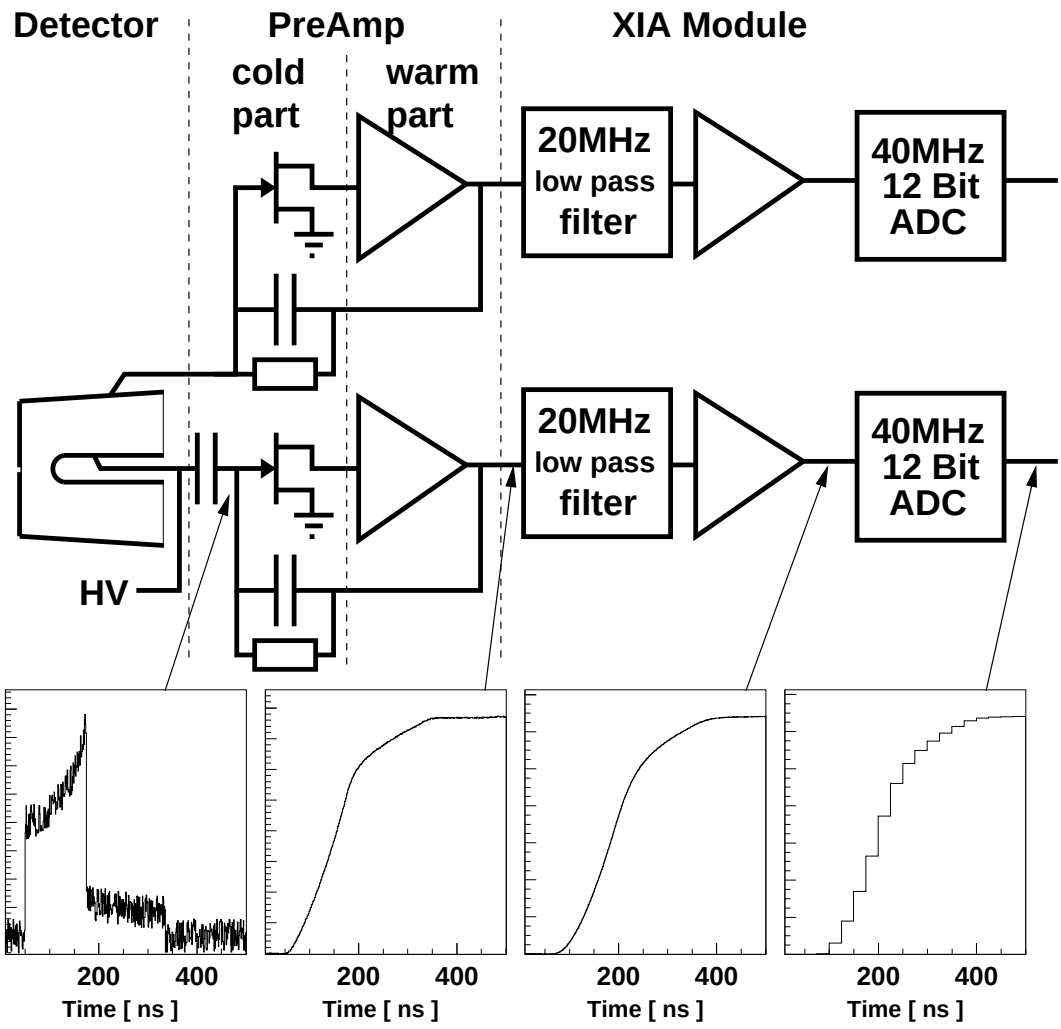

Figure 2.5: Analogue part of the MINIBALL electronics. The analogue signal path and the signals at the marked positions are shown.

The segment electrodes are directly connected to their respective contacts, a capacitor is needed to separate the signal of the central electrode from the detector high voltage. The current signals originating from the electrodes of the germanium crystal are amplified and integrated in their preamplifiers, the preamplifier charge pulse is obtained. The first transistor – a FET – and the feedback circuit of the preamplifier are mounted directly on the detector capsule and operated at liquid nitrogen temperature, so that the short signal paths and the low noise allow an optimized energy resolution. A 4th-order filter at the Nyquist frequency ($f_{sampling}/2$) blocks all signals above 20 MHz (anti-aliasing); a second amplifier adjusts the pulse height for the ADC and adds an offset when necessary. Every 25 nanoseconds the ADC provides a 12-bit wide sample of the pulse for digital processing. The detector crystals and the preamplifiers are mounted inside the cryostats; the filter, amplifier and ADC are part of the XIA Digital-Gamma-Finder module [XIA].

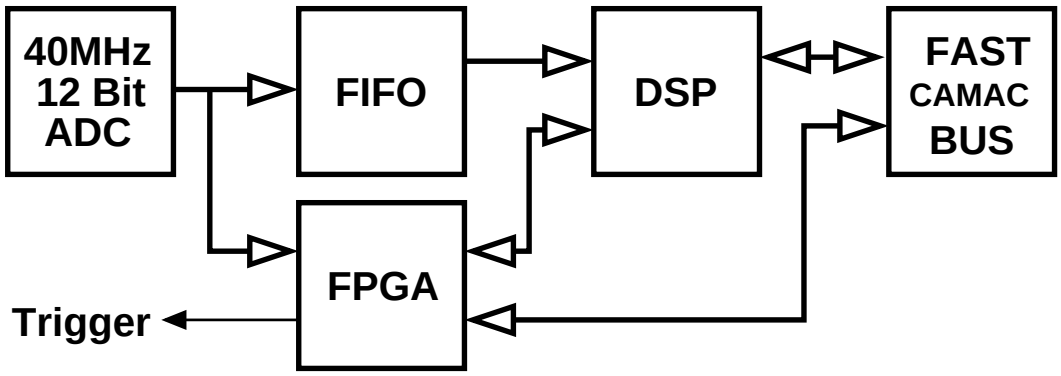

Figure 2.6: Digital part of the MINIBALL electronics.
In the digital part of the XIA module the 12-bit samples from the ADC are preprocessed and filtered in the FPGA. The trigger signal and the energy value are generated there. A FIFO makes the samples directly accessible for the DSP. Further information about the γ-ray detected is produced using both preprocessed and raw data. All information is read out via the fast-CAMAC bus.

of the XIA module. An amplifier is needed to adjust the pulse height to the dynamic range of the input of the ADC. Every 25 ns the ADC provides a 12-bit wide sample of the preamplifier charge pulse for digital processing, a set of these samples is called the ADC charge pulse.

The sampled signal from the ADC is then digitally shaped with two filters implemented in the FPGA[4] – see Figure 2.6. One filter is used to evaluate the energy of the pulse, which is then directly read out via CAMAC, the other one is needed to produce the fast trigger. Via a FIFO[5] the raw samples are also directly accessible for the DSP[6]. The DSP is needed both to control the signal flow and to implement further algorithms for the position resolution which do not fit into the FPGA.

The delivery of the XIA modules has started in autumn of 1999. The tests of the modules and the development of algorithms have not yet finished. At a high γ-energy of 1.3 MeV an energy resolution of better than 2.2 keV has been observed for the central contact, the segments have yielded values around 2.4 keV [Wei].

[4]Field Programmable Gate Array
[5]First In First Out Memory
[6]Digital Signal Processor

In this energy range comparable analogue standard electronics cannot match the energy resolution achieved with the XIA module (~2.3 keV). In the low energy range around 100 keV the energy resolution of the module cannot quite match its analogue counterpart (1.2 keV and 1.0 keV for the central contact).
While the energy resolution of the XIA module has already exceeded expectations, a strong effort will be needed to reach the timing resolution usually obtained from analogue electronics. The digital timing is sufficient for hardware trigger purposes, methods to obtain an improved timing resolution by interpolation of the pulse are currently under investigation.

Chapter 3

Pulse Production in Germanium γ-ray Detectors

3.1 Interactions of γ-rays with Matter

Unlike the detection of an ion in a semiconductor detector, where the ion produces a track of electron-hole pairs, the detection of a γ-ray in a semiconductor detector is a two-step process. The photon enters the detector and only eventually interacts with the material. In this interaction a fast electron, in a pair-production process also a fast positron, is released. These fast charged particles in return deposit their energy in the excitation of a large number of electron-hole pairs. Finally the electron-hole pairs can be electronically detected.
In the energy range between a few keV and several tens of MeV, which is the relevant energy range in nuclear physics experiments three different processes dominate the interaction of γ-rays with matter:

- In a **photoelectric absorption** process the photon interacts with an atom. The full energy E_γ is transferred to an electron, while the momentum is transferred to the atom. Due to the difference in mass the energy transfer to the atom is negligible. The kinetic energy E_{e^-} of the released electron is the difference between the γ-energy E_γ and the electron binding energy E_b.

  $$E_{e^-} = E_\gamma - E_b \tag{3.1}$$

  The remaining hole in the electron shell of the atom is filled successively by electrons from outer shells, whereupon either a characteristic X-ray, which is

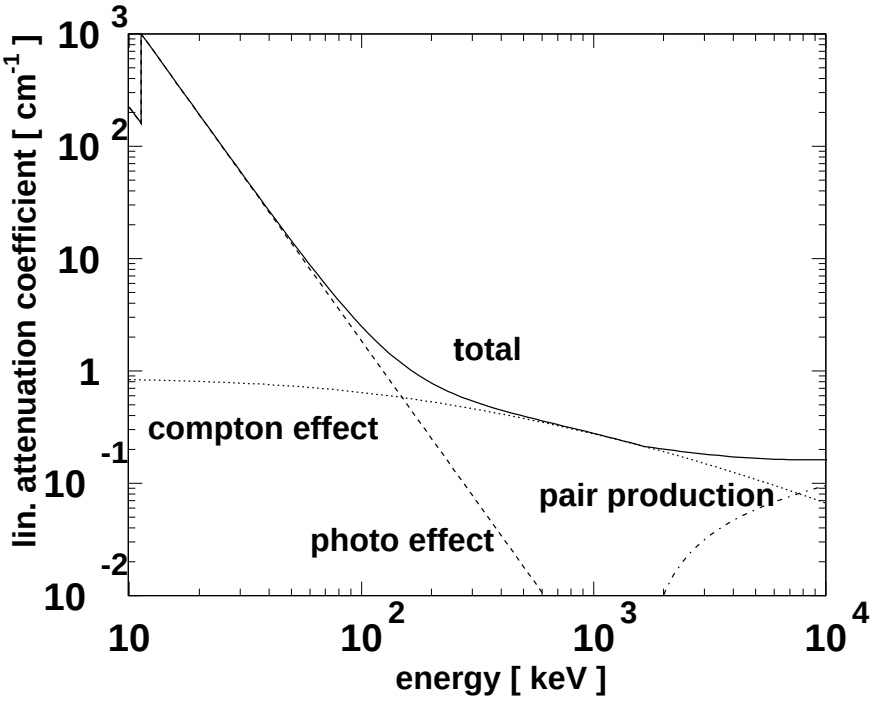

Figure 3.1: Linear attenuation coefficients of germanium. Redrawn from [Deb88].

immediately absorbed again by the photoelectric effect, or an Auger electron is emitted in order to conserve energy. As can be seen in Figure 3.1, the binding energy of the K-shell is located at 13 keV, where a step of the linear attenuation coefficient occurs. The photoelectric effect dominates the linear attenuation coefficient of germanium up to γ-energies of about 150 keV.

- In a **Compton** interaction the photon scatters elastically at an electron transferring only a part of its energy ΔE_γ. As before the binding energy E_b of the electron has to be overcome.

$$E_{e^-} = \Delta E_\gamma - E_b \tag{3.2}$$

Since the atom is not needed to assume the momentum, mainly the large number of electrons in the outer shells of the atom contribute to the Compton effect. As the Compton effect dominates the linear attenuation coefficient in the energy range between 150 keV and 2.5 MeV and the binding energy of the outer electrons only accounts for a few electronvolts, the binding energy can be neglected. Even the energy loss ΔE_γ is generally

significantly larger than the binding energy. Only for very small scattering angles ΔE_γ and E_b are of the same order of magnitude.

- In a **pair production** process the photon annihilates at a nucleus creating an electron-positron pair that shares the kinetic energy

$$E_{e^+} + E_{e^-} = E_\gamma - 2 \cdot m_e c^2. \tag{3.3}$$

Both charged particles are decelerated, subsequently the positron annihilates and two secondary γ-rays with an energy of 511 keV are produced. They are emitted in arbitrary opposing directions.

The fast electrons (positrons) produced in the interactions continuously deposit their energy in a large number of interactions with the detector material. Two different interaction processes exist.
As can be seen in Figure 3.2, impact ionisation dominates most of the energy range of the fast electrons created when a γ-ray interacts with matter. The specific mean energy loss is described by the Bethe-Bloch-formula [Sie65]

$$\begin{aligned} -\left(\frac{dE}{dx}\right)_e &= \frac{2\pi e^4 NZ}{c^2 m_e \beta^2}\left[\ln\frac{c^2 m_e \beta^2 E_{\text{kin}}}{2I^2(1-\beta^2)} - \ln 2 \cdot \left(2\sqrt{1-\beta^2} - 1 + \beta^2\right)\right. \\ &\quad \left. + \left(1-\beta^2\right) + \frac{1}{8}\left(1-\sqrt{1-\beta^2}\right)^2\right], \text{ with} \end{aligned} \tag{3.4}$$

N : number density of the detector material $\left[\frac{1}{cm^3}\right]$
Z : atomic number of the detector material (32 for germanium)
E_{kin} : electron kinetic energy
e : electron charge
m_e : electron rest mass
$\beta = \frac{v}{c}$: velocity of the electron in units of the speed of light
I : mean ionisation energy of a bound electron ($\approx$300 eV for germanium)

For highly relativistic electrons the radiative energy loss described in the Bremsstrahlung formula [Sie65] becomes relevant:

$$-\left(\frac{dE}{dx}\right)_e = \frac{N(E_{\text{kin}} + m_e c^2) Z(Z+1) e^4}{137 m_e^2 c^4}\left(4 \ln\frac{2(E_{\text{kin}} + m_e c^2)}{m_e c^2} - \frac{4}{3}\right). \tag{3.5}$$

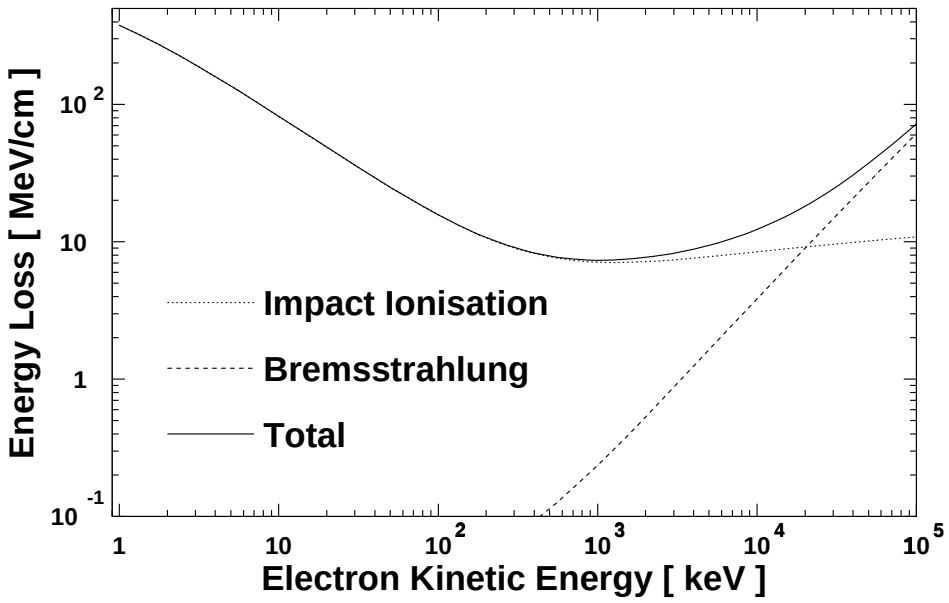

Figure 3.2: Energy loss of fast electrons in germanium. While impact ionisation (dotted line) dominates at lower energies, Bremsstrahlung (dashed line) is only important for highly relativistic electrons.

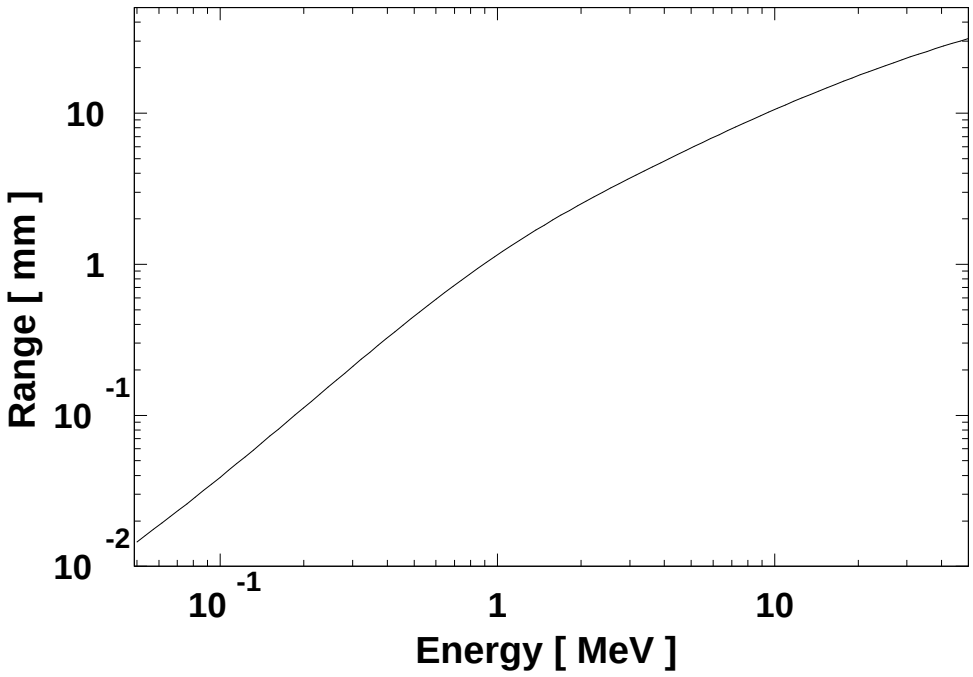

Figure 3.3: Mean range of fast electrons in germanium [Muk76].

While radiative energy losses are negligible below 1 MeV they dominate the total energy loss above 20 MeV.

The total energy loss data is used to derive the range of an electron with a given energy (compare with Figure 3.3 [Muk76]). As can be seen, the mean range[1] of an electron with a kinetic energy of 1 MeV is only one millimeter, at lower energies the electron travels even less than that. Thus the creation of electron-hole pairs happens in the closest vicinity of the interaction point of the γ-ray, so that it is possible to determine the interaction point of the photon in the crystal.

Germanium detectors are especially suited for γ-ray spectroscopy. Due to the low energy needed to produce an electron-hole pair (E_{pair}= 2.96 eV) and the high purity of the germanium detector material, which inhibits trapping, they have the best energy resolution of all detectors available. The statistical fluctuations ΔN_{pair} of the average number of pairs N_{pair} created is even lower than expected ($\Delta N_{\mathrm{pair}} < \sqrt{N_{\mathrm{pair}}}$), indicating that more complicated considerations about this statistical problem are necessary. An outline of the full statistical analysis [Dru71, Zul70] will be given here.

The mean number of pairs produced is given by

$$N_{\mathrm{pair}} = \frac{E_{\mathrm{dep}}}{E_{\mathrm{pair}}}, \tag{3.6}$$

where E_{dep} is the energy deposited in the interaction and E_{pair} is the average energy needed to produce an electron-hole pair. The fluctuations of N_{pair} originate from the fluctuations of E_{pair}. In order to study these fluctuations one has to be aware that E_{pair} is a sum of the effective bandgap E_{gap}, the mean energy lost in phonon production $\langle E_{\mathrm{phon}} \rangle$ and the average kinetic energy of the electron and the hole $\langle E_{\mathrm{kin}} \rangle$, which are further explained in Table 3.1:

$$E_{\mathrm{pair}} = E_{\mathrm{gap}} + \langle E_{\mathrm{phon}} \rangle + \langle E_{\mathrm{kin}} \rangle. \tag{3.7}$$

The statistical analysis including phase space densities reveals that the fluctuations of the average kinetic energy dominate the fluctuations of E_{pair}. A fluctuation of

$$\Delta N_{\mathrm{pair}} = \frac{\Delta E_{\mathrm{kin}}}{E_{\mathrm{pair}}} \cdot \sqrt{\frac{E_{\mathrm{dep}}}{E_{\mathrm{pair}}}} \tag{3.8}$$

[1]The mean range of a hot electron is the mean distance between the point where it is produced and the point where the last electron-hole pair is excited. It is shorter than the mean path length of the electron.

Symbol	E_{gap}	$\langle E_{\text{phon}} \rangle$	$\langle E_{\text{kin}} \rangle$	E_{pair}
Description	effective bandgap	mean energy lost in phonon production	average kinetic energy of the electron and the hole	electron-hole pair energy
Value	0.93 eV	0.08 eV	1.95 eV	2.96 eV
$\Delta E_x / E_{\text{pair}}$	-	≈ 0.03	≈ 0.25	≈ 0.25

Table 3.1: Contributions to the statistical fluctuations of the average energy needed to produce an electron-hole pair in germanium at a temperature of 90 K. The fluctuations are dominated by the fluctuations of the kinetic energy of the electron and the hole.

has to be expected theoretically, yet electronic noise and an incomplete charge collection somewhat deteriorate this result. In the standard literature the reduced fluctuation is represented by the Fano factor F related to ΔN_{pair} and $\frac{E_{\text{dep}}}{E_{\text{pair}}}$ as follows:

$$\Delta N_{\text{pair}} = \sqrt{F \cdot \frac{E_{\text{dep}}}{E_{\text{pair}}}}. \tag{3.9}$$

From the calculations above a Fano factor of 0.065 is expected whereas measured Fano factors vary around 0.1. The fluctuations of N_{pair} result in an intrinsic broadening Γ_{intr} of the linewidth[2]

$$\Gamma_{\text{intr}} = 2.35 \cdot E_{\text{pair}} \cdot \Delta N_{\text{pair}} = 2.35 \cdot \sqrt{F E_{\text{dep}} E_{\text{pair}}}, \tag{3.10}$$

which limits the energy resolution of the detectors.

3.2 The Drift of Electrons and Holes in the Detector Material

So far it has been discussed what happens in a semiconductor material, when a γ-ray deposits energy; the photon interacts with matter and the deposited energy is finally consumed to produce a number of electron-hole pairs proportional to this energy. Yet these electron-hole pairs recombine unless they are immediately separated. This separation is achieved by operating the germanium detector as

[2]In nuclear physics the full peak width at half maximum (FWHM) is preferred to the standard deviation σ as a measure for the broadening of the linewidth. For a Gaussian peak the following holds: FWHM $= 2.35 \cdot \sigma$

a reverse-biased PIN-diode[3]. The separation of electrons and holes only happens in the depletion layer of the diode, as the electric field there separates the charge carriers and drives them to the contacts. In the contact layers electron-hole pairs recombine. For the MINIBALL modules the thickness of the contact material was kept below 100 μm, so that almost the whole crystal volume is available for γ-ray detection.

In order to follow the drift path of the electrons and holes, the electric field in the detector has to be determined. Then the electron and hole drift velocity for each point in the detector can be derived. As the drift velocity is the first derivative of the drift path, an ordinary differential equation is obtained, whose solution corresponds to the time-dependent drift path.

The electrostatic field $\vec{E}$ in the detector can be calculated when the electric potential ϕ is known.

$$\vec{E}(\vec{r}) = -\vec{\nabla}\phi(\vec{r}) \tag{3.11}$$

In the depletion layer of the crystal and in the vacuum inside the capsule (inner volume Ω) this potential obeys the Poisson equation

$$\nabla^2\phi(\vec{r}) = -\frac{\rho(\vec{r})}{\varepsilon} = -\frac{eN}{\varepsilon_0\varepsilon_r} \qquad \vec{r} \in \Omega. \tag{3.12}$$

On the electric contacts and the walls of the capsule the potential is predetermined (Dirichlet boundary conditions on the surface $\delta\Omega$).

$$\phi_{\text{boundary}}(\vec{r}) = f(\vec{r}) \qquad \vec{r} \in \delta\Omega \tag{3.13}$$

The impurity concentration in the depletion layer $N = N_\text{A} - N_\text{D}$ is the difference between the acceptor density N_A and the donor density N_D. For the MINIBALL modules N varies between $0.5 \cdot 10^{10}\text{cm}^{-3}$ and $2 \cdot 10^{10}\text{cm}^{-3}$ [Gut96], corresponding to a space charge density between $0.8\frac{\text{nC}}{\text{cm}^3}$ and $3.2\frac{\text{nC}}{\text{cm}^3}$. The dielectric constant ε_r of germanium is 16 [Sze81].

The drift velocity $\vec{v}_{\text{drift}}$ of the electrons and holes is determined by the electric field. For small electric fields the velocity is proportional to the field applied,

[3]A PIN-diode (P-doped Intrinsic N-doped) is a diode with a large intrinsic region between the p- and n-doped contacts. When a reverse bias is applied, the depletion layer extends across this intrinsic zone, so that the depleted volume surpasses the contact volume by orders of magnitude.

for higher fields the velocity levels off and approaches a limit (compare with Figure 3.4), as high-energy low-mobility valleys of the conduction band start to contribute to the conduction. In crystalline solid materials the drift velocity does furthermore depend on the direction of the crystal lattice and the field and the drift velocity are in parallel only for the main crystal directions. This deviation of the drift velocity from the direction of the electric field was first observed by Sasaki [Sas56].

In germanium the drift velocity of both electrons and holes has a maximum in parallel to the [100]-direction and a minimum in parallel to the [111]-direction. While the electron drift is extremely well studied even in directions other than the main crystallographic axes [Neu73, Jac81], very little data are available for holes in germanium [Reg76, Reg77], in particular no experimental data are available for directions other than the [100]-, [110]- and, [111]-direction.

Since the early days of germanium detectors the anisotropic behaviour has been neglected in the analysis of simulations and experiments, but it has been pointed out recently [Mih98] that the internal position resolution of germanium detectors obtained from any isotropic pulse-shape analysis (PSA) algorithm will be limited by the anisotropy. In the isotropic fit the drift velocity is approximated by

$$\vec{v}_{\mathrm{drift}_{\mathrm{e,h}}}(\vec{E}) = \frac{\mu_{0_{\mathrm{e,h}}}\vec{E}}{\left[1+\left(\frac{|\vec{E}|}{E_{0_{\mathrm{e,h}}}}\right)^{\beta_{\mathrm{e,h}}}\right]^{\frac{1}{\beta_{\mathrm{e,h}}}}} \tag{3.14}$$

The fit parameters μ_0, E_0 and β are temperature dependent, for liquid nitrogen temperatures (77 K) the following values are quoted [Rau82, Kno89]:

	electrons(e):	holes(h):
E_0	275 V/cm	210.5 V/cm
β	1.32	1.36
μ_0	$3.6 \cdot 10^4$ cm^2/Vs	$4.2 \cdot 10^4$ cm^2/Vs

As can be seen in Figure 3.4 this fit can deviate by more than 20% from the real value and the deviation is strongly energy and lattice-direction dependent. Hence it is necessary to include the anisotropy into the fit. In order to fully understand the anisotropy of the drift velocity one has to study the energy band structure ($\vec{k}$-E diagram) of germanium [Hun92], which is shown in Figure 3.5. Germanium

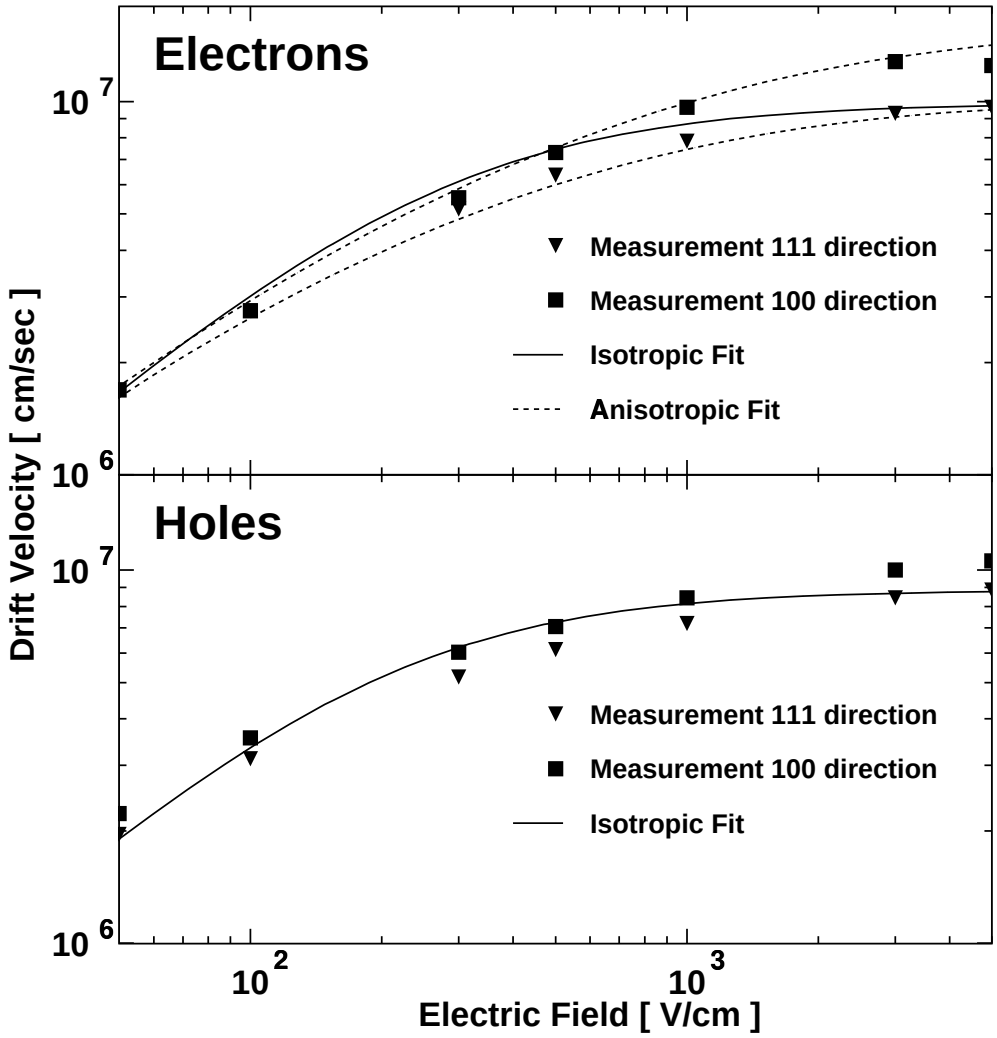

Figure 3.4: Velocity field curves of electrons and holes in germanium. For electrons an isotropic and an anisotropic fit is given, for holes only an isotropic fit is available.

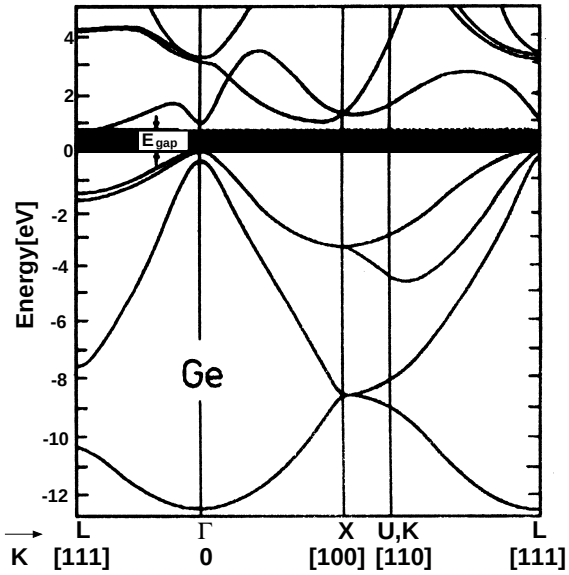

Figure 3.5: $\vec{k}$-E-diagram of germanium. Germanium is an indirect semiconductor with the conduction band minimum at the L-point (fringe of the Brillouin zone in 111-direction) and the valence band maximum at the Γ-point (centre of the Brillouin zone). The band gap is $\sim$0.7 eV at a temperature of 80 K. The image is taken from [Hun92].

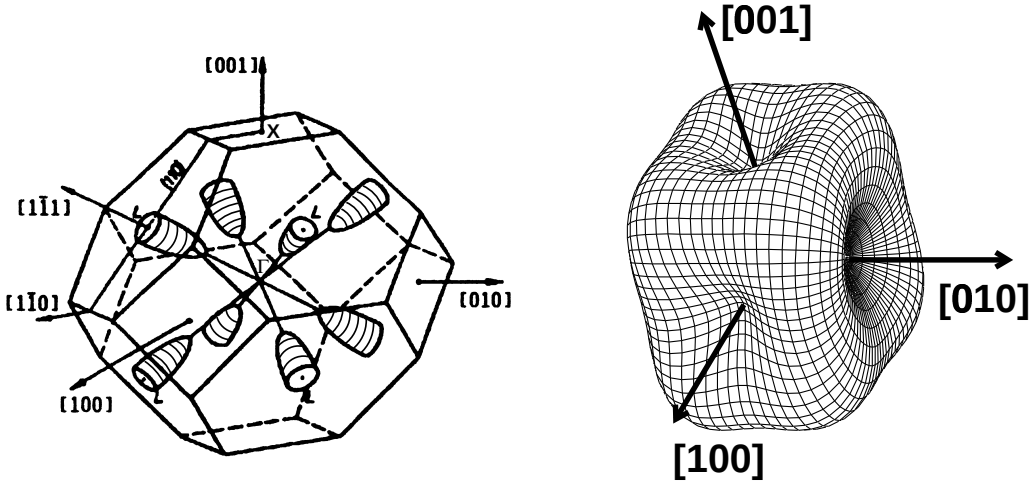

Figure 3.6: Conduction band and valence band in germanium. In the first panel a surface of constant energy for conduction band electrons is shown within one Brillouin zone. The surface is not contiguous, but consists of 8 half-ellipsoids. The size of these half-ellipsoids depends on the energy difference between the conduction band minimum and the electron energy. The image is taken from [Hun92]. In the second panel a surface of constant energy in the valence band of germanium is shown. The size of the warped sphere scales with the difference between the hole energy and the valence band maximum (0 eV by definition). The plot is recalculated after [Reg76].

is an indirect semiconductor with the conduction band minimum at the L-point (fringe of the Brillouin zone in [111]-direction) and the valence band maximum at the Γ-point (centre of the Brillouin zone). Hence the conducting electrons are distributed in 8 half-ellipsoids near the conduction band minimum at the fringes of the Brillouin zone, while the conducting holes are distributed over a warped sphere close to the maximum of the valence band (see Figure 3.6).
The theory of the anisotropy of the electron conduction in a simplified case, where only scattering between the half-ellipsoids by phonons is considered and the contribution of the higher valleys of the conduction band is neglected, is described in [Reik62]. All 8 half-ellipsoids contribute to the conduction. The average drift velocity of an electron is derived as

$$\vec{v}_{\text{drift}} = \sum_{j=1}^{8} \frac{n_j}{n} \cdot \vec{v}_{j\,\text{drift}} \quad \text{with} \quad n = \sum_{j=1}^{8} n_j, \tag{3.15}$$

where $\frac{n_j}{n}$ is the relative occupation probability of the half-ellipsoid and $\vec{v}_{j\,\text{drift}}$ is the average drift velocity the half-ellipsoid contributes. When an electric field $\vec{E}$ is applied the energy and the density of free states of each half-ellipsoid is changed so that the half-ellipsoids start to fill unequally. Phonon scattering of the electrons tries to restore an equal distribution so that an equilibrium is reached. For a dilute electron gas one finds

$$\frac{n_j}{n} = \frac{\sqrt{\vec{E}^T \cdot \hat{\mathbf{a}}_j \cdot \vec{E}}^{-1}}{\sum_{l=1}^{8} \sqrt{\vec{E}^T \cdot \hat{\mathbf{a}}_l \cdot \vec{E}}^{-1}} \quad \text{with} \quad \hat{\mathbf{a}}_j = U_j^T \begin{pmatrix} \frac{m_e}{m_l} & 0 & 0 \\ 0 & \frac{m_e}{m_t} & 0 \\ 0 & 0 & \frac{m_e}{m_t} \end{pmatrix} U_j, \tag{3.16}$$

where m_e is the free electron mass, m_l and m_t are the longitudinal and transverse electron masses in the ellipsoid, and U_j is the rotation matrix, which rotates the reciprocal effective mass tensor in the direction of the ellipsoid. With the knowledge of the electron distribution, a vector $\vec{S}$ can be defined,

$$\vec{S} = \sum_{j=1}^{8} \frac{n_j}{n} \frac{\hat{\mathbf{a}}_j \cdot \vec{E}}{\sqrt{\vec{E}^T \cdot \hat{\mathbf{a}}_j \cdot \vec{E}}} = \frac{1}{\sum_{l=1}^{8} \sqrt{\vec{E}^T \cdot \hat{\mathbf{a}}_l \cdot \vec{E}}^{-1}} \sum_{j=1}^{8} \frac{\hat{\mathbf{a}}_j \cdot \vec{E}}{\vec{E}^T \cdot \hat{\mathbf{a}}_j \cdot \vec{E}} \tag{3.17}$$

which describes the anisotropy of the drift velocity. Using this vector a fit can be derived.

$$\vec{v}_{\text{drift}_e}(\vec{E}) = C_2 \cdot \frac{1}{\sum_{l=1}^{8} \sqrt{\mathbf{X}_l}^{-1}} \sum_{j=1}^{8} \frac{\hat{\mathbf{a}}_j \cdot \vec{E}}{\mathbf{X}_j},$$

$$\text{with} \qquad \mathbf{X}_j = \vec{E}^T \cdot \hat{\mathbf{a}}_j \cdot \vec{E} + C_1 \cdot \sqrt{\vec{E}^T \cdot \hat{\mathbf{a}}_j \cdot \vec{E}} + C_0 \tag{3.18}$$

In this fit $\vec{S}$ has to be altered to account for the field dependence of the drift velocity (linear rise at low fields, limiting value at high fields); $\sqrt{\vec{E}^T \cdot \hat{\mathbf{a}}_j \cdot \vec{E}}$ has to be replaced by $\sqrt{\mathbf{X}_j}$, where C_1 and C_0 are the two fit parameters needed for this replacement. The parameter C_2 is the proportionality constant of the altered $\vec{S}$ and $\vec{v}_{\text{drift}}$. Even though this fit uses the same number of fit parameters as the isotropic fit, the anisotropic fit describes the measured velocity field curves considerably better (compare with Figure 3.4). Furthermore the measured angular deviation of the drift velocity from the direction of the electric field is also correctly described. For the fit parameters the following values were obtained:

Fit parameters of the anisotropic fit:

C_0	$1.17{\cdot}10^6$ V^2/cm^2
C_1	4430 V/cm
C_2	$1.97{\cdot}10^7$ cm/s

The theory of anisotropic hole conduction in a warped sphere is by far more difficult than the theory for electron conduction described above. One has to cut the warped surface in sectors, calculate scattering probabilities between these sectors and simulate the drift with Monte-Carlo methods [Reg76]. As the experimental data available until now is scarce, it would only be possible to produce a fit that correctly describes the drift velocity along the crystallographic axes. The drift velocity along other axes and the angle between the drift velocity and the electric field could only be predicted from theory. Unfortunately the angular deviation of the drift velocity from the electric field would be far more interesting than the absolute value, because such a deviation could result in a hole drift path from one segment into another segment, while the hole drift time is of minor importance for the pulse shape. As the most important data of an anisotropic fit would be unreliable, the attempt to produce such a fit was abandoned.

With the knowledge of the electric field $\vec{E}$ in the detector and the position $\vec{r}_0$ where the electron-hole pairs have been created, the drift path $\vec{r}(t)$ can now be calculated by solving the ordinary differential equation:

$$\frac{d}{dt}\vec{r}_{e/h}(t) = \vec{v}_{drift_{e/h}}(\vec{E}(\vec{r}_{e/h}(t))) \quad \text{with} \quad \vec{r}_{e/h}(t=0) = \vec{r}_0 \tag{3.19}$$

The solution of this equation is the time dependent drift path of the charge carriers.

3.3 Detector Pulse Generation

Until now the interactions of γ-rays with the detector material, the production of electron-hole pairs, and the drift of the charge carriers to the contacts of the detector have been studied, but it still needs to be discussed how the drifting electrons and holes affect the detector pulses on the contacts.

The accumulation of charges starts as soon as the electrons and holes start to separate, which is *immediately* after the γ-ray has deposited its energy. Both electrons and holes induce charges on *all* contacts. The drift velocity is so small compared with the speed of light, that at any time the charge on the contacts can be calculated by solving the electrostatic problem with the electrons and holes at fixed positions.

In the beginning the charges induced by an electron and a hole at the same place cancel out. Then the electrons and holes start to separate and mirror charges start to accumulate on the contacts. When a drift charge approaches a contact, the mirror charge on this contact induced by the drift charge is equal and of opposite sign; all the other contacts cannot "see" this drift charge any more. Finally the drift charge annihilates with its induced mirror charge.

In order to calculate the pulse on a contact the induced mirror charge has to be known for every position inside the detector. It is possible to calculate the position dependent mirror charge by brute force, but there is a more elegant way to solve the problem:

One starts with Green's second identity [Jac83]

$$\int_V \Phi\Delta\Psi - \Psi\Delta\Phi dV = \int_{\delta V} \Phi\frac{\partial\Psi}{\partial n} - \Psi\frac{\partial\Phi}{\partial n}dA, \tag{3.20}$$

where Φ and Ψ are arbitrary scalar fields. Then a special set of variables has to be chosen. Two electrostatic setups with the same geometry, but different potentials (ϕ, ϕ'), different space charge distributions (ρ, ρ'), and different surface charge distributions (σ, σ') are selected. One can now substitute $\Phi = \phi$, $\Psi = \phi'$, $\Delta\Phi =$

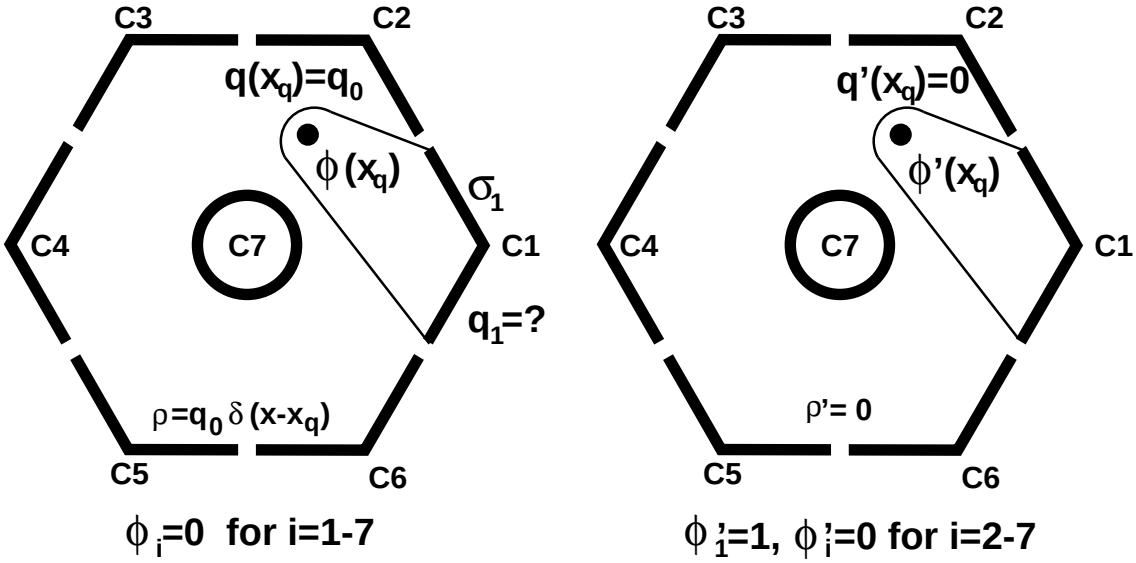

Figure 3.7: Calculation of the mirror charge. The left frame shows the problem to be solved, whereas the right frame shows a model problem that can be easily solved. Both problems are related by Green's reciprocity principle, so that it is possible to solve the actual problem by solving the model problem.

$-4\pi\rho$, $\Delta\Psi = -4\pi\rho'$, $\frac{\partial\Phi}{\partial n} = -4\pi\sigma$, and $\frac{\partial\Psi}{\partial n} = -4\pi\sigma'$. An equation called Green's reciprocity principle is obtained, which couples the two different electrostatic setups

$$\int_V \phi'\rho dV - \int_{\delta V} \phi'\sigma dA = \int_V \phi\rho' dV - \int_{\delta V} \phi\sigma' dA. \tag{3.21}$$

Then two very special setups are chosen. One setup is the mirror charge problem to be solved, in this case it is the mirror charge q_1 on contact C_1 induced by the charge q_0 at the position x_q, as can be seen in in the first frame of Figure 3.7. The potentials of all contacts are zero for this problem, even for the centre contact, as there is only interest in the mirror charge induced by the test charge q_0 and not in the charges on the contacts resulting from the bias voltage. In the second setup (second frame of Figure 3.7) a model problem with no charges inside the detector, a unity potential on contact C_1, and zero potential on all other contacts is used. The volume for the integration must include the test charge, contact C_1 must be part of the surface of the volume, all other surfaces of the integration volume must be inside the detector. With the help of the model problem the mirror charge for a drift charge at an arbitrary position inside the detector can be easily calculated

using equation 3.21. All known values are filled in the equation and the right side cancels out completely.

$$\int_V \phi' q_0 \delta(\vec{x} - \vec{x_q}) dV + \int_{\delta V} \phi' \sigma dA = \int_V \phi \cdot 0 dV + \int_{C_1} 0 \cdot \sigma' dA + \int_{\delta V \setminus C_1} \phi \cdot 0 dA \quad (3.22)$$

The two remaining terms relate the mirror charge q_1 on contact C_1 with the potential $\phi'(\vec{x_q})$ of the model problem. As the mirror charge is directly proportional to this potential it is usually called the weighting potential

$$q_1 = \phi_1' \int_{\delta V = A_1} \sigma dA = \int_{\delta V} \phi' \sigma dA = -\int_V \phi' q_0 \delta(\vec{x} - \vec{x_q}) dV = -q_0 \cdot \phi'(\vec{x_q}) \quad (3.23)$$

Hence the charge pulse $q_i(t)$ of any contact can finally be calculated. It is the superposition of the mirror charge pulses of all drift charges q_{0j}[4]:

$$q_i(t) = \sum_j -q_{0j} \cdot \phi_{\text{weight}\,i}(\vec{r}_j(t)) \quad (3.24)$$

The corresponding current $I_i(t)$ is the time derivative of the charge:

$$I_i(t) = \frac{dq_i(t)}{dt} = \sum_j -q_{0j} [\nabla \phi_{\text{weight}\,i}(\vec{r}_j(t)) \cdot \vec{v}_{\text{drift}}(\vec{E}(\vec{r}_j(t)))] \quad (3.25)$$

3.4 The Main Interaction Concept

Until now, it has been discussed how a germanium detector can transform the energy deposited by a γ-ray into an energy and position dependent detector pulse, but one still needs to find out what information can be extracted from such a detector pulse.

The most important information is the energy of the incident γ-ray. For γ-ray spectroscopy therefore usually only the *full-energy events*[5] (FEE) are relevant, as only these events deposit the total energy of the initial γ-ray in the detector; for all other events not even this crucial piece of information is included in the detector pulse, so that they only contribute to the background.

As the germanium detectors will be used to detect γ-rays emitted from nuclei

[4] It should be noted that every interaction produces two drift charges, the corresponding electrons and holes.

[5] They are also called *full-energy-peak events* as they contribute to the sharp peak in the γ-spectrum reflecting the full-energy events.

with large recoil velocities, it is necessary to extract information not only about the energy, but also about the direction of the emitted γ-ray with a directional resolution much better than the resolution determined by the solid angle of the detector in order to achieve a good Doppler correction. A FEE deposits its energy in one or more interactions, of which the last one must be a photoeffect. As γ-rays travel with the speed of light the time between these interactions is negligible and cannot be resolved electronically. Hence there is no means to distinguish the first interaction, whose location together with the target position directly determines the γ-ray emission direction, from other interactions electronically. The interaction one can expect to locate inside the detector most easily is the interaction where the largest fraction of the initial energy of the photon is deposited, as the charge pulses of this interaction will dominate the total detector pulse. This interaction will be called the *main interaction*.

It does not make sense to study the main interaction unless its location is strongly related to the first interaction. For low γ-energies, almost all FEEs will be photoelectric absorption events with only one interaction, i.e. first and main interaction coincide. At high energies above 2.5 MeV most of the FEEs will have a pair-production as the first interaction. Here again, the first interaction and the main interaction coincide, as only 2×511 keV are carried away by the secondary photons produced in the positron annihilation.

For energies between about 100 keV and 2.5 MeV the first interaction is usually a Compton scattering. Here the first interaction and the main interaction do not necessarily coincide. For a given γ-energy E_γ and a Compton scattering angle θ the relative energy loss ϵ is given by

$$\epsilon = \frac{1-\cos(\theta)}{1-\cos(\theta)+\frac{m_e c^2}{E_\gamma}} \tag{3.26}$$

The relative energy loss as a function of the initial energy and the scattering angle is shown in Figure 3.8. It is interesting to note that for an initial γ-energy below half the rest mass of the electron the relative energy deposition is always below 50%, so that it is unlikely that the first interaction coincides with the main interaction. Here the direction from the target to the first interaction can strongly deviate from the direction to the main interaction. At high initial γ-energies, either more than 50% of the initial energy is deposited in a Compton-scattering

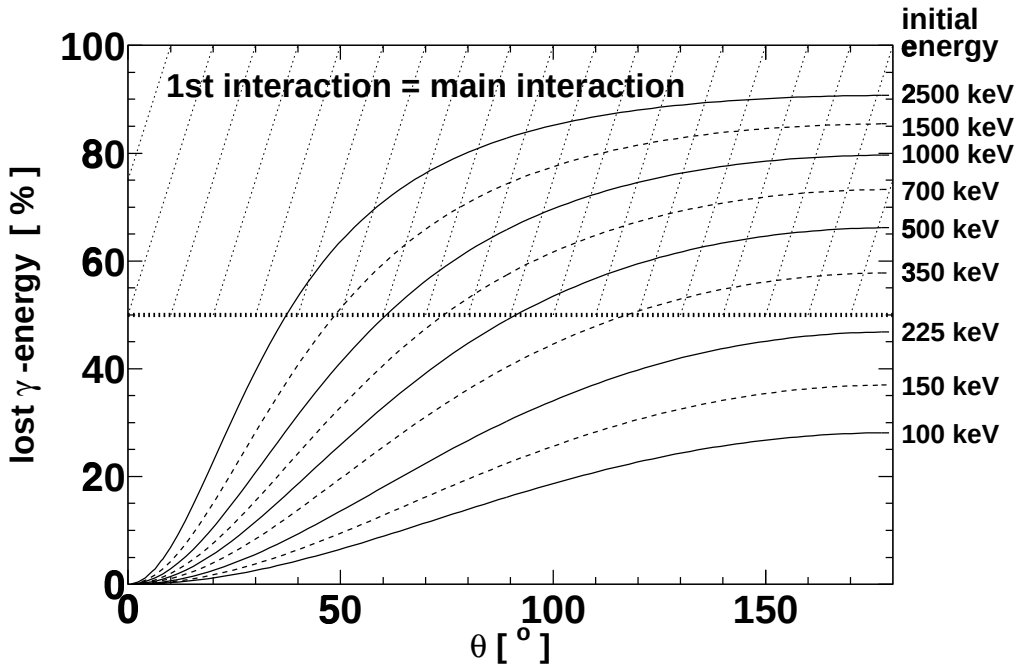

Figure 3.8: Relative energy loss in a Compton scattering interaction depending on initial energy and scattering angle. The shaded area marks the region where the first interaction – when proceeding via the Compton effect – is automatically also the main interaction.

event, so that the first and the main interaction automatically coincide, or both interactions coincide, although less than 50% of the initial γ-energy is deposited in the first interaction, or the scattering angle is very small, so that the scattered γ-ray is hardly deflected from the direction of the initial γ-ray. Hence the biggest deviation, when reconstructing the direction of the emitted γ-ray from the position of the main interaction instead of the first interaction, has to be expected for γ-energies between 150 keV and 500 keV.

At this stage the fundamental physics, which determine the detector behaviour, have been presented in detail and the main-interaction concept, which will be applied to achieve a better Doppler-shift correction, has been discussed. The analysis of the three types of interactions of γ-rays with matter has revealed that only for Compton-effect first interactions problems concerning the Doppler-shift correction have to be expected, as first and main interaction do not necessarily coincide. In particular the energy range between 150 keV and 500 keV is problematic, as the directions from the target to the first and to the main interaction,

respectively, may deviate considerably.
In order to obtain quantitative information about the expected position resolution in the detector and the resulting energy resolution after Doppler correction simulations are needed. The simulations techniques used in this work are presented in the following. They strongly rely on the fundamental germanium detector physics presented before.

3.5 Simulation Techniques

3.5.1 Introduction

Based on the germanium-detector physics discussed in the previous sections the properties of a MINIBALL Cluster module and of the MINIBALL 3-Cluster were simulated. The simulations were split in 4 different parts:

- The scattering and absorption of γ-rays in the germanium material was simulated using the GEANT package [CERN93].
- The Finite Difference Method (FDM) was used to obtain a discretization of the Poisson equation [Gro94] and a Successive Over-Relaxation (SOR) solver [Hac93] was used to calculate the electrostatic field in the detector and the weighting potentials of the core and the segment contacts.
- A second-order integrator [Sto90] was applied to the Ordinary Differential Equations (ODE, compare with equations 3.19/3.24) to calculate the drift of the charges in the detector and the resulting detector pulses.
- Various data-analysis programs were applied to the simulated data, so that simulated spectra could be derived. The results were compared with measurements, where available.

The simulations aimed to determine basic properties of the detectors like their efficiency. Furthermore the physical limitations of the detector granularity were tested. Finally, fast algorithms to achieve a suitable position resolution inside the detector module were developed and energy resolution predictions were made. Before these simulations will be discussed in chapter 4 the different parts of the simulation will be described in more detail.

3.5.2 GEANT Simulations

The Monte-Carlo package GEANT, available from CERN, was used to simulate the scattering and absorption of γ-rays in the germanium material. The package uses the detector geometry, the detector material, the source position, the source velocity and the γ-energy as input parameters and calculates the position, type, and energy of all γ-ray interactions. Furthermore the deceleration of the fast electron (positron) within the detector material and the generation of secondary Bremsstrahlung γ-rays, positron-annihilation γ-rays, and electron-hole pairs is included in the simulations, so that the actual energy deposited in each segment can be extracted from the data.
GEANT is ideally suited to derive detector properties like efficiency, mean penetration depth of the γ-ray, energy distributions of the different segments, and the physical limitations of the position resolution due to e.g. multiple scattering. Yet the GEANT simulations are not sufficient to simulate energy and position resolution, since e.g. the radius information and the angular refinement will be extracted by pulse-shape analysis (PSA) of the core signal and the segment signals, respectively. Therefore one needs to simulate how the pulses are generated on the electrodes and how they are further processed.

3.5.3 Calculation of the Potentials

The electric field and the weighting potentials in the detector do not contain data that is directly relevant for γ-ray spectroscopy, yet their influence on the pulse shape is enormous, as they determine the drift velocity and the mirror charges. In contrast to previous work [Gun97, Pal97], where commercially available programs were used, a SOR solver was developed and applied to the PDE[6]-problems. The commercial programs were considered insufficient, as none of them allowed the free assignment of the space charge inside the detector volume (corresponding to the right-hand side of the Poisson equation). Furthermore the self-made program allowed a better control of the error estimator. The Poisson equation was discretized on a a regular grid with a step size of 0.5 mm using the Finite Difference Method. In order to describe the boundaries, boundary points were placed within

[6]The Poisson equation is a Partial Differential Equation (PDE)

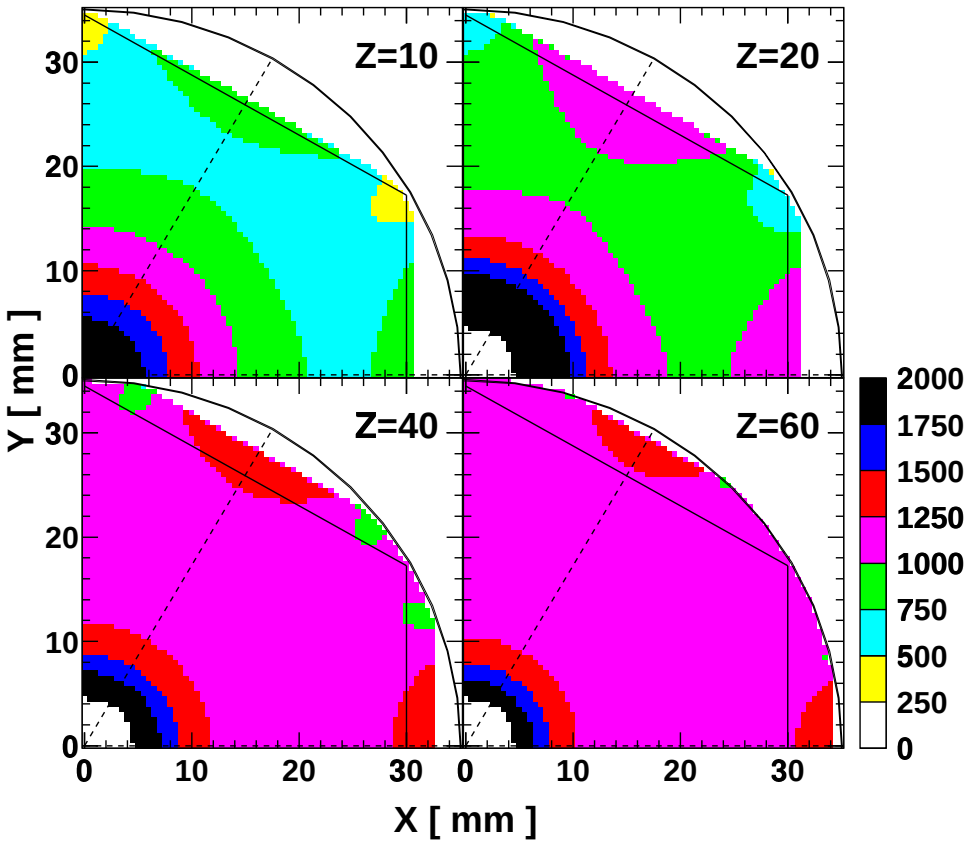

Figure 3.9: Absolute value of the electric field $[\frac{\mathrm{V}}{\mathrm{cm}}]$ in the detector at 4 different depths (z[mm]) for a constant impurity concentration of $5{\times}10^{9}\mathrm{cm}^{-3}$ and a bias voltage of 3500 V. The electric field is symmetric, so that only a quarter of the detector needs to be shown. Electric field strengths exceeding 2000 V/cm are also shown in black. The front view of the detector with the segmentation lines is included in the picture to guide the eye.

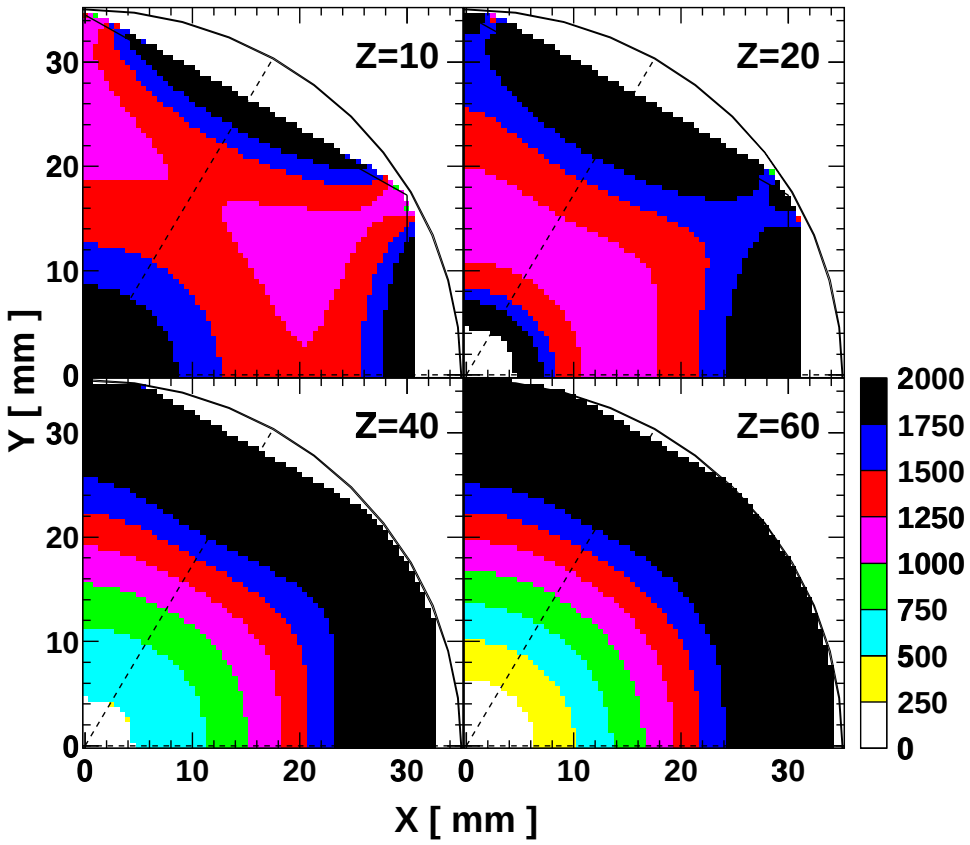

Figure 3.10: Absolute value of the electric field $[\frac{\mathrm{V}}{\mathrm{cm}}]$ in the detector at 4 different depths (z[mm]) for a a bias voltage of 4000 V and an impurity concentration that rises linearly from $7{\times}10^{9}\mathrm{cm}^{-3}$ at $R = 0$ cm to $20{\times}10^{9}\mathrm{cm}^{-3}$ at $R = 3.5$ cm. The electric field is symmetric, so that only a quarter of the detector needs to be shown. Electric field strengths exceeding 2000 V/cm are also shown in black. The front view of the detector with the segmentation lines is included in the picture to guide the eye.

0.005 mm and 0.505 mm away from inner points at the places, where the grid intersects the boundary[7]. A total number of about 800000 knots were used.
In order to account for the varying impurity concentration of different detector crystals (compare with page 11) the electric field was calculated for a detector with a high and with a low impurity concentration, corresponding to a small and a large space charge within the detector. In Figure 3.9 the electric field inside the detector is shown at different depths z in the detector for a small constant space charge of $5\times10^9\text{cm}^{-3}$ and a core potential of 3500 V, typical for a low impurity concentration detector. (The coordinate system used can be found in Figure 2.2 on page 10.) In the front part of the detector ($z = 10$ mm) the strongest fields (dark) can be found near the core contact and areas with very low field strength (light) appear in the vicinity of the corners of the detector. In the rear part of the detector ($z = 60$ mm) an almost constant field strength above 1000 V/cm is encountered which rises near the core contact. Figure 3.10 shows the electric field inside the detector for a potential of 4000 V and an impurity concentration with a linear radial rise from $7\times10^9\text{cm}^{-3}$ at $R = 0$ cm to $20\times10^9\text{cm}^{-3}$ at $R = 3.5$ cm, which are typical values for a high impurity detector. Here very high field strengths are encountered in the front part of the detector with maxima both at the inner contact and the outer contacts. In the rear part of the detector ($z = 60$ mm) the field strength rises from values below 500 V/cm at the core to maximum values at the outer contacts.
These two setups represent the extremes of a low-impurity and a high-impurity concentration detector. The bias voltages needed to deplete the detector rise with impurity concentration. It is essential to keep in mind that the germanium crystals delivered from the manufacturer show such variations in their impurity concentration and that all simulations can only describe the properties of an "average" detector module. The impurity concentration inside the crystal can only be measured by destructive methods, so that only estimates exist for the operational modules. Hence it seems to be futile to simulate the detector properties at all, but the variations of the electric field are less important than anticipated. Their influence is moderated by the shape of the velocity field curves of both electrons and

[7] A minimum distance of 0.005 mm has to be kept in order to avoid numerical problems; for smaller distances one inner knot has to be omitted.

holes which levels off for electric fields above 500 V/cm (Figure 3.4). Therefore, for all the pulse simulations a constant impurity concentration of $10\times10^{9}\mathrm{cm}^{-3}$ and a bias voltage of 4000 V were used in order to obtain results for an "average" detector.

As the mirror charge accumulated on a contact is directly proportional to the weighting potential of this contact at the position of the drift charge, the weighting potential has a strong influence on the pulse shape (equation 3.24, page 33). As can be seen in Figure 3.11, the gradient of the weighting potential of the inner contact has a distinct maximum in the vicinity of the core contact. As the drift velocity of electrons and holes is similar for equal fields (Figure 3.4) and does not vary by more than a factor of 2 within the detector, as long as the field strength is above 500 V/cm, electrons, which travel to the core contact, will dominate the shape of the current pulse of the inner contact, while holes, which travel to the segment contacts, contribute less. It will therefore be possible to distinguish between the electron and the hole contribution to the core current pulse.

In contrast to the weighting potential of the inner contact, which is shown on a linear scale, the segment weighting potential needs to be shown on a logarithmic scale (Figure 3.12). Here the pulse of the hit segment is of minor interest for pulse-shape analysis, as this pulse is a superposition of the charge pulse of the core and the mirror charge pulses of the remaining segments. Instead the focus has to be put on the adjacent segments of the hit segment. If these segments are not hit themselves, the charge temporarily accumulated on them can help to locate the drift charge in the hit segment.

Until now, the reliability of the numerical simulations of the fields and potentials has not yet been discussed. As the correct solutions are not available, an error estimator has to be used. As a simple error estimation procedure the differential equation is solved on a coarse and a refined grid and the difference of both solutions is calculated for every knot of the coarse grid. A reasonable relative error was found for both the electric field in the detector and the weighting potentials. A relative error below 2% was achieved in more than 97% of all knots, an error below 5% in more than 99% of all knots. For both the electric field and the weighting potentials the maximum relative errors occurred at the curved front part of the inner contact. Furthermore the segment weighting potential had large relative

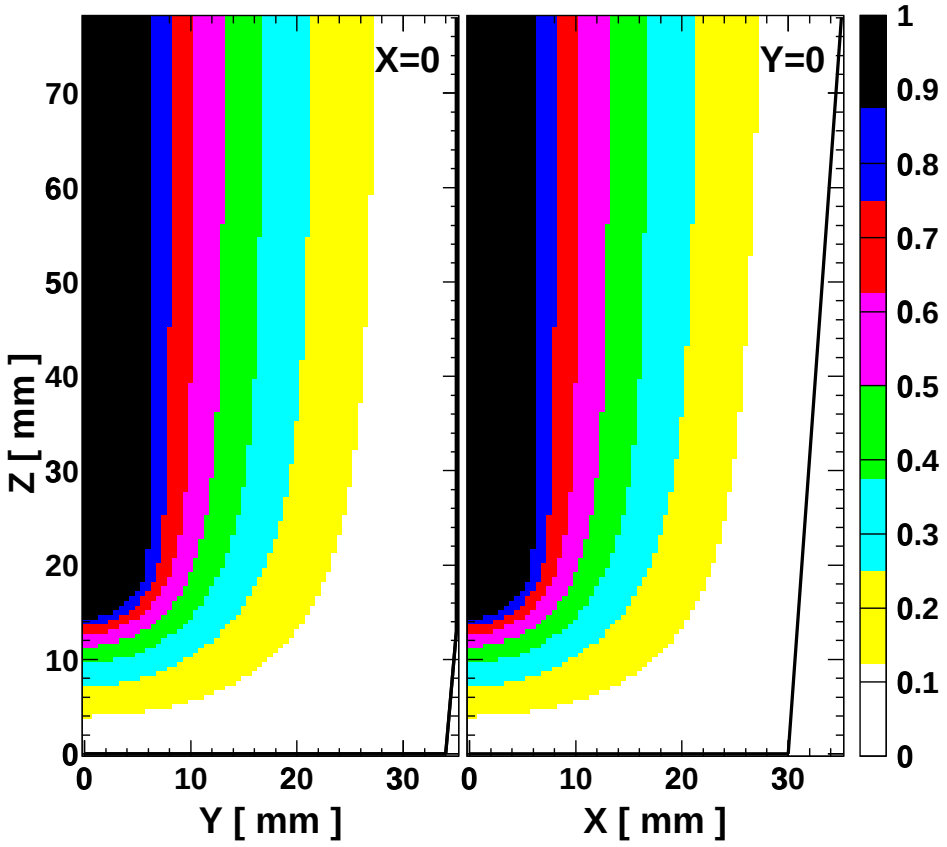

Figure 3.11: Weighting potential of the core contact at the x = 0 mm and y = 0 mm cross sections. For symmetry reasons only one half of the detector needs to be shown. The outer limits of the detector crystal are shown.

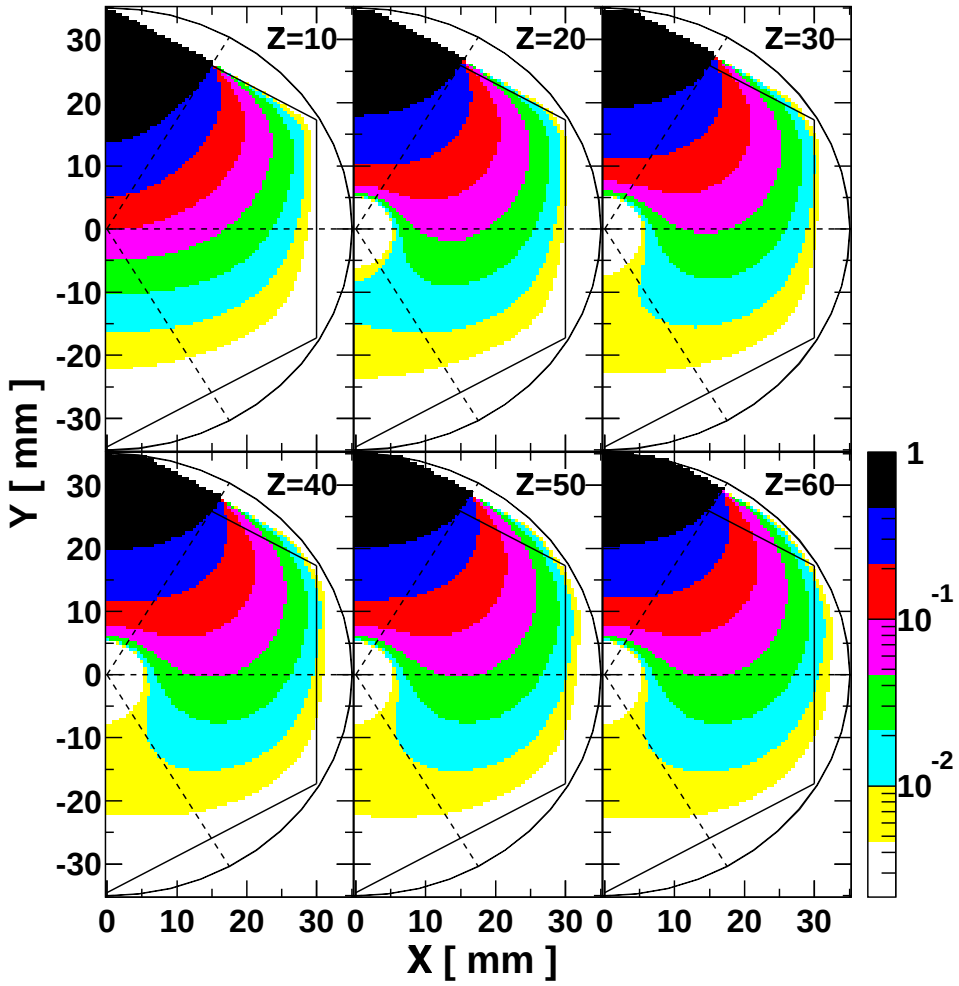

Figure 3.12: Weighting potential of the upper segment for 6 different depths (z[mm]). The weighting potential is symmetric, so that only one half of the detector needs to be shown. It should be noted that a logarithmic scaling is used. The front view of the detector with the segmentation lines is included in the picture.

errors near the segmentation line. Both problematic regions are not unexpected. The curvature of the front part of the inner contact is so strong that the few knots of the coarse grid are not sufficient to describe it. Furthermore the inner contact can be seen as a polyhedron which penetrates into the volume. It is well known that corners which penetrate into the volume are a substantial problem for a PDE solver. In addition at the segmentation line two Dirichlet boundaries with different potentials touch, so that the solution in the closest vicinity of the segmentation line is always questionable.

3.5.4 Pulse-Shape Simulations

In order to solve the drift equation and calculate the charge on each contact an Ordinary-Differential-Equation solver (integrator) was needed. The solver had to be fast to process vast amounts of events and accurate to obtain usable pulses. Both aims could only be achieved by a solver with variable step size, which could be adjusted to large steps, when the pulse rose or fell smoothly, and short steps, when the pulse height varied quickly.
A second-order integrator was used for this purpose. The time-step size was limited to values between 0.025 and 2 ns. The electric field and the weighting potentials were only available on the 0.5 mm grid, values in-between were obtained by interpolation. For the electric field a linear interpolation was used, for the potentials a third order Hermite interpolation was applied. Both interpolations were selected to allow a continuous assignment of the field and the potential values respectively.
For a second-order integrator it is necessary to have a continuous first derivative of the "right-hand" side; in this case $\vec{v}_{drift_{e/h}}(\vec{E}(\vec{r}_{e/h}(t)))$ and $\phi_{\text{weight}}(\vec{r}(t))$, which is used in the function to control the step size, must have continuous first derivatives. Unfortunately this criterion is not fulfilled when the border between two cubes of the grid is crossed. The problem stems from the PDE solver, as the simple Finite Difference Method only yields potentials which can be interpolated up to the second order. Hence it is impossible to have an interpolation of an order above one for the electric field. In consequence the drift velocity does not have a continuous second derivative either. Even though the discontinuities can cause a reduced quantitative accuracy of the simulation, the results nevertheless remain

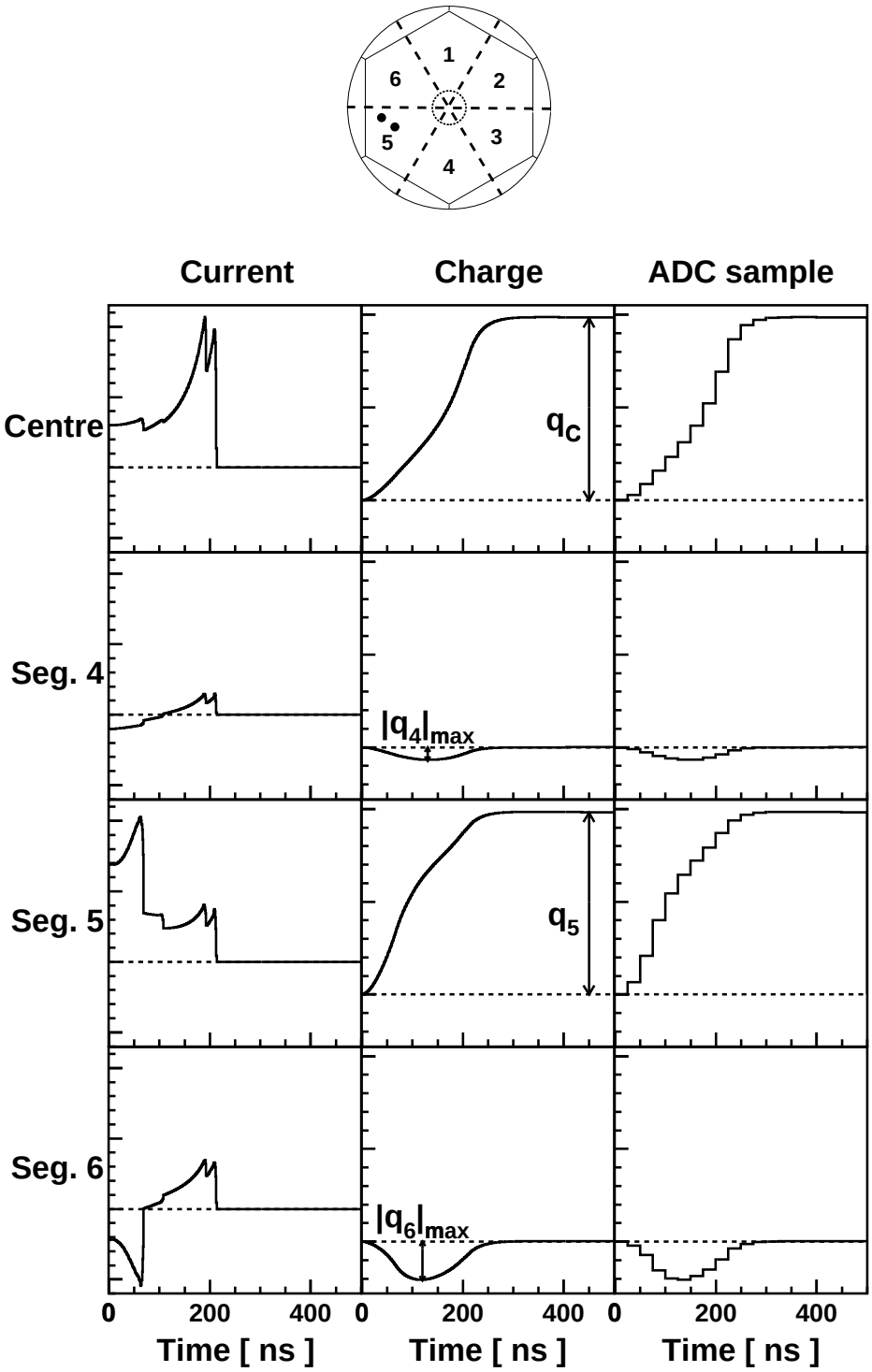

Figure 3.13: Sample pulses of an event with two interactions which is contained in one segment (segment 5). The detector pulses (current pulses), the preamplifier pulses (preamplifier charge pulses), and the ADC samples (ADC charge pulse) are shown for the core of the detector, the hit segment, and its two neighbours. The zero line is shown as a dashed line. In each column the same scaling is selected for all graphs.

valid. The reason is again the relatively small electric field dependence of the drift velocity. The drift velocity changes significantly only on scales larger than the mesh width and can be considered almost constant. Hence large changes of either the velocity or its first derivative are not expected. In contrast, the weighting potential, especially the one of the segments, can vary rapidly within short distances. Yet, as the continuity of the first derivatives of all weighting potentials is ensured, the weighting potential functions are compatible with a second order integrator.

In order to reduce the amount of data and allow a simple pulse processing the pulses were discretized on a 1 ns grid. The simulated charge pulses of each contact were transformed into current pulses by taking the differences of successive charge pulse heights (current pulses in Figure 3.13). Digital filters representing the pulse shaping of the preamplifier (integration time $\sim$16 ns and decay time 50 μs) and the input filter stage of the XIA module (20 MHz low pass filter) were applied to these pulses to obtain the pulses fed into the fast ADCs (the charge pulses in Figure 3.13 correspond to the preamplifier charge pulses). Finally samples with a sampling time of 25 ns (the sampling rate of the fast-ADC) and a random time offset between 0 ns and 25 ns were produced and saved for further processing (ADC charge pulses). Unless otherwise stated, the pulse simulations were made for the "average" detector module, the anisotropic fit was used for the electrons and the isotropic fit for the holes. The electronic noise of the detector and the different amplifier stages was not included in the simulations; the drift charges were simulated as point charges, their small finite radius was neglected.

Chapter 4

Detector Simulations

4.1 Introduction

As already explained in the first chapter, two key properties are most relevant for γ-ray detector arrays for radioactive beam experiments – the relative energy resolution after Doppler correction and the full-energy-peak efficiency (FEP efficiency), which is defined as the probability to register a γ-ray, which is isotropically emitted into a solid angle of 4π, with its full energy in the detector. The simulations of the MINIBALL detector array have therefore been focused on these properties.
The simulation techniques described in section 3.5 were applied to determine basic properties of the detectors like their efficiency. Furthermore the main interaction concept was tested by investigating the deviation of the direction of γ-emission from the direction from the target to the exact position of the main interaction. Finally, fast algorithms to achieve a suitable position resolution inside the detector module were developed and energy resolution predictions were made for typical experiments leading to γ-emitting nuclei moving with several percent of the velocity of light. If possible, the simulated data were compared with their experimental equivalent to check the reliability of the simulations.

4.1.1 Full-Energy-Peak Efficiency

The FEP efficiency of a single MINIBALL module had already been investigated [Gun97, Fis97]. A reexamination became necessary in order to decide about the final shape of the MINIBALL 3-Cluster cryostat. Two different solutions, which

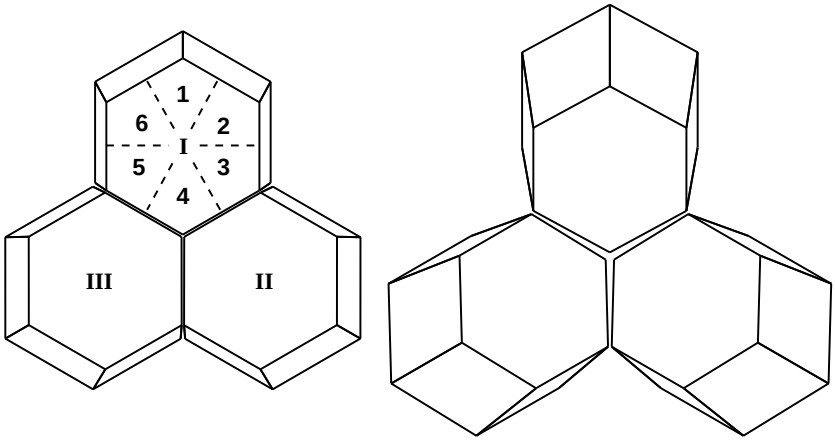

Figure 4.1: Schematic picture of an aligned 3-Cluster (left) and an on-target 3-Cluster (right). In the aligned 3-Cluster the segmentation of one crystal is shown and the numbering of the segments that was used for the simulations is indicated.

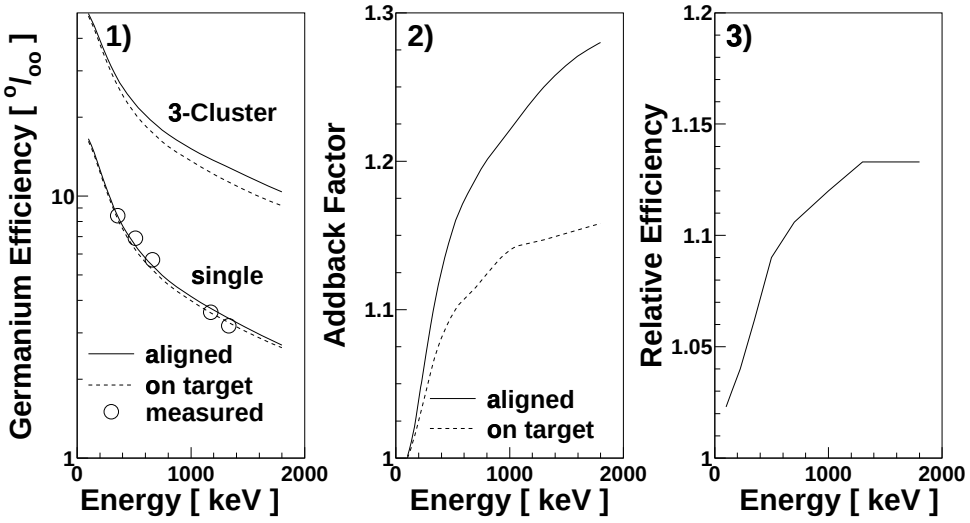

Figure 4.2: Comparison of the full-energy-peak efficiencies of an aligned 3-Cluster and an on-target 3-Cluster. The minimum MINIBALL target distance of 10.6 cm was used for the simulations and the measurement. A single on-target MINIBALL module was used for the measurements.
In panel 1 is shown that the single crystal efficiencies of the aligned geometry and the on-target geometry hardly differ, yet the improved addback of the aligned geometry results in a higher 3-Cluster efficiency. The addback factors of both geometries are shown in panel 2. The ratio of aligned 3-Cluster efficiency to on-target 3-Cluster efficiency can be seen in panel 3.

are shown in Figure 4.1, were suggested. The adopted solution was the "aligned" MINIBALL 3-Cluster. Here the cryostats were built for an ideal target distance[1] of 42 cm and the surfaces, where two crystals were facing each other, were in parallel. The idea to build an "on-target" 3-Cluster for the closest MINIBALL geometry with ∼11 cm target distance, where the centreline of each module aims at the target, was abandoned, because such a detector geometry was not useful for larger target distances and therefore unflexible.
As can be seen in the first panel of Figure 4.2, the FEP efficiency of a single detector module hardly differs for the two cryostats, but the addback factor, which is the ratio of the events which deposit their full energy in the MINIBALL 3-Cluster including inter-module scattering and the events which deposit their full energy in exactly one of the three modules, is significantly higher for the aligned 3-Cluster. In the aligned 3-Cluster up to 20% of all FEEs are event with a module multiplicity[2] above one, in the on-target 3-Cluster only up to 10%. Depending on the γ-ray energy the FEP efficiency of the aligned 3-Cluster is up to 13% higher than the FEP efficiency of the on-target 3-Cluster. However, this difference has not been important for the final decision, as the price for the higher efficiency are complications in the Doppler-shift correction algorithm, which will be studied in the following sections.

4.1.2 Doppler Correction

In radioactive beam experiments excited states of nuclei at high velocities are studied. In order to calculate the initial energy of the emitted γ-rays $E_{\gamma-0}$ an excellent Doppler-shift correction is needed. For the Doppler-shift correction,

$$E_{\gamma-0} = \gamma E_{\gamma-\mathrm{lab}}(1 - \beta\cos(\theta_\gamma)) \quad \text{with} \quad \gamma = \frac{1}{\sqrt{1-\beta^2}}, \tag{4.1}$$

the measured γ-energy $E_{\gamma-\mathrm{lab}}$, the velocity β of the reaction product, and the measured angle (in the laboratory system) θ_γ between the direction of γ-emission and the flight direction must be determined. Assuming that the γ-ray is emitted in close proximity of the target – the excited state must have a short lifetime of less

[1] The target distance is defined as the distance between the centre of the detector front plane (x=0, y=0, z=0) and the middle of the target.
[2] The module multiplicity is defined as the number of modules, which have fired.

than a nanosecond – and that β can be calculated from kinematic considerations as soon as the flight direction of the γ-emitting nucleus is known, the required values can be derived from the target position, the location, where the reaction products hit the particle detectors and the first interaction position of the γ-ray in the detector array. It is impossible though, to exactly determine these three locations, so that the Doppler correction of a γ-line becomes distributed over an energy interval. The width of this energy distribution defines the relative energy resolution after Doppler correction. In order to obtain the contribution of the germanium detector array to the energy resolution after Doppler correction, the intrinsic resolution of the germanium array is neglected and the velocity and flight direction of the γ-emitting nucleus and the target position are assumed to be well known. The obtainable relative energy resolution is then solely determined by the position resolution of the first interaction or, to be precise, by the angle θ_γ and the deviation $\Delta\theta_\gamma$ from its correct value. A formula for the relative energy resolution for a small deviation $\Delta\theta_\gamma$ can be derived from the first derivative of equation 4.1

$$\frac{\Delta E_{\gamma-0}}{E_{\gamma-0}} = \frac{\beta \sin(\theta_\gamma)}{1 - \beta \cos(\theta_\gamma)} \Delta\theta_\gamma. \tag{4.2}$$

In the main interaction concept, the approximate position of the first interaction is obtained by locating the main interaction. This concept has been tested by deriving $\Delta\theta_\gamma$, assuming that it was possible to exactly locate the main interaction in the germanium detector. As can be seen in Figure 4.3, $\Delta\theta_\gamma$ is not the angle between the direction of γ-emission and the direction from the target position to the main interaction, but the angle between the direction of γ-emission and the perpendicular projection of the direction from the target position to the main interaction onto the plane spanned by the nucleus flight direction and the direction of γ-emission[3]. For MINIBALL it is desired to achieve $\frac{\Delta E}{E} \leq 0.1 \times \beta$ – an energy resolution of 1% or better with a maximum β of 0.1 – even for the high efficiency setup with a minimum target distance of 10.6 cm. Under the most unfavourable conditions, which is θ_γ=90°, where $\frac{\Delta E}{E}$ has its maximum, the angular deviation must therefore be limited to $|\Delta\theta_\gamma| < 0.05$ rad (3 degrees). For a single MINIBALL module at a target distance of 10.6 cm this corresponds to a position resolution

[3]The reason for the projection is that the Doppler correction is only sensitive to this angle, a deviation in the perpendicular direction does not enter in the Doppler shift.

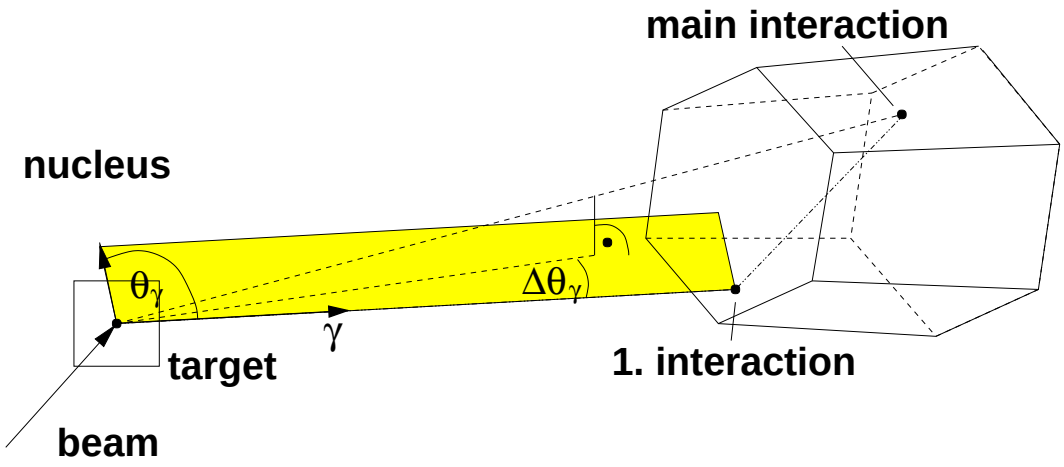

Figure 4.3: Deviation of θ_γ from its correct value, when the main interaction instead of the first interaction is used to determine the direction of γ-emission.

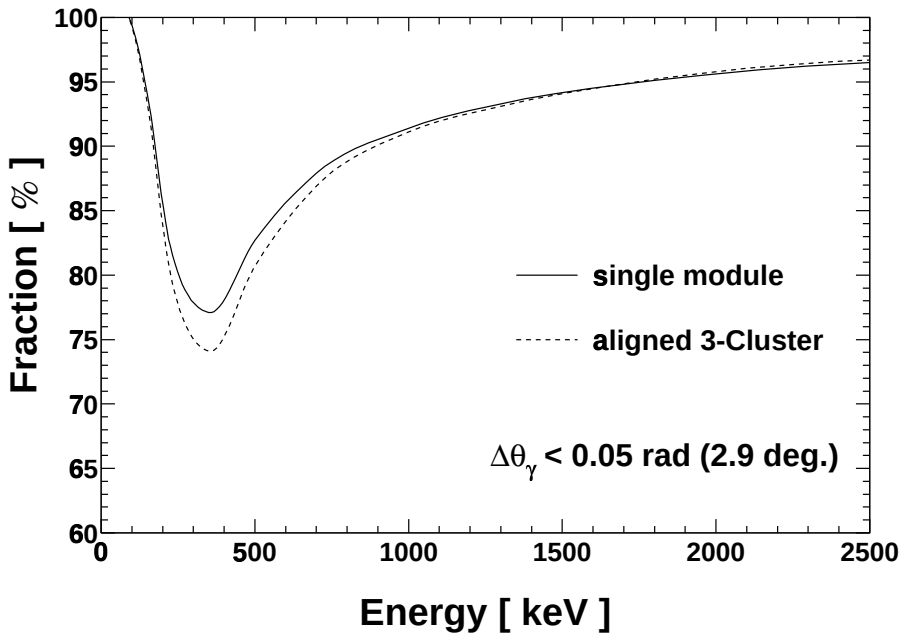

Figure 4.4: Theoretical granularity of a single detector module and of the aligned 3-module Cluster. The fraction of all FEE, where the approximation of the first interaction position with the main interaction position yields a $|\Delta\theta_\gamma| < 0.05$ rad, is shown.

on the front face of the detector of ±5 mm. The energy-dependent fraction of all full-energy events (FEE), which fulfill $|\Delta\theta_\gamma| < 0.05$ rad, is shown in Figure 4.4 for a single MINIBALL module and for the aligned MINIBALL 3-Cluster at the minimum target distance of 10.6 cm. Both curves hardly differ for energies below 200 keV and above 900 keV where more than 90% of all FEEs meet this requirement. In-between, at an energy of 350 keV, the single-module and the aligned-3-Cluster curves exhibit a minimum of 77% and 73%, respectively. As we can expect to obtain a good Doppler correction for at least three quarters of all events, the usability of the main interaction concept has been demonstrated.

4.1.3 The γ-ray Penetration Depth

The idealized assumption that it was possible to exactly locate the main interaction position (R, ϕ, z – see Figure 2.2) is unrealistic. The segmentation and pulse-shape analysis (PSA) only permit an approximate angle ϕ and radius R determination. The z-coordinate cannot be measured at all, although it is needed for the Doppler correction and the PSA. In the MINIBALL collaboration it has been extensively discussed, how an additional segmentation in z-direction could improve the detector performance, but finally it has been decided that the resources needed for the extended detector read-out would exceed the benefits of such a segmentation.

As the depth of the main interaction cannot be determined experimentally, the simulation of energy dependent mean depths of the first and the main interaction become necessary (upper panel of Figure 4.5). These mean depths are used instead of measured values, even though the width of the depth distribution has almost the same size as the mean depth itself. In the energy range between 0 keV and 500 keV the mean first and main interaction depths rise quickly with energy, for higher γ-energies only a moderate increase is encountered.

The depths of the first and main interaction are important for the PSA, as the pulses generated by charge carriers drifting in the "planar" front part of the detector ($z < 15$ mm) differ significantly from pulses generated by charge carriers in the rear "coaxial" part. The distribution of the first and main interaction depth in the "coaxial" and "planar" part is depicted in the lower panel of Figure 4.5. The mean depth of both the first and the main interaction is hardly affected, when the

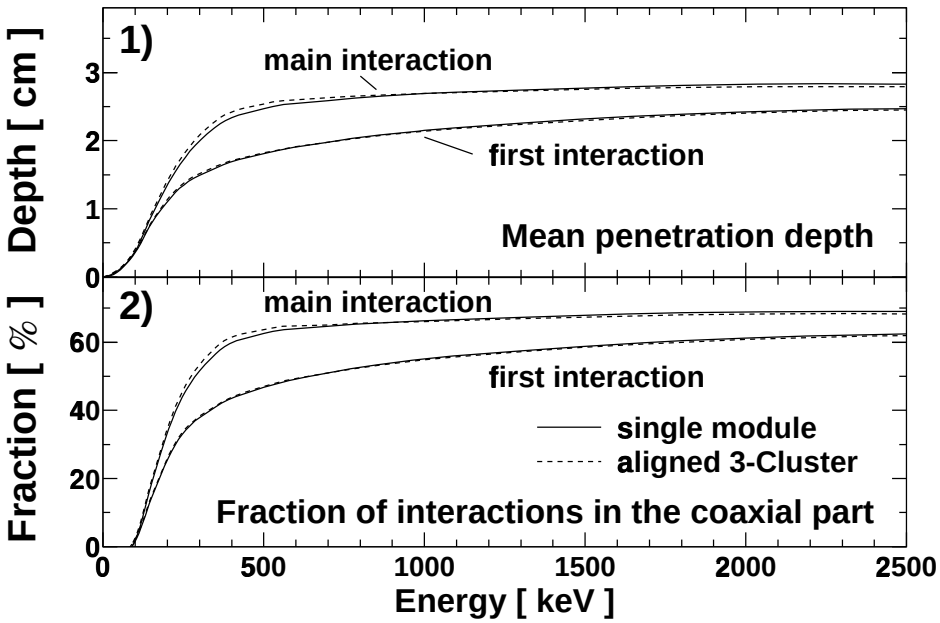

Figure 4.5: Penetration depth of the first and the main interaction for a single MINIBALL module and for the aligned MINIBALL 3-Cluster. In the first graph the average mean penetration depth of the first and the main interaction is shown. In the second frame the fractions of interactions which happen in the coaxial part of the detector ($z > 15$ mm) are shown. As usual, only FEEs are considered.

detector is slightly tilted (aligned and on-target geometry). Position dependent simulations have also revealed that the mean depths change only above the drilled hole of the inner contact and in the closest vicinity of the fringe of the detector. As these areas have a strongly reduced efficiency, the mean first interaction and main-interaction depths can be considered position and geometry independent. The replacement of the measurement of the main interaction depth by the average value of the first interaction depth[4] means a loss in position resolution, which can only be justified by the greatly enlarged costs for the z-segmentation.

4.1.4 Energy Resolution as a Function of Position Resolution

Before the angular and radial resolution algorithms are discussed in detail, it is important to find out, how the energy resolution after Doppler correction is

[4]One should remember that the main interaction is the interaction, which can be located, while the first interaction is the interaction, one wants to locate.

influenced by the radial and angular resolution. For this purpose the Doppler correction and the resulting energy spectrum have been simulated for a single MINIBALL module at a target distance of 10.6 cm for varying radial and angular resolutions. The values of the radius R_0 and its resolution ΔR_0, as well as the angle ϕ_0 and its resolution $\Delta\phi_0$, are given with respect to the detector frontal plane ($z = 0$ mm), corresponding to the γ-ray entry position into the detector. The radius and angle values used for the Doppler correction have been obtained by adding Gaussian distributed errors with the defined width to the angle and the γ-ray entry radius. As the main-interaction depth cannot be measured, it is assumed that the radius algorithm suffers from an additional broadening of the resolution, which is already included in the simulated radius resolution values – the angle algorithm is not affected, as the single module is aligned with respect to the target direction, so that the angle is independent of the depth.
Measurements of the radial resolution [Gun97] have revealed that the radial resolution is hardly angle or radius dependent (for radii outside the drilled core hole). The radial resolution ΔR_0 is therefore assumed to be independent of the position. As no such data are available for the angular resolution, the simulations have been performed for two different assumed angular resolutions. On one hand simulations have been made for a constant angular resolution $\Delta\phi_0$, on the other hand they have been performed for a constant arc-length resolution $R_0 \cdot \Delta\phi_0$, corresponding to an angular resolution, which improves with radius.
In Figure 4.6 the position-resolution-dependent energy-resolution is shown for a 1 MeV γ-ray emitted by a nucleus with a velocity of β=0.065. It is assumed that a single detector module is positioned at a distance of 10.6 cm from the target at an angle ϑ_{det}=90° and that the nucleus travels in parallel to the beam, so that the most unfavourable detection angle θ_γ=90°, where $\frac{\Delta E}{E}$ has its maximum (see equation 4.2), is obtained. The left plot shows the energy resolution as a function of the radial resolution ΔR_0 and angular resolution $\Delta\phi_0$, the right plot displays the energy resolution as a function of the radial resolution ΔR_0 and the arc-length resolution $R_0 \cdot \Delta\phi_0$. While the size of a ΔR_0-$\Delta\phi_0$-section grows linearly with radius, the size of a ΔR_0-$(R_0 \cdot \Delta\phi_0)$-section is constant and therefore comparable to a standard Cartesian Δx-Δy-section. Both plots show a similar behaviour, the contours of constant energy resolution are elliptical. Hence the

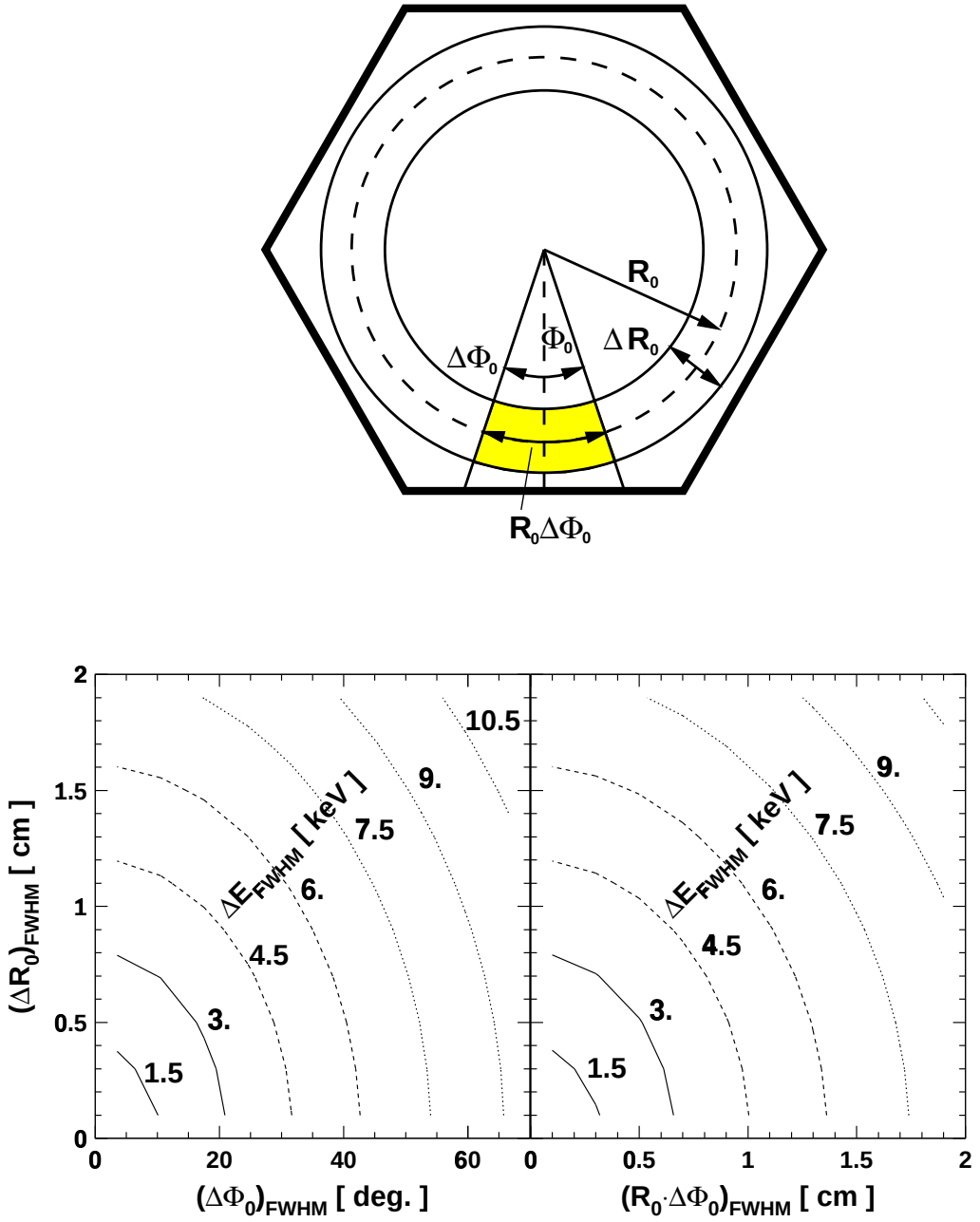

Figure 4.6: Energy resolution ΔE_{FWHM} of a 1 MeV γ-line after Doppler correction as a function of the radial and angular or arc-length resolution. It is assumed that the detector is positioned 10.6 cm away from the target at an angle of ϑ_{det}=90° with respect to the beam and that the γ-emitting nucleus, which has a velocity of β=0.065, travels in parallel to the beam, so that θ_γ=90° is obtained. The intrinsic energy resolution of the germanium detector is neglected in the simulation. A sketch is shown on top explaining the quantities involved.

energy resolution shows little improvement, if the better of the two directional resolutions is improved. The best energy resolution results can be achieved for comparable directional resolutions.

4.2 Radius Information

4.2.1 The Steepest-Slope Algorithm

Operation of the algorithm

With the aid of Figure 4.6 it is now possible to estimate the energy resolution for a known radial and angular resolution. In order to obtain such resolutions it is necessary to develop a radius and an angle algorithm using the segment energies and pulse-shape analysis (PSA). At first the radius algorithm will be discussed. Different algorithms to obtain a radial resolution have already been developed, discussed, and compared [Gun97]. All these algorithms rely on a PSA of the centre-contact signal. The best of these algorithms, the steepest-slope algorithm developed by Palafox [Pal97], will be presented here in brief, a full presentation of radius algorithms can be found in the references above.

Looking at the schematic detector pulses of single-interaction events in a true coaxial detector (the core hole fully penetrates the detector), shown in Figure 4.7, the radius dependence is immediately evident. For a small interaction radius the electrons quickly reach the central contact, while the holes take a long time to arrive at the outer electrodes, for large radii it is the other way around. Due to the differences of the core weighting potential at the core and the outer contacts the current drop is significantly larger when the electrons arrive at the central contact than when the holes arrive at the outer contact. It is therefore possible to distinguish between electrons and holes and to determine the time, when the electrons reach their contact.

The detector pulses are integrated, shaped, and digitized by the preamplifier and the XIA-module (see Figure 2.5) and finally the ADC charge pulse (panel 2 in Figure 4.7) is obtained. Due to the extensive signal shaping in the electronics one cannot be sure whether the radius information is still contained in this pulse. In order to detect a sharp drop of the initial detector pulse, an approximate detector

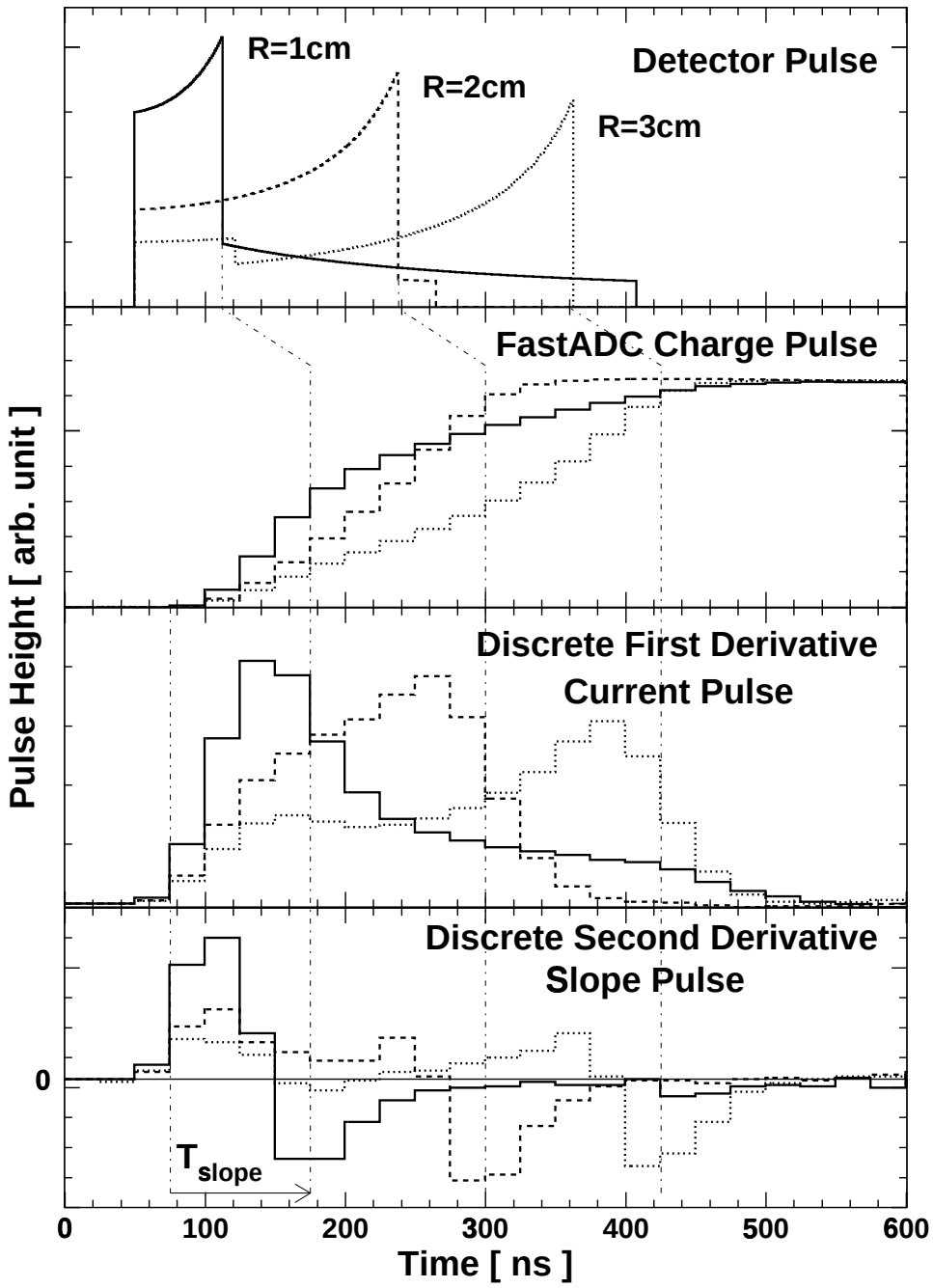

Figure 4.7: The Steepest-Slope Algorithm to obtain a radial resolution. To explain the method, single interaction events are assumed. The time-to-steepest-slope T_{slope} is drawn for a crude algorithm which does not include interpolation of intermediate values.

pulse (current pulse) has to be calculated. This pulse is obtained by taking differences of neighbouring FastADC samples (sample[i+1]-sample[i]), as can be seen in the third panel. The drops when charge carriers arrive at their corresponding contacts have been transformed into slopes, which become steeper, the higher the initial drop was. In order to determine its steepest slope the absolute minimum in the second derivative of the sampled pulse is calculated. The discrete second derivatives (sample[i+1]+sample[i-1]-2·sample[i]) display such minima (lower panel). The time of the absolute minimum coincides with the time of the highest drop of the initial detector pulse, the shift between the two times is caused by the rise times of the electronics, which are included in the simulations.
As the electron drift velocity in the detector is almost constant (for high electric fields the velocity approaches a limit, see Figure 3.4), the time-to-steepest-slope T_{slope}, which is defined as the time difference between the start time of the pulse[5] and the time, when the second derivative reaches its absolute minimum (the time when the electrons reach the inner contact), is proportional to the length of the drift path of the main interaction electrons. Since furthermore the length of the electron drift path scales with the interaction radius, the time-to-steepest-slope T_{slope} allows to determine an approximate interaction radius R.
However, a FEE usually consists of multiple interactions and several electron- and hole-drops occur. In this case the steepest slope is caused by the electrons of the main interaction. An approximate first interaction radius R_1 can nevertheless be obtained, because the first and the main interaction are usually located "close together" (Figure 4.4).

Potentials of the Algorithm

The considerations in the last section have shown that a radius determination by PSA of the core pulse seems possible. Hence the simulation techniques outlined in chapter 3 have been used to study the correlation between the first interaction radius R_1 and T_{slope} and the influence of various detector properties (impurity concentration, anisotropy of the drift velocity, detector geometry) on this correlation.

[5] the time of the first sample of the pulse, which is larger than zero.

For this purpose the irradiation of a single MINIBALL module was simulated with a point-like isotropic source positioned 10.6 cm away from the centre of the detector frontal plane. For each FEE the core pulse was calculated and T_{slope} was extracted using interpolation methods[6], furthermore basic geometric data like the first interaction radius R_1 (compare with the upper panel of Figure 4.8) and the distance between the first interaction and the centreline of the core contact[7] D_1, which were not directly accessible experimentally, were derived from the GEANT data. The pairs (R_1,T_{slope}) and (D_1,T_{slope}) were then filled in two-dimensional histograms for correlation studies.

At first, the dependence of the radial resolution on the variation of the drift velocity due to varying electric fields has been studied. For this purpose the electric fields of the low-impurity and the high-impurity detector has been used for the pulse calculations and the isotropic fit has been used for the electron drift velocity. As the D_1-T_{slope}-correlation plots for the two detectors, which are shown in panel 1 and panel 2 of Figure 4.8, display a very fine, linear, almost identical correlation line, one can be assured that in general the first and the main interaction are located close together and that the drift velocity does hardly depend on the electric field in the detector. The use of an "average" detector is validated.

Subsequently the dependence of the radial resolution on the anisotropy of the electron drift velocity has been investigated. For this purpose the "average" detector has been used for the pulse calculations and the D_1-T_{slope}-correlations have been compared for a simulation with and without an anisotropic electron drift velocity. The correlation line for the isotropic fit – panel 3 – is identical with the ones in panel 1 and 2, as expected; the correlation plot for the anisotropic fit – panel 4 – exhibits a considerable broadening for large D_1 and T_{slope} values. One therefore has to expect that the anisotropy of the electron drift velocity will limit the radial resolution of the MINIBALL modules.

Finally the influence of the "planar" part of the MINIBALL module on the radial resolution has been determined. For this purpose the "average" detector and an

[6]The pulse start was obtained from a linear extrapolation to 0 of the first two charge pulse samples with a value >0, the electron arrival time was obtained from a quadratic interpolation of the discrete second derivative curve in the minimum.

[7]In contrast to R_1, which does not scale linearly with the electron drift path for z <20 mm, D_1 always scales linearly with the length of the drift path of the electrons

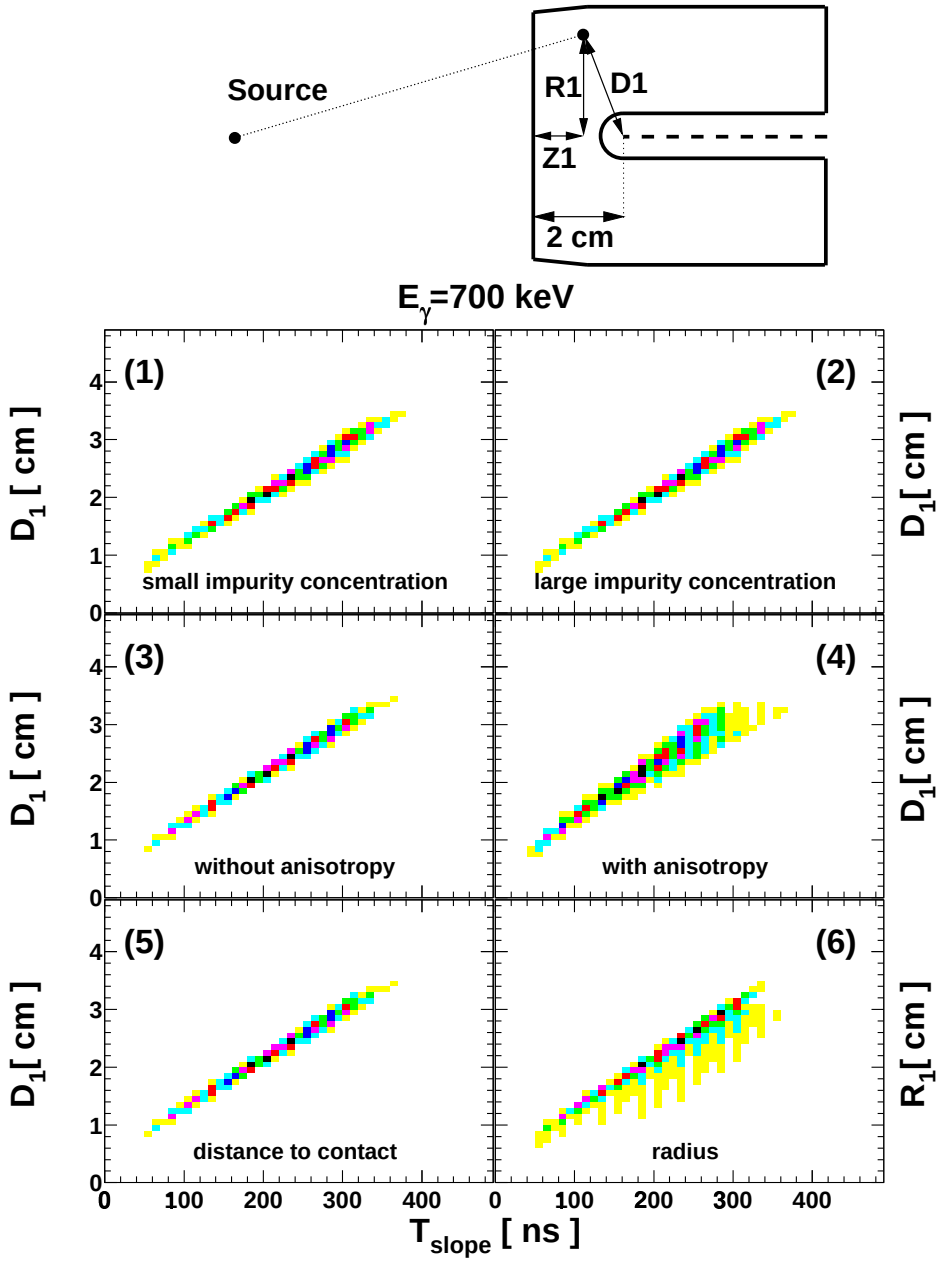

Figure 4.8: Studies of the correlation between R_1 and T_{slope} and between D_1 and T_{slope} for different detector properties. In the pictures (1) and (2) the D_1-T_{slope}-correlation is shown for a bias voltage of 3500 V and an impurity concentration of $5\times10^9\mathrm{cm}^{-3}$ and for a bias voltage of 4000 V and a linear radial rise from $7\times10^9\mathrm{cm}^{-3}$ to $20\times10^9\mathrm{cm}^{-3}$, respectively (isotropic simulation). In picture (3) the D_1-T_{slope}-correlation is displayed for an isotropic simulation of the "average" detector. It is compared with the same correlation but an anisotropic simulation (panel 4). In the graphs (5) and (6) the D_1-T_{slope}-correlation and the R_1-T_{slope}-correlation are compared for the "average" detector (isotropic simulation).

isotropic fit of the electron drift velocity have been used for the pulse calculations and the D_1-T_{slope}-correlation (panel 5 of Figure 4.8) has been compared with the R_1-T_{slope}-correlation (panel 6). As D_1 exceeds R_1 for events in the "planar" part of the MINIBALL module and as D_1 correlates linearly with T_{slope}, the R_1-T_{slope}-correlation plot shows the sharp correlation line of events in the "coaxial" part of the detector and a smeared out "shadow" at reduced radii, which corresponds to events in the "planar" part of the module. As D_1 exceeds R_1 in the "planar" part of the MINIBALL module, the radial resolution will also be limited for this geometric reason.
It has been shown that a good correlation between R_1 and T_{slope} is obtained. The mechanisms, which limit the radial resolution of the steepest-slope algorithm, have been deduced:

- The spatial distance between the first and the main interaction, which is a fundamental problem of all algorithms relying on the main interaction concept.
- The anisotropy of the electron drift, which is a material property.
- The difference between the drift path length D_1 and the radius R_1 in the "planar" part of the MINIBALL module, which is related to the detector geometry.

Now the results from the simulations have to be verified in experiment.

Radial Resolution for Perpendicular Irradiation

In order to test the steepest-slope algorithm an experimental verification was required. Yet for such a measurement the problem of an undetermined first interaction depth z_1 still had to be overcome. It was therefore impossible to use a point source with an isotropic irradiation, as the first interaction radius then scaled with the first-interaction depth. However, the problem could be avoided, when the detector frontal plane was perpendicularly irradiated with a collimated source, as can be seen in Figure 4.9. In this case the collimator position, the γ-ray entry radius R_0, and the first interaction radius R_1 were identical.
In Figure 4.9 a two-interaction event is shown, which demonstrates the geometric

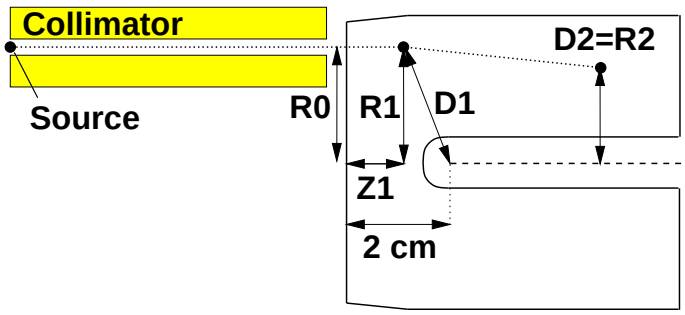

Figure 4.9: Collimated irradiation of a single MINIBALL module. A two-interaction event with the first interaction in the planar and the second interaction in the coaxial part of the detector is shown.

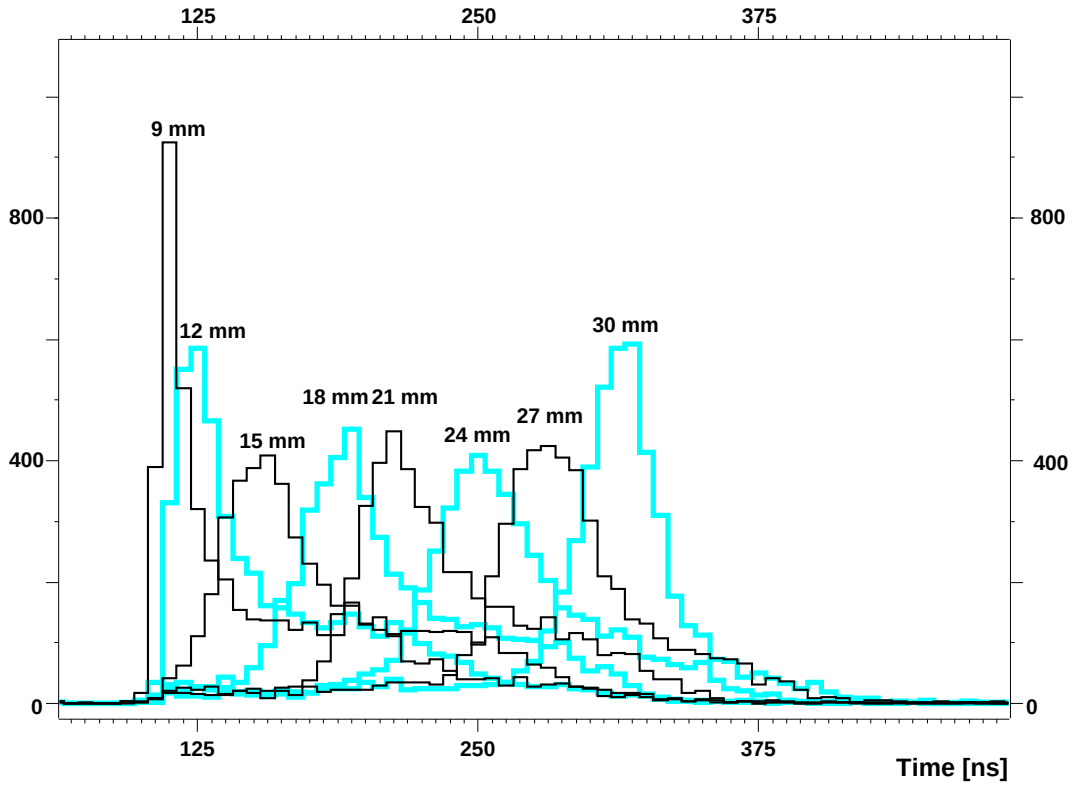

Figure 4.10: First interaction radius resolution of the steepest-slope algorithm for a γ-ray of 662 keV. The collimator used has a beamspot diameter of $\approx$2.5 mm. The incident beam has been perpendicular to the detector front plane. The preamplifier pulses have been sampled with the XIA electronic modules and the steepest-slope time has been extracted using interpolation methods. The time distributions measured for first interaction radii smaller than 9 mm are omitted as they hardly differ from the distribution at 9 mm and at 12 mm. The data have been taken and evaluated at the Universität zu Köln [Wei].

mechanisms, which will cause a broadening of the radial resolution, when the steepest-slope algorithm is used in such an irradiation geometry:
Assuming that the first interaction is the main interaction, the radius of the first and main interaction are identical (R_1=R_{main}), yet T_{slope} measures the drift path of the electrons, which scales with the distance of the main interaction to the inner-contact centreline[8] (D_{main}=D_1). As the first interaction happens in the "planar part" of the detector, D_1 is larger than R_1, so that the radius in the "planar" part is overestimated. The problem is most pronounced for small radii and small main interaction depths and ceases to exist, as the main interaction depth reaches 2 cm.
Assuming that the second interaction is the main interaction, the radius difference stems from the spatial distance between the first and the main interaction. However, the main interaction occurs in the coaxial part of the detector, so that D_2 and R_2 are equal. Here the broadening of the radial resolution exclusively stems from the distance between the first and the main interaction.
Two more types of FEEs remain: For events, where the first and the main interaction coincide and happen in the coaxial part of the detector, the steepest-slope algorithm gives optimum results. In contrast, for multiple-scattering FEE, where the main interaction is not the first interaction and which have their main interaction in the planar part of the detector, only a moderate radial resolution is obtained.
The most recent measurements of the radial resolution using the steepest-slope algorithm have already been performed with the new XIA-module [Wei], however not yet in real time, as the algorithms are not yet implemented on the DSP of the XIA cards (i.e. full detector pulses were read out and analyzed off-line). In Figure 4.10 the time-to-steepest-slope distributions are shown for a set of irradiation radii with a distance of 3 mm between neighbouring irradiation points. Only a poor radial resolution is achieved for small irradiation radii below 12 mm, as the charges in front of the drilled core hole mainly drift in z-direction. For larger radii an equally spaced separation is observed; the radius scales linearly with T_{slope}. All time distributions exhibit a large tail to longer steepest-slope times, corres-

[8] As no interactions can take place inside the core hole of the detector, a drift time of 0 ns corresponds to a D of 5 mm.

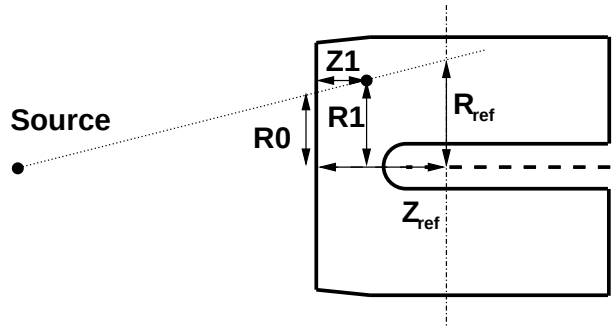

Figure 4.11: Radius assignment for a given reference depth. The first interaction position determines the direction of γ-ray emission. If the first interaction depth z_1 is unknown, the reference radius R_{ref} has to be assigned to a given reference depth z_{ref}. The plane, which corresponds to the given reference depth is drawn as a dash-dotted line.

ponding to events, where the main interaction is located in the planar part of the detector. For a perpendicular irradiation a radial resolution of about $6 - 8$ mm (FWHM) has been measured for radii above 12 mm.
The feasibility of the steepest-slope algorithm has been demonstrated in simulation and experiment. The algorithm gives very good results, except in front of the drilled core hole of the detector, which corresponds to a very small part of the detector. For larger radii T_{slope} scales almost linearly with the first interaction radius R_1 allowing an easy extraction of the radius.

4.2.2 Radial Resolution in MINIBALL experiments

The Reference Depth

Until now, the radial resolution has only been discussed for the first interaction radius R_1. In MINIBALL, however, the first interaction radius is not sufficient to determine the direction of a γ-ray, as the photons are not incident perpendicularly on the detector and the first interaction depth z_1 cannot be accessed. For to obtain an approximate γ-ray direction an assumption about the first interaction depth z_1 has to be made and a reference depth z_{ref} has to be assigned (see Figure 4.11). In order to determine the radial resolution in the simulation for an irradiation geometry with a point-like source, a new radius called the reference radius R_{ref}

has to be introduced[9]. This reference radius is the radius coordinate of the point, where the line defined by the γ-ray direction intersects the z_{ref}-plane, i.e. the first interaction position is shifted along the γ-ray direction, until it reaches the assigned depth.
If the R_{ref}-T_{slope}-correlation is now studied instead of the R_1-T_{slope}-correlation, the the radial resolution of the steepest-slope algorithm for a fixed reference depth can be obtained. At this point the concept of the reference depth z_{ref} might not seem very useful, however, as will be shown later, only by assigning appropriate values to z_{ref} a good correlation between R_{ref} and T_{slope} can be retained[10]. The concept of the reference depth will now be applied to simulate the radial resolution of a single MINIBALL module and of the aligned MINIBALL 3-Cluster for an irradiation geometry with a point-like isotropic source.

Radial Resolution in a Single MINIBALL Module

The radial resolution of a single MINIBALL module has been simulated for an isotropic irradiation with a distance of 10.6 cm to the source. The source has been aligned with respect to the module centreline (left panel in Figure 4.12). Two reference depths have been selected. In Figure 4.13 panel 1 the R_{ref}-T_{slope}-correlation is shown for z=0 as the reference depth (the detector frontal plane), in panel 3 the mean first interaction depth $\langle z_1 \rangle$ has been selected as the reference depth. Both correlation plots exhibit a clear correlation. Therefore the radial resolution, which can be obtained with the steepest-slope algorithm, does not depend on the reference depth for this irradiation geometry. The unknown first interaction depth has added considerably to the width of the correlation line; the line has transformed into a band. A linear fit has been applied to this plot in order to obtain a correlation function for the radius, resulting in

$$R(T_{\mathrm{slope}}) = 0.00992 \frac{\mathrm{cm}}{\mathrm{ns}} \cdot T_{\mathrm{slope}} + 0.188\,\mathrm{cm}.$$

With the aid of this correlation function the radial resolution has been obtained. The time width ΔT has been taken for a constant radius, then the radial reso-

[9] The concept of a reference depth has already been used in section 4.1. Here the detector frontal plane (z_{ref}=0) has been used as the reference depth and the γ-ray entry radius as the reference radius (R_0=R_{ref}).

[10] The reason for this behaviour is the tilted geometry of for instance the 3-Cluster.

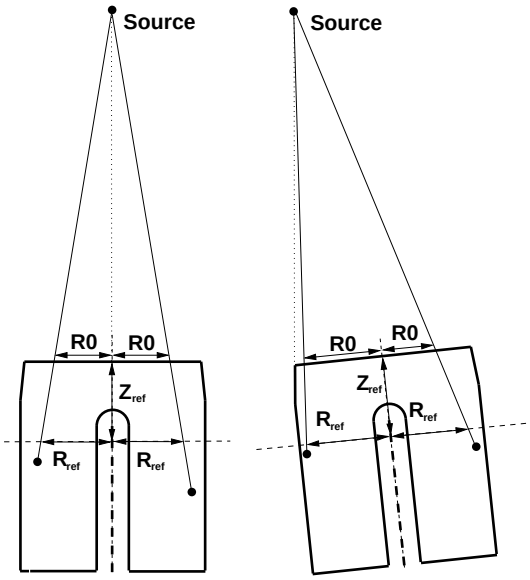

Figure 4.12: Irradiation geometry for a single MINIBALL module and for the aligned 3-Cluster. The source is aligned with the module centreline for a single module and with the edge of the corner, where all 3 modules touch, for the aligned 3-Cluster. The assigned radii are shown assuming the detector frontal plane as reference depth – R_0 – and assuming a reference depth z_{ref} inside the detector – R_{ref}.

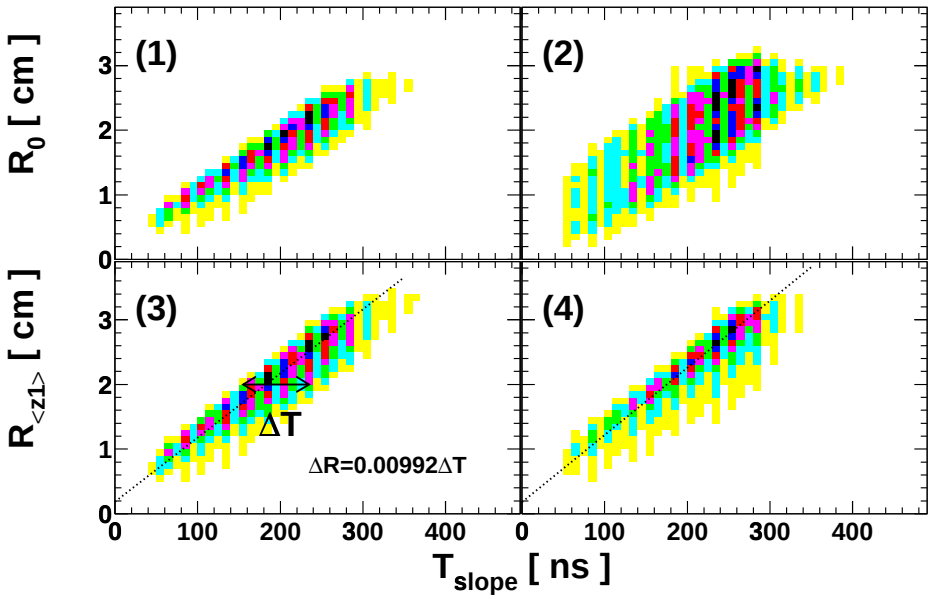

Figure 4.13: R_{ref}-T_{slope}-correlation plots for z=0 as the reference depth (R_0) and for the mean first interaction depth as the the reference depth (z_{ref}=$\langle z_1 \rangle$). Panels 1 and 3 correspond to the single module, panel 2 and 4 to the 3-Cluster irradiation geometry. Linear fits corresponding to the $R_{\langle z_1 \rangle}$-T_{slope}-correlation are added in panel 3 and 4. These fits are used in the following simulations.

lution has been calculated using

$$\Delta R = 0.00992 \frac{\text{cm}}{\text{ns}} \cdot \Delta T.$$

A radial resolution with an estimated width of about 8 mm (FWHM) is obtained from the simulation at a radius of 2 cm.
The simulations for the single MINIBALL module have shown, that the missing information about the first interaction depth adds considerably to the width of the radial resolution. The selection of a reference depth is necessary, as the real first interaction depth is unknown, but the precise value of the selected reference depth is unimportant.

Radial Resolution in the aligned MINIBALL 3-Cluster

The MINIBALL modules will not be used independently, but mainly in aligned 3-Clusters. Therefore, the radial resolution of the aligned MINIBALL 3-Cluster has been simulated for an isotropic irradiation with a distance of 10.6 cm to the source[11]. In this geometry the source is not aligned with respect to the modules' centreline, but with respect to the edge in the middle of the Cluster, where all three modules touch. From the right panel in Figure 4.13 it is immediately evident that for this geometry the reference depth is *very* important. Considering the right panel of Figure 4.12 explains why; even though both events shown have different γ-ray entry radii, there exists a reference depth, where both reference radii are equal. Due to the misalignment the left side and the right side of the module are no longer equal. The R_{ref}-T_{slope}-correlation becomes dependent on the ϕ-direction in the module.
If one selects the detector frontal plane (z=0) as the reference depth, the effect is very strong. As can be seen in panel 2 of Figure 4.13 a very poor R_0-T_{slope}-correlation is obtained, as long as the strong ϕ-dependence of the correlation is neglected. There are two possible remedies for this problem. One could evaluate the radius-time-correlation for every angle ϕ separately, but such an approach is extremely tedious and complicated and it would require an angle-dependent correlation function. The idea of the other approach is, to minimize the influence of the ϕ-direction by selecting an optimized reference depth. The best results are

[11] The distance is measured from the middle of the detector frontal plane (R=0, ϕ=0, z=0).

expected for a reference depth, which minimizes the mean distance between the real first interaction position (R_1, z_1) and the corresponding reference position (R_{ref}, z_{ref}) for all FEEs. For this reason the mean first interaction depth $\langle z_1 \rangle$ is selected as the reference depth. As can be seen in the fourth panel of Figure 4.13, the width of the $R_{\langle z_1 \rangle}$-T_{slope}-correlation is much smaller than the one of the R_0-T_{slope}-correlation. From the correlation plot a correlation function is obtained:

$$R(T_{\mathrm{slope}}) = 0.0104 \frac{\mathrm{cm}}{\mathrm{ns}} \cdot T_{\mathrm{slope}} + 0.182\,\mathrm{cm}$$

A radial resolution with a FWHM of about 11 mm is expected from the simulation for a radius of 2 cm.

In the aligned 3-Cluster the misalignment of the modules with respect to the target results in different correlations for different segments. With the selection of $\langle z_1 \rangle$ as the reference depth it nevertheless remains possible to achieve a reasonable radial resolution without knowledge of the angle ϕ, so that an angular dependence in the radius algorithm can be avoided.

Energy-Dependent Radial Resolution

For both irradiation geometries and a set of γ-ray energies the correlation functions $R(T_{\mathrm{slope}})$ were derived. The correlation functions were used to obtain the energy-dependent radial resolution of the steepest-slope algorithm as shown in Figure 4.14. The difference between the exact reference radius R_{ref} and the calculated radius $R(T_{\mathrm{slope}})$ was evaluated on an event-by-event basis and filled in a one-dimensional histogram. The radius resolution values were obtained from Gaussian fits to these histograms. It should be noted, that for each energy the radial resolution was given with respect to the (energy-dependent) mean first interaction depth.

At low γ-energies the radial resolution of both the single module and the 3-Cluster exhibits excellent resolution values below 7 mm, then the curves quickly rise until they reach their maximum at around 350 keV. Here poor radial resolution values of 1.1 cm and 1.4 cm, respectively are obtained. For higher energies both curves show an exponential-like decrease as a limiting resolution of about 6 mm is approached at 2.5 MeV.

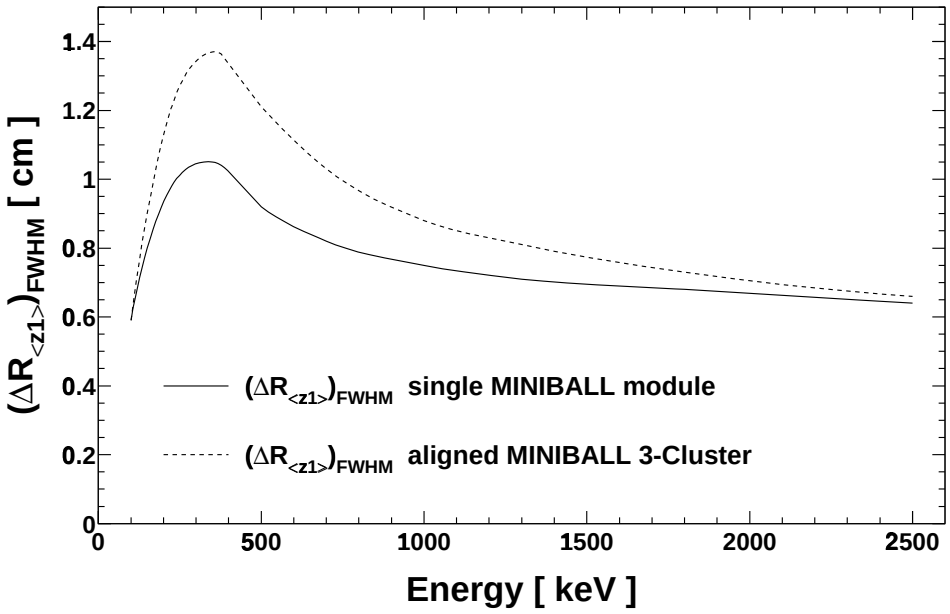

Figure 4.14: Simulated energy-dependent radial resolution of a single MINIBALL module and the aligned MINIBALL 3-Cluster.

It has been shown in the simulation that the steepest-slope algorithm can give a reasonable radial resolution for both the single MINIBALL module and the aligned 3-Cluster (compare with Figure 4.6). The resolution is energy dependent and has its maximum in the region of 350 keV, the energy range, where the main interaction concept itself has its weakness. The resolution is determined by the distance between first and main interaction, the lattice-dependent anisotropy of the electron drift velocity in germanium, the geometry of the detector module (planar part, coaxial part), and the irradiation geometry. The missing information about the interaction depth results in a reduced radial resolution. The radius is obtained from the time-to-steepest-slope T_{slope} with the aid of a correlation function $R(T_{\mathrm{slope}})$, which can be obtained from the correlation plot. One now has to discuss, how the results from these simulations can be used in experiments. In particular, it has to be discussed how the correlation function can be obtained experimentally.

Application of the Steepest-Slope Algorithm

While it is very easy to obtain the R_{ref}-T_{slope}-correlations in the simulation, it is extremely tedious to measure them. One has to use a collimated source at the correct irradiation angle. A vast amount of measurements at different positions and with γ-sources at different energies are necessary. Furthermore there is a high risk that errors in the positioning of the collimator will result in errors in the correlation plot and finally in the correlation function. Therefore another approach is suggested.

The correlation plot is unimportant for the Doppler correction, only the correlation function is needed to calculate the radius from the measured T_{slope}-value. The sole purpose of this correlation function is, to permit a good energy resolution after Doppler correction. Therefore an in-beam experiment with a known nucleus is proposed to obtain the correlation function $R(T_{\mathrm{slope}})$ for each module. In the experiment the γ-singles are recorded (γ-energy, T_{slope}, angular information) for an offline-evaluation. In the offline analysis a linear correlation function

$$R(E_{\gamma-\mathrm{lab}}, T_{\mathrm{slope}}) = a(E_{\gamma-\mathrm{lab}}) \cdot T_{\mathrm{slope}} + b(E_{\gamma-\mathrm{lab}})$$

is assumed for each excitation energy E_γ of the nucleus ($E_{\gamma-\mathrm{lab}}$ has to be calculated for each detector using the inverse Doppler correction) and the parameters $a(E_{\gamma-\mathrm{lab}})$ and $b(E_{\gamma-\mathrm{lab}})$ are varied until the energy resolution after Doppler correction reaches a minimum for the corresponding excitation energy. For the reference depth the simulated mean first interaction depth can be used[12]. Finally an energy dependent correlation function for arbitrary energies $R(E_{\gamma-\mathrm{lab}}, T_{\mathrm{slope}})$ is obtained by interpolating the parameters a and b for the required energy.

There are three requirements for this experiment:

- The flight direction of the γ-emitting nucleus must be well defined (better than 2 degrees), the reaction of a heavy projectile with a light target is therefore recommended.

- A sufficient Doppler-shift of the emitted γ-rays is needed – a velocity of the reaction products of $\beta > 5\%$ is recommended.

[12] As the GEANT simulations are more reliable than the pulse simulations, the basic angle assignment algorithm can be directly used for the analysis of the experiment, whereas the correlation function must be determined in experiment.

- The reaction products must be excited into several short-lived states, which cover the full range of γ-energies.

The proposed method was used for the radius determination of the experiment described in chapter 5. Here the parameters for the correlation function $R(E_\gamma, T_{\text{slope}})$ could only be deduced for an excitation energy of 646 keV. Hence the radius assignment was limited to the energy region between 600 keV and 700 keV, where a constant extrapolation of the parameters a and b seemed reasonable.

4.3 Angular Information

4.3.1 The Single Crystal

The Basic Angle Assignment Algorithm

In order to locate γ-rays within the detector the radial information is not sufficient, since the angle ϕ is still unknown. While the radius information is derived from PSA of the detector core contact, the angular information is contained in the segment pulses. The angle assignment in the MINIBALL module is a two-step process. First a coarse angle, either the middle line of a segment or the segmentation line between two segments, is selected. If possible the coarse angle is refined in a second step.

The assignment of the coarse angle ϕ_{coarse} is based on the analysis of the energy pattern of the segments. Possible first interaction positions are limited to the hit segments. In order to develop an angle algorithm the segment response of a single 6-fold segmented module has therefore been evaluated on a grid of γ-ray entry points with a distance of 1 mm in both the x- and the y-direction (see Figure 4.15). One simulation has been made with the isotropic single-module irradiation geometry, where the source has been positioned 10.6 cm away from the detector and aligned with respect to the module's centreline. In the other simulation the module has been irradiated perpendicularly. It should be noted that in contrast to the radius coordinate, the angle coordinate is not depth dependent for both irradiation geometries. The first interaction angle ϕ_1, the γ-ray entry angle ϕ_0 and the reference angle ϕ_{ref}, which is defined as angle coordinate of the point, where the direction of γ-ray emission intersects the z_{ref}-plane, are the same for

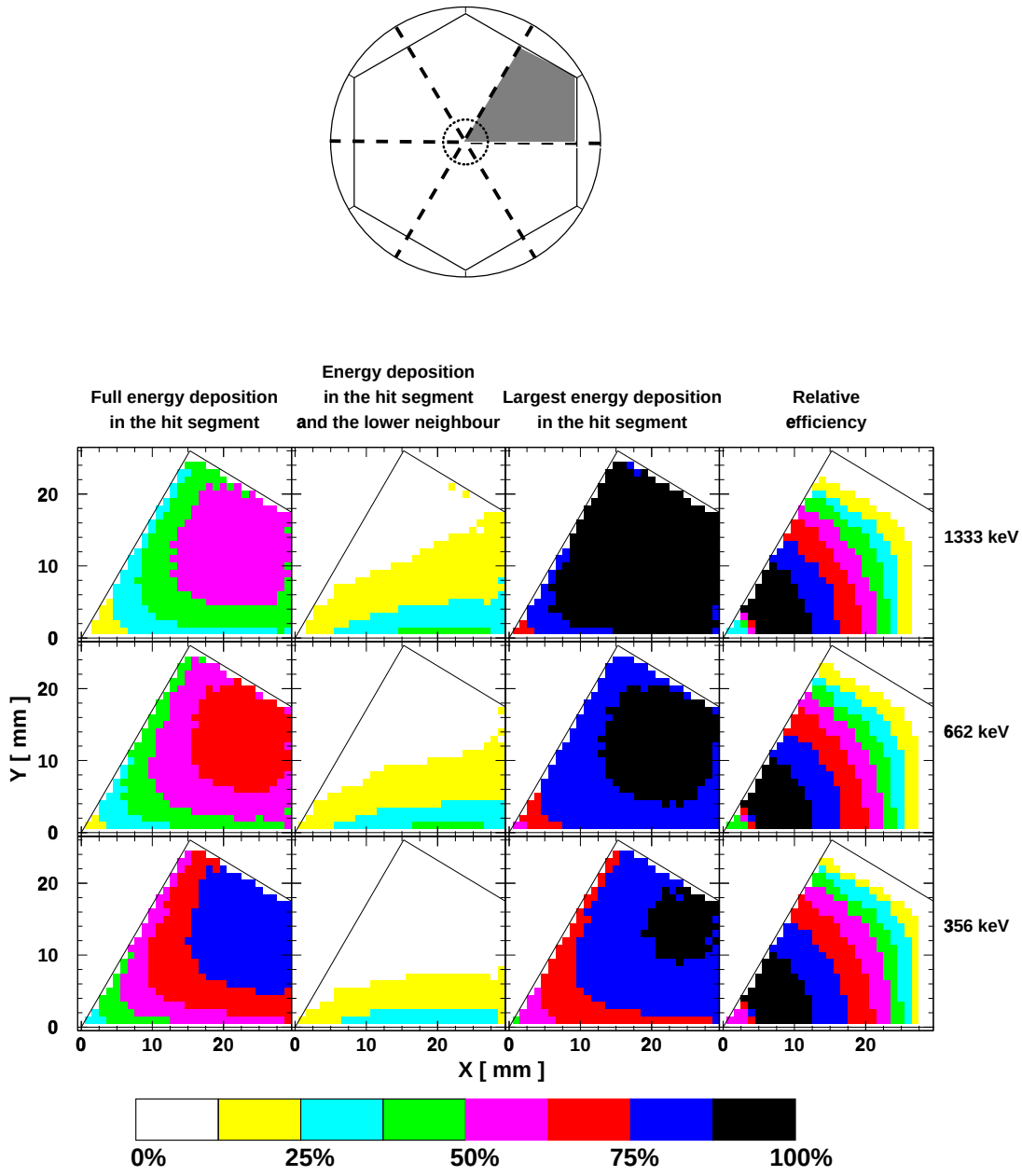

Figure 4.15: Position dependent segment response for γ-ray entry positions on a 1 mm grid for a single MINIBALL module. The source has been positioned 10.6 cm away from the detector. It has been aligned with respect to the module's centreline. The fraction of FEEs, for which all the energy is deposited in the entry segment, the fraction, for which the energy is deposited in the entry segment and in the lower neighbour, and the fraction, for which the energy deposition in the entry segment is larger than in any other segment, is shown for energies at 356, 662, and 1333 keV. In addition the relative FEP efficiency of the single MINIBALL module is shown (The definition can be found in the text.).

both irradiation geometries. As it is very tedious to confirm the simulations for every position calculated, the results have been verified for a few positions only using collimated sources and the perpendicular irradiation [Gun97, Fis97].
The following quantities have been determined in the simulations:

- The fraction of module FEEs, which deposit all their energy in the entry segment.
- The fraction of module FEEs, which spread their energy between the entry segment and the lower neighbour segment.
- The fraction of module FEEs, which deposit the largest amount of energy in the entry segment.

The results of both simulations are similar, therefore it has been decided to only discuss the results of the simulation with the source fixed at 10.6 cm distance to the module and aligned with respect to the module's centreline.
In order to determine, how different entry positions are weighted in this irradiation geometry, the relative FEP efficiency has been derived. This relative efficiency is defined as the ratio of the FEP efficiency at the given position divided by the maximum FEP efficiency, so that in the position, where the FEP efficiency reaches its maximum, a value of 100% is obtained. As can be seen in the last column of Figure 4.15, the fringes of the single module hardly contribute to the efficiency, the radius range from 5 mm to 22 mm contributes most.
From the first two columns of Figure 4.15 one can deduce that a reasonable assignment of the entry angle ϕ_{coarse} can be obtained for the following hit patterns: When only one segment is hit, the segment angle, which is defined as the centreline of the segment, is directly assigned to ϕ_{coarse} and when two neighbouring segments are hit the angle of the segmentation line between those two segments is a reasonable assignment. These events will be called *one-segment events* (OSE) and *neighbouring-two-segment events* (NSE) respectively. They are also the most important events, as more than 75% of all FEEs are OSEs or NSEs (see Figure 4.16). However it makes no sense to directly assign the angle of the segment with the highest energy deposition to ϕ_{coarse}, because it is not necessarily the entry segment. As can be seen in Figure 4.16, the initial γ-energy and the segment-hit-pattern determine, whether there is a high probability that the segment with the

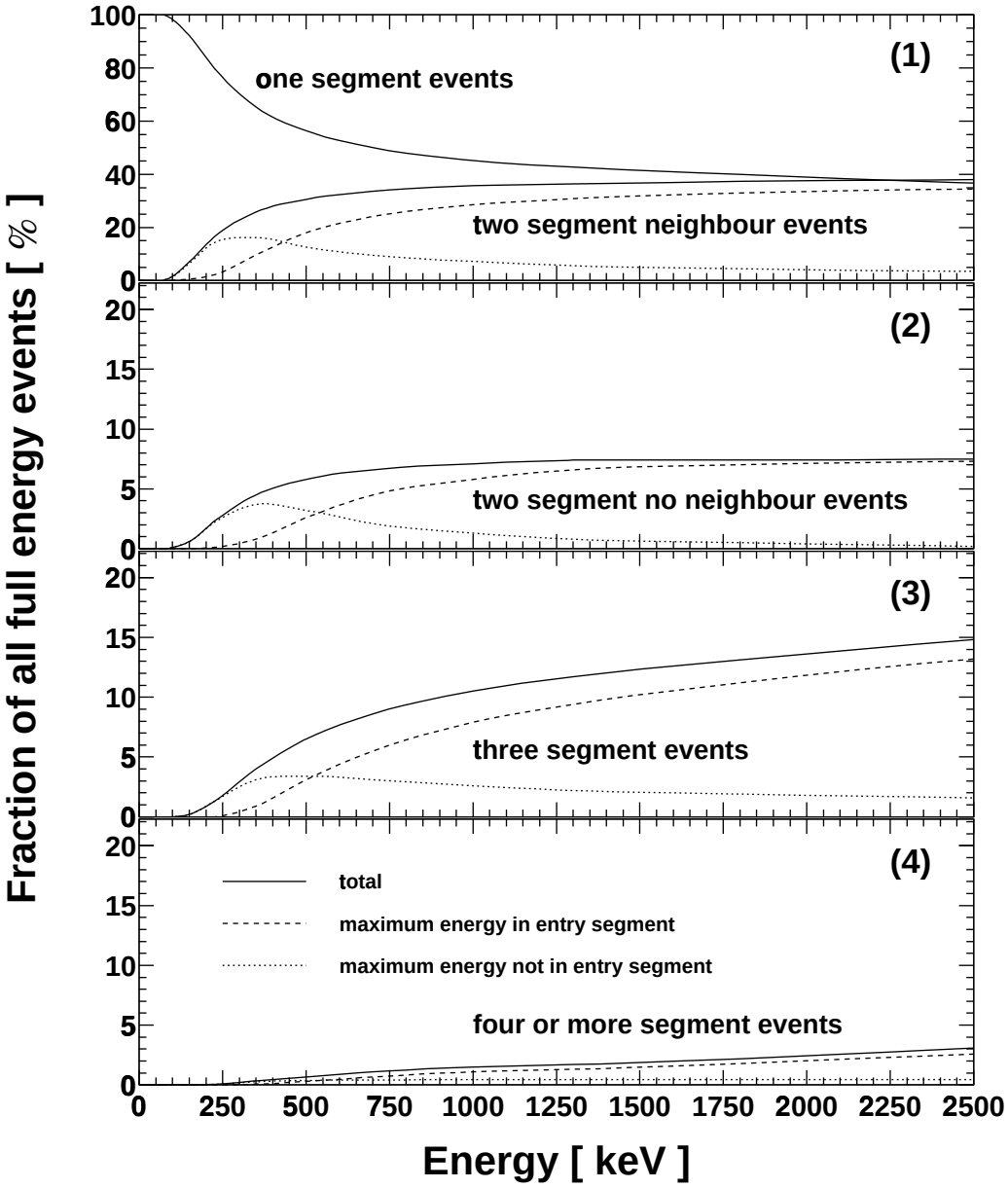

Figure 4.16: Energy-dependent segment multiplicity for a single MINIBALL module. The fraction of all FEEs, which are OSEs, NSEs, two-segment no-neighbour events, three-segment events, and four-segment events is shown as a function of energy. For a segment multiplicity above one, the fraction of FEEs, which have the maximum energy deposition in the entry segment and which do not have the maximum energy deposition in the entry segment is plotted, so that the limiting energy, at which the entry segment can be assigned to the segment with the maximum energy deposition can be deduced.

highest energy deposition is the entry segment or not.

It follows from the analysis of Figure 4.15 column 2 and Figure 4.16(1) that for NSEs it is safe to assign the segmentation line to ϕ_{coarse}, as long as E_γ is below 450 keV. For these energies most NSEs have their entry position in the segment with the lower energy deposition very close to the segmentation line. Above 450 keV the NSEs are more evenly distributed over the segment. Here the knowledge about the segment with the higher energy is an additional piece of information and can be used to achieve a better angular resolution. An energy weighted average of the two segment angles provides an improved ϕ_{coarse}-assignment.

Two-segment events, where the segments are not neighbours, are problematic as long as the γ-energy is below 600 keV. At these energies there is a higher probability that the segment with the smaller energy deposition is the entry segment (compare with Figure 4.16(2)). In this case one possibility is to assign the middle of the detector module ($R = 0$ cm) as the entry position – the entry segment is unknown; as an alternative, the segment with the lower energy can be assigned as the entry segment. The second alternative has the problem that the radius algorithm presented in section 4.2 will almost certainly fail, so that a fixed average radius has to be assigned. Furthermore the search for a low energy segment is error-prone, as a low energy can also be caused by crosstalk or another interference. It has therefore been decided to use a conservative approach and take $R = 0$ cm. At energies above 600 keV a majority of two-segment events, where the segments are not neighbours, have the highest energy deposition in the entry segment and the angle of the segment with the maximum energy deposition is assigned to ϕ_{coarse}.

Events where three or more segment are hit are treated similarly. Below a γ-energy of 600 keV the segment with the maximum energy deposition is usually not the entry segment (see Figure 4.16(3,4)) and the middle of the detector module ($R = 0$ cm) is assigned to the entry position. Above 600 keV the angle of the segment with the maximum energy deposition is assigned to ϕ_{coarse}, as the segment with the maximum energy deposition has a probability above 50% to be the entry segment.

The algorithm presented uses the segment multiplicity and the γ-ray energies ob-

Seg. Mult.	neighbours	energy	assigned angle	segment PSA
1	no	*	ϕ(MaxSeg)	Alg.1
2	1	<450keV	ϕ(Segline)	no
2	1	>450keV	weighted ϕ(Segline)	no
2	no	<600keV	Centre of Module	no
2	no	>600keV	ϕ(MaxSeg)	Alg.1
3+	*	<600keV	Centre of Module	no
3+	2	>600keV	ϕ(MaxSeg)	no
3+	1	>600keV	ϕ(MaxSeg)	Alg.2
3+	no	>600keV	ϕ(MaxSeg)	Alg.1

* means: does not depend on this value

Table 4.1: Multiplicity-dependent Angle Assignment for a single MINIBALL module. The segment multiplicity (Seg. Mult.) the number of neighbours of the entry segment and the the γ-energy determine, which angle to assign and which refinement algorithm to use.
"ϕ(MaxSeg)" means segment angle of the segment with the maximum energy deposition, "ϕ(Segline)" means angle of the segmentation line between two neighbouring segments, "weighted ϕ(Segline)" means energy weighted mean value of the two segment angles of two neighbouring segments, and "Centre of Module" means $R = 0$ cm – the entry segment is unknown.

served on the core and the hit segments to assign an angle ϕ_{coarse}, for a segment multiplicity above two also the "neighbour"-property is relevant. An overview of the algorithm can be found in Table 4.1, the segment PSA algorithms mentioned there will be described in the following section.
One of the most important features of this basic angle algorithm is the independence of the results of the radius algorithm. Thus the radius and angle algorithm are independent and it is impossible that a failure of the radius algorithm can cause a failure of the angle algorithm. Furthermore it is only necessary to compare the segment hit pattern and the segment energies, so that the computing time consumed is negligible and the analysis can even be done in real time.

The Angle Refinement Algorithms

The basic angle assignment algorithm does not employ all the information contained in the segment pulses to obtain the coarse angle ϕ_{coarse}; the shape of the

segment pulses is not yet used. One therefore tries to obtain a refined angle ϕ_{fine} from the basic angle ϕ_{coarse} by using segment-PSA. Two algorithms will be presented, they are however limited to certain segment hit patterns. Both algorithms have been simulated using the isotropic irradiation geometry with the source aligned with respect to the module's centreline. For the measurements the collimated perpendicular irradiation has been employed.

The most powerful segment-PSA algorithm is the $\log(\frac{|q_-|_{\max}}{|q_+|_{\max}})$ algorithm (Alg.1). It can be used, if ϕ_{coarse} unambiguously defines the entry segment and if both neighbours of the entry segment are not hit. As these conditions are fulfilled by all OSEs, this algorithm can be applied to at least 35% of all FEEs.

In this algorithm the charge pulse of the neighbour with the lower index[13] q_- is compared with the charge pulse of the neighbour with the higher index[14] q_+. The absolute charges temporarily accumulated on the neighbour segments are evaluated and $|q_-|_{\max}$ and $|q_+|_{\max}$, which are defined as the maximum values of the absolute charge pulses of the two neighbours of the entry segment (see also Figure 3.13 on page 45), are compared. As can be seen from the simulations presented in Figure 4.17, $\log(\frac{|q_-|_{\max}}{|q_+|_{\max}})$ exhibits a strong, almost-linear correlation with the angle within the segment, the correlation is different for different segments due to the anisotropy of the drift velocity of the electrons. The strength of the correlation depends on the actual *first interaction radius* and *not* on the entry radius, with the weakest correlation for first-interaction radii of about 1.5 cm and a stronger correlation for higher radii.

For all FEEs, where this algorithm could be applied, the angular resolution was simulated for a single MINIBALL module. The angular resolution was obtained in the same way as the radial resolution in section 4.2. For each segment a correlation plot was made, which included all FEEs, which had their first interactions in the selected segment. As the dependence of the angle on $\log(\frac{|q_-|_{\max}}{|q_+|_{\max}})$ was investigated $\log(\frac{|q_-|_{\max}}{|q_+|_{\max}})$ became the x- and the angle the y-coordinate. Linear fits on these plots yielded the correlation functions for each segment:

$$\phi_{\text{fine}}(q_-, q_+, \phi_{\text{coarse}}) = C_1(\phi_{\text{coarse}}) \cdot \log\left(\frac{|q_-|_{\max}}{|q_+|_{\max}}\right) + C_2(\phi_{\text{coarse}})$$

[13] For segment 1 the segment with the lower index is segment 6.
[14] For segment 6 the segment with the higher index is segment 1.

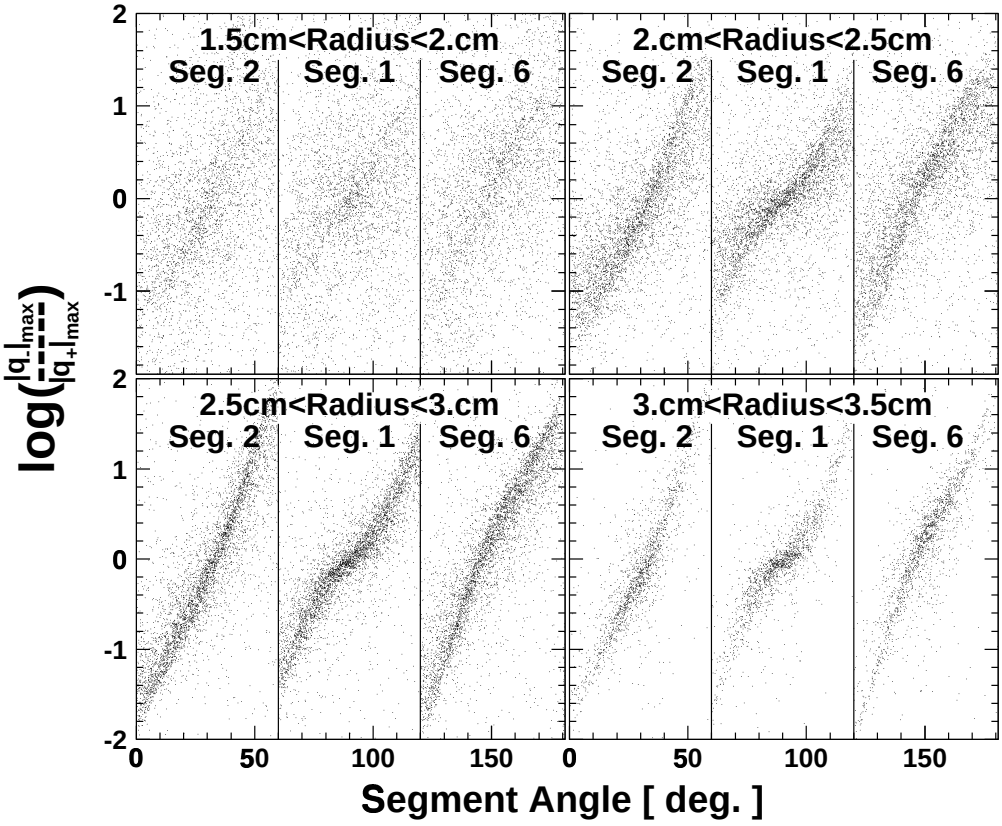

Figure 4.17: Simulated correlation of the $\log(\frac{|q_-|_{\max}}{|q_+|_{\max}})$ with ϕ at an energy of 700 keV. The isotropic irradiation geometry, where the source is positioned 10.6 cm away from the detector and aligned with respect to the module's centreline, has been used. For four different *first*-interaction radii ranges and three segments the correlation of $\log(\frac{|q_-|_{\max}}{|q_+|_{\max}})$ with the segment angle is shown. For each entry segment the charge pulses of the corresponding neighbours have been investigated (e.g. segment 1 and 6 for segment 2 as the entry segment). The angular resolution improves for larger radii. Due to the anisotropy of the drift velocity in dependence of the lattice direction, the correlations look different for different segments.

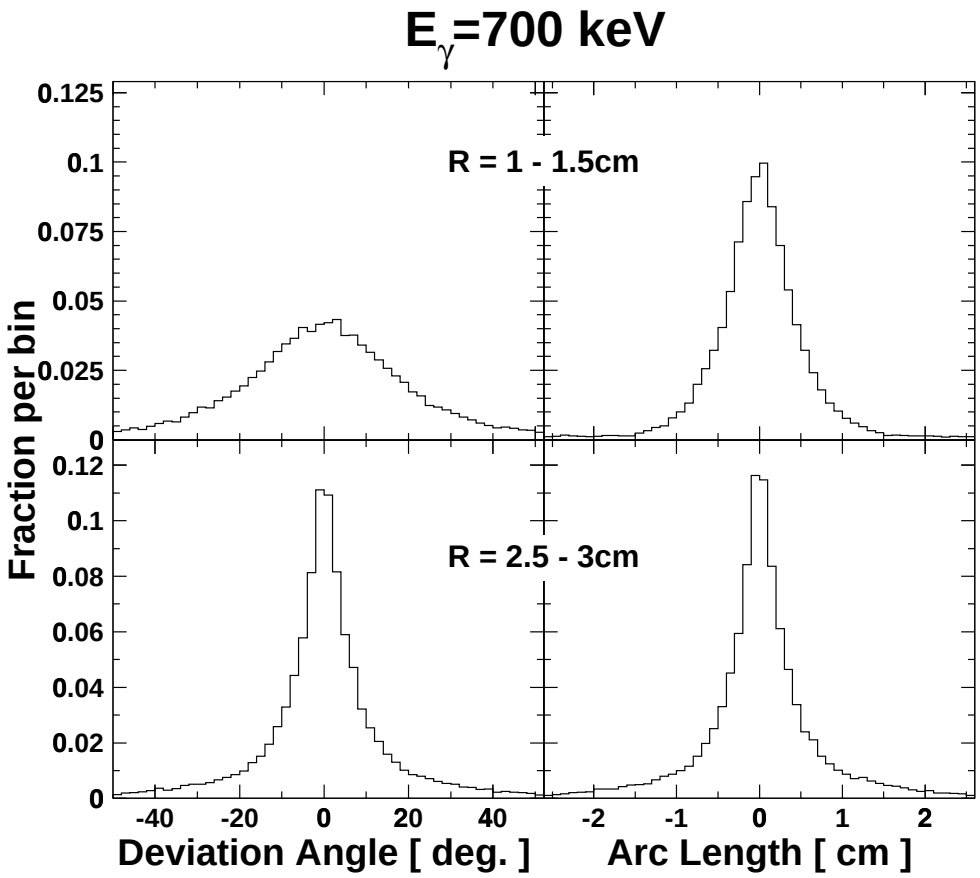

Figure 4.18: Simulated angular resolution and arc-length resolution of the $\log(\frac{|q_-|_{\max}}{|q_+|_{\max}})$-algorithm. In the first column the deviation of the correct angle from the angle provided by the algorithm is shown for first-interaction radii between 1 cm and 1.5 cm and for first-interaction radii between 2.5 cm and 3 cm. The arc-length deviation $R_1 \cdot \Delta\phi$ for the same first-interaction radius ranges is displayed in the second column.

Then the simulated pulses were analyzed a second time. The entry segment was determined by the the coarse angle algorithm. When the event had a suitable hit pattern, the refined angle was obtained using the correlation function of the determined entry segment. The difference between the correct entry angle and the angle obtained from the algorithm, the deviation angle $\Delta\phi$, was plotted in a one-dimensional histogram. A second histogram was filled with the arc length deviation $R_1 \cdot \Delta\phi$, where R_1 was the first interaction radius of the event. In order to demonstrate the first-interaction-radius dependence of the algorithm, the first interaction ranges between 1 cm and 1.5 cm and between 2.5 cm and 3 cm were selected.

The results of the simulation are plotted in Figure 4.18. The angular resolution is improving with increasing first interaction radius, while the arc-length resolution $R_1 \cdot \Delta\phi$, which determines the position resolution, remains almost constant for radii between 1.5 cm and 3.5 cm.

The simulations were compared with measurements, where the segment charge pulses were digitized using a 250 MHz 8-bit FlashADC-system [Wal92]. A collimator with a hot spot of 4 mm diameter was used to perpendicularly irradiate a single MINIBALL module, so that the γ-ray entry radius R_0 and angle ϕ_0 were equal to the first interaction radius R_1 and angle ϕ_1, respectively.

In Figure 4.19 the results of these measurements are presented for first interaction radii of 1.5 cm and of 2.85 cm and two series of angles within the segment. As expected, for a radius of 1.5 cm the angular resolution $\Delta\phi$ is only moderate, a measured value of 31° FWHM deduced from a Gaussian fit to the curve has been obtained, 15° have to be attributed to the finite size of the hot spot, so that an actual resolution of 25° FWHM is derived. At 2.85 cm an excellent angular resolution of 14° FWHM has been measured, here the collimator contributes only 8°, so that an actual resolution of 11° FWHM results. As a result of the improvement of the angular resolution with rising radius the arc-length resolution $R_1 \cdot \Delta\phi$ remains almost constant. The width of the measured distributions at an entry angle of 0° is comparable with that of the simulated distributions.

Although (Alg.1) is very powerful, it cannot be applied to events, where one neighbour of the entry segment is hit. Here the second algorithm (Alg.2) can be used that makes use of the correlation between the angle within the segment and

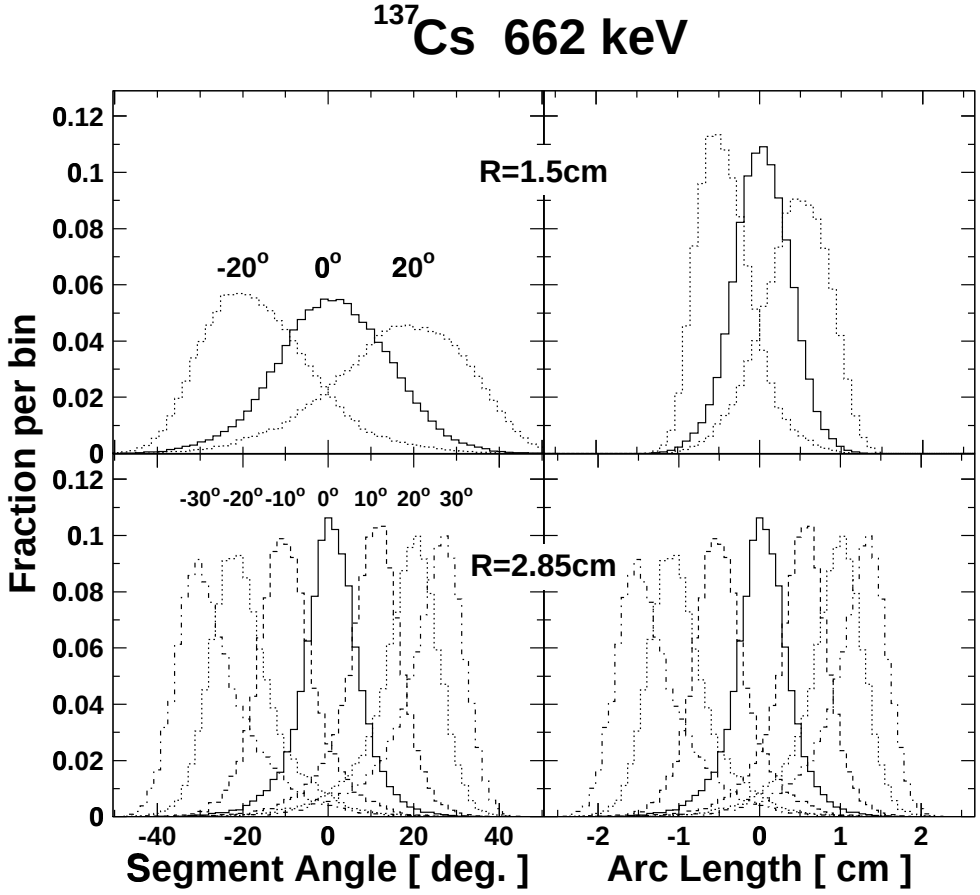

Figure 4.19: Measured angular resolution and arc-length resolution of the $\log(\frac{|q_-|_{\max}}{|q_+|_{\max}})$ algorithm. A single MINIBALL module has been irradiated perpendicularly using a collimated source. The hot spot of the collimator has a diameter of 4 mm. For a first-interaction radius of 1.5 cm the distributions for 3 collimator positions are shown, for a radius of 2.85 cm 7 positions are presented. The algorithm can only be used, when both neighbouring segments are not hit. For large radii above 2.5 cm an excellent angular resolution (first column) can be achieved, while the angular resolution at 1.5 cm is only moderate. Yet, the corresponding arc-length resolution (second column) at both radii is comparable.

the logarithm of the ratio of the maximum value of the absolute of the charge pulse of one neighbour and the charge deposited in the hit segment ($\log(\frac{|q_\pm|_{\max}}{q_{\text{seg}}})$) – see Figure 3.13 on page 45. As can be seen in Figure 4.20, the correlation is less pronounced than in Alg.1, so that only a moderate angular resolution can be expected. The angular resolution of the algorithm has been evaluated experimentally using the same irradiation geometry, which has been used to test the first algorithm (Alg.1). An angular resolution of 35° FWHM is obtained for a first-interaction radius of 2.85 cm, which is so much larger than the width caused by the collimator hot spot (8°) that the influence of the hot spot can be neglected. As the width of the angular distribution obtained is more than twice the size of the width obtained from the first algorithm, the second algorithm is only used, if the first algorithm is not applicable (one neighbour of the entry segment is hit). In Table 4.1 it is noticeable that Alg.2 is not used for NSEs with a γ-energy above 600 keV; the energy-weighted average of the segment angles is used instead. The angular resolution of the second algorithm together with the assignment of the entry segment to the segment with the higher energy deposition has been simulated[15] and compared with the direct assignment of the energy weighted average of the segment angles. The same angular resolution is obtained for both algorithms, so that the more simple algorithm has been selected. As Alg.2 is not used for NSEs, it only plays a minor role for angular refinement, it is used for less than 10% of all FEEs.

Two refinement algorithms have been presented, each of them can only be applied to FEEs with certain segment hit patterns. The powerful first algorithm can only be used, if both neighbours of the entry segment assigned from the basic angle algorithm are not hit, but an excellent angular resolution within the segment can be obtained. As it is applicable to OSEs more than 35% of all FEEs can be refined using this algorithm. The second algorithm only requires that one of the two neighbours of the entry segment is not hit. The missing information about the second neighbour results in a considerable broadening of the angular resolution. The poor angular refinement outweighs the greater applicability of

[15]For the simulation the same procedure was used, which was employed to simulate Alg.1. Correlation functions $\phi_{\text{fine}}(q_\pm, q_{\text{seg}}, \phi_{\text{coarse}}) = C_1(\phi_{\text{coarse}}) \cdot \log(\frac{|q_\pm|_{\max}}{(q_{\text{seg}})_{\max}}) + C_2(\phi_{\text{coarse}})$ were derived from the correlation plot and the simulated angle was determined using the correlation function.

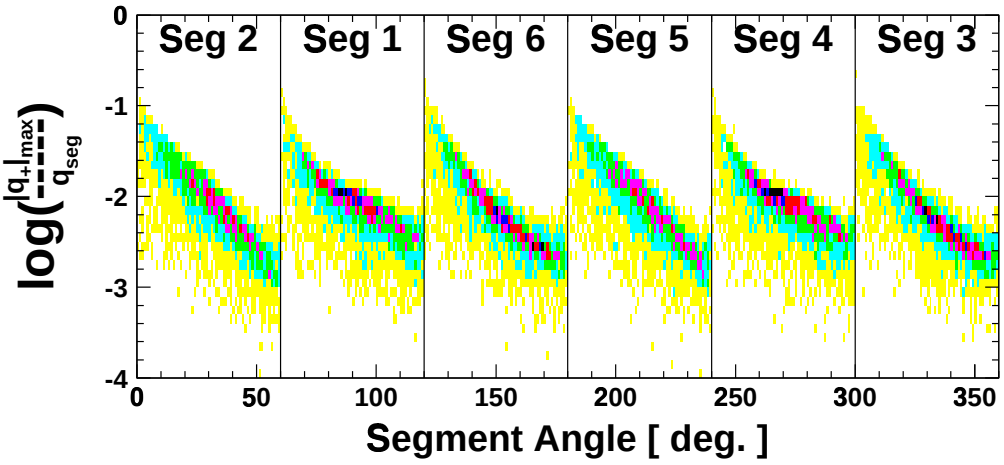

Figure 4.20: Angular correlation of $\log(\frac{|q_+|_{\max}}{q_{\text{seg}}})$ and ϕ at an energy of 700 keV. The correlation is very weak, so that the differences between the segments have almost disappeared.

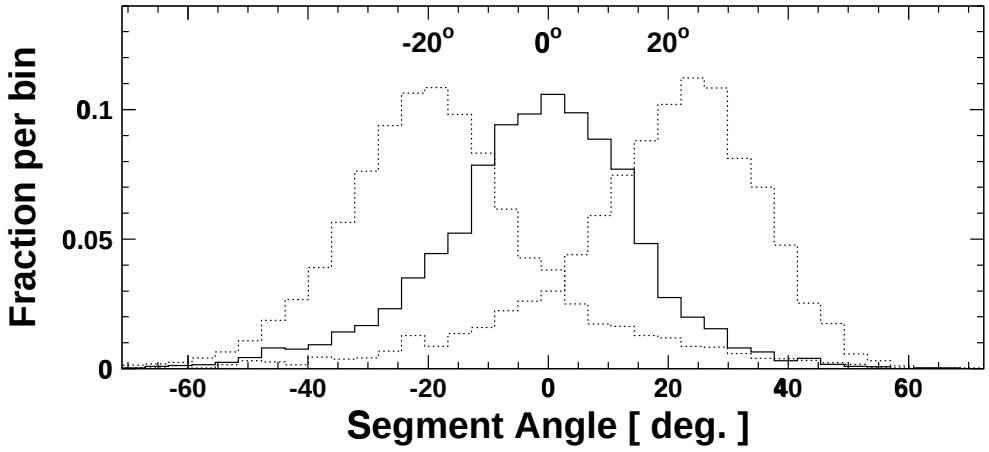

Figure 4.21: Measured angular resolution of the $\log(\frac{|q_+|_{\max}}{q_{\text{seg}}})$ algorithm. A ^{137}Cs source has been used and different positions with a radius of 2.85 cm have been irradiated. The measured resolution is about twice the width of the $\log(\frac{|q_-|_{\max}}{|q_+|_{\max}})$ algorithm.

the algorithm, so that it is only useful for less than 10% of all FEEs. Like the basic angle algorithm, which provides the coarse angle ϕ_{coarse}, the refinement algorithms do not depend on the radius information. Both refinement algorithms require the search for absolute maxima of the charge pulses in segments, which are not hit. This search requires about the same computing time as the calculation of an energy value for a hit segment. Hence it should be possible to operate both algorithms in real time.

4.3.2 The Aligned 3-Cluster

The angle algorithm for the single MINIBALL module now has to be extended, so that it is applicable for the aligned 3-Cluster, the cryostat type, which will mainly be used in MINIBALL experiments. Yet, for a target distance of 10.6 cm the modules of the aligned 3-Cluster do not aim at the target, so that it is no longer guaranteed that there is an energy deposition in the segment, where the γ-ray crosses the frontal plane of the module.

A thorough analysis of the segment response of the 3-Cluster and the development of an adapted angle algorithm became necessary. The segment response of the MINIBALL 3-Cluster was simulated on a grid of γ-ray entry points with a distance of 2 mm in both the x- and the y-direction, a linear interpolation was used to obtain points on a 1 mm grid. The source was positioned aligned with respect to the cryostat centreline, where all three modules touched. The distance from the source to the centre point of each module was 10.6 cm.

In Figure 4.22 the percentage of Cluster FEEs[16], for which the full energy is deposited in one segment (OSE) and the percentage, for which the full energy is deposited in neighbouring segments is shown for the given γ-ray entry positions and γ-energies of 356 keV, 662 keV, and 1333 keV. The relative efficiency is shown in the last column, so that the weighting of different entry positions is illustrated. The relative efficiency is defined as the ratio of the Cluster FEP efficiency[17] at the given position divided by the maximum Cluster FEP efficiency, so that in the position, where the Cluster FEP efficiency reaches its maximum, a value of

[16] In contrast to a module FEE, where the full γ-energy has to be deposited in one module, for a Cluster FEE it is only required that the energy is deposited in the three modules, so that inter-module scattering events are allowed.

[17] The Cluster FEP efficiency includes addback.

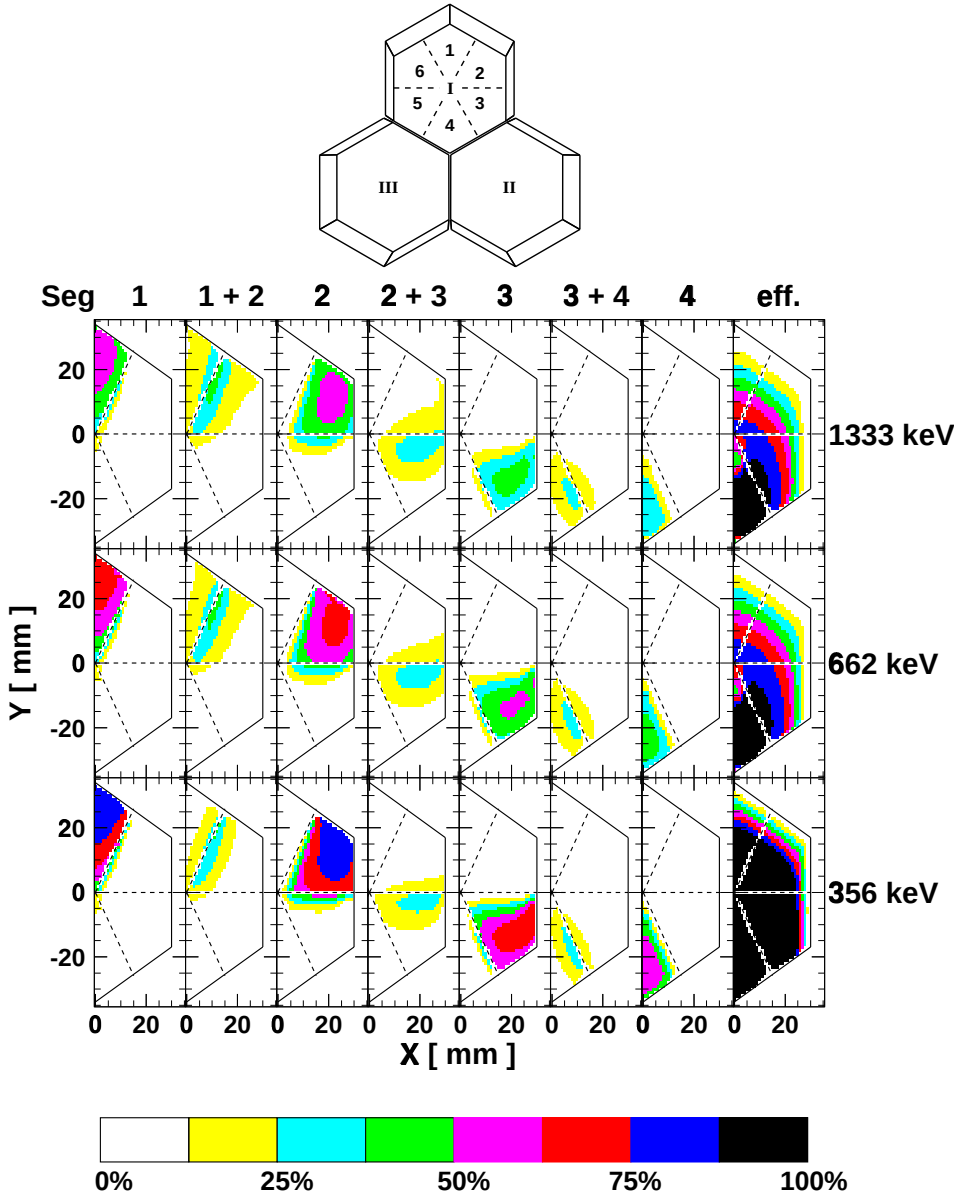

Figure 4.22: Position-dependent segment response for γ-ray entry positions on a 1 mm grid for the aligned 3-Cluster.
The entry positions of FEEs, for which all the energy is deposited in one segment and the fraction, for which the energy is deposited in two neighbouring segments is shown for energies at 356, 662, and 1333 keV. The grey scale reflects the fraction of all FEEs with this entry position, which deposit the energy in a OSE in the segment or which deposit the energy in a NSE in the two segments. In the last column the relative FEP efficiency is depicted; a definition of the relative FEP efficiency can be found in the text. The contour of the detector frontal plane and the physical segmentation lines (dashed) of the module are included in the plot.
It can be noticed that the entry point can be outside the segment, where the energy has been deposited.

100% is obtained.

For the irradiation geometry of the single module the source is aligned with respect to the module's centreline, so that the γ-ray entry point and the first interaction are always in the same segment. For the irradiation geometry of the aligned 3-Cluster, however, the γ-ray can penetrate through several segments. Hence the entry positions for OSEs in segment 1 of module I are no longer confined to segment 1, since the photon can pass through e.g. segment 2 without interacting and deposit all its energy in segment 1; segment 2 and segment 3 show a comparable behaviour. Only the OSEs in segment 4 have their entry position exclusively in segment 4, as no γ-ray, which enters a segment other than segment 4, can penetrate into this segment without scattering. A similar effect is observed for NSEs. The percentage of segment 1-2 NSEs has its maximum in segment 2 and not on the segmentation line, segment 2-3 and segment 3-4 NSEs have theirs in segment 3 and 4, respectively. This changed behaviour of the segment response of the modules in the 3-Cluster can be summarized in two effects: The first effect is smearing, i.e. there are γ-ray directions, where the possible first interaction positions are spread over at least two segments. As this spill-over only occurs in the vicinity of the borderline between two segments, it does not jeopardize a possible angular resolution. The second effect can be seen either as a displacement of the segmentation lines or as an asymmetric response of the segments. For the segments 2 and 3 the segment response for OSEs is asymmetric with respect to the centrelines of these segments, the segment response for NSEs is asymmetric with respect to the physical segmentation lines on the front plane of the module. The reason for the asymmetry can be explained, if one considers γ-rays, which enter the detector in segment 3 close to the segmentation line to segment 2. Although segment 3 is the entry segment, they almost immediately enter segment 2, if one follows the direction of γ-ray emission, so that there is a higher probability to have the first interaction in segment 2 than in segment 3.

The asymmetry of the segment response is not tolerable and the use of displaced segmentation lines should be avoided, because both would greatly enhance the complexity of an angle algorithm. There is, however, the possibility to circumvent this problem by varying the depth of the segmentation lines:

The physical segmentation lines on the detector frontal plane and on the side

plane of the detector define the segmentation planes inside the detector. These planes cut the detector in six pieces, so that an interaction occuring in one of these pieces can immediately be attributed to its corresponding segment. One now considers two directions of γ-emission: For γ-rays with an emission direction such that the segmentation plane is penetrated at the depth $z = 0$ cm, all first interactions occur behind the segmentation plane. The unwanted asymmetric segment response is obtained, when the detector frontal plane is used as the reference plane. For γ-rays with an emission direction such that the segmentation plane is penetrated at the depth $z{=}\langle z_1(E_\gamma)\rangle$, the energy dependent mean first interaction depth of the γ-ray, about the same number of first interactions happen in front and behind the segmentation plane. The segment response with respect to the segmentation lines at the depth $z{=}\langle z_1(E_\gamma)\rangle$ becomes symmetric[18]. Hence the γ-ray entry positions must not be used as they represent the depth $z = 0$ cm. One follows the direction of the γ-ray and calculates the point, where it intersects the plane $z{=}\langle z_1(E_\gamma)\rangle$ – for each γ-ray entry position a corresponding reference position in the $\langle z_1(E_\gamma)\rangle$-plane is obtained. In analogy to the entry segment, which is the segment where the γ-ray penetrates the z=0-plane, a segment is called the *reference segment*, if the initial direction of the γ-ray penetrates the $\langle z_1(E_\gamma)\rangle$-plane in this segment. The position-dependent segment response of the aligned 3-Cluster with respect to the reference plane $z{=}\langle z_1(E_\gamma)\rangle$ is shown in Figure 4.23. For each γ-ray entry point the corresponding point in the reference plane is plotted, the projection of the contour of the detector frontal plane on the reference plane with respect to the source position is depicted. In addition the lines are shown, where the segmentation planes cut the reference plane.
The change from the detector frontal plane to the reference depth $z{=}\langle z_1(E_\gamma)\rangle$ ensures a symmetric segment response, which is similar to the response of the single MINIBALL module. Hence it will be possible to use the concepts of the basic angle assignment developed for a single module also for the aligned 3-Cluster, where the modules are tilted and do not aim at the source. A complicated angle algorithm can be avoided. In contrast to the segmentation lines in a single mod-

[18]This is not true in the vicinity of the borders of a module that are not adjacent to a another module, however these regions do not influence the behaviour of the respective segments, as the relative FEP efficiency is too small, as can be seen in Figure 4.22.

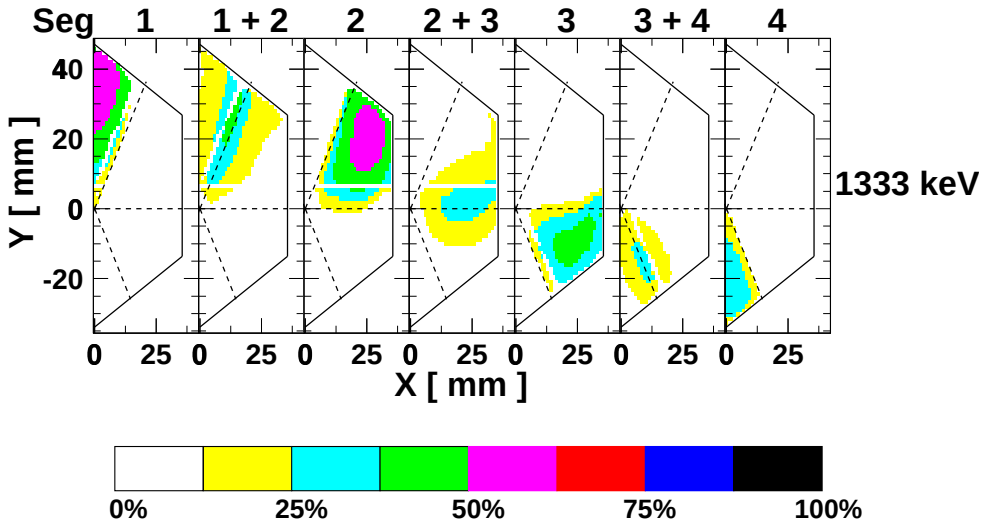

Figure 4.23: Position-dependent segment response of the aligned 3-Cluster with respect to the plane located at the mean first interaction depth (z=$\langle z_1(E_\gamma)\rangle$).
The reference positions of FEEs, for which all the energy is deposited in one segment and the fraction, for which the energy is deposited in two neighbouring segments is shown for a γ-energy of 1333 keV. The grey scale reflects the fraction of all FEEs with this reference position, which deposit the energy in a OSE in the segment or which deposit the energy in a NSE in the two segments. In addition the "segmentation" lines are shown, where the segmentation planes intersect the reference plane.

ule, the 3-Cluster "segmentation-lines" at the reference depth are not sharp, but smeared out a little bit. However, this penetration of the segment response into the neighbouring segments is very small.
The aligned 3-Cluster is not fully comparable with the single module, as some of the Cluster FEEs are inter-module-scattering events; in the aligned 3-Cluster up to one fifth of all FEEs are distributed over at least two modules (compare with the addback factor in Figure 4.2). As can be seen in Figure 4.24 these inter-module-scattering events are mainly located in segments which are adjacent to another module. This property is especially important, when it is impossible to assign a reference segment. In this case a position on the 3-Cluster, which does not only reflect the segment, but also the module multiplicity, has to be assigned.
As the differences between the single module and the aligned 3-Cluster have been depicted and the problems with the asymmetric segment response have been solved, the basic angle assignment algorithm for the aligned 3-Cluster can be presented.
It has been discussed that the modules in the aligned 3-Cluster exhibit a similar behaviour as in the single module. When the correct reference depth is used ($z{=}\langle z_1(E_\gamma)\rangle$), the segment response becomes comparable. However, in the 3-Cluster three modules are operated together allowing the scattering between the modules. Therefore the segment-assignment algorithm has to be adapted and new segment hit patterns have to be included. In particular it is important determine the energy limit for all the different hit patterns possible, where the reference segment can be assigned to the segment with the maximum energy deposition. As it was done for the single module, the energy limits can be extracted from the energy-dependent segment and module multiplicity of the aligned 3-Cluster, which is shown in Figure 4.25.
For events, which are confined to one module (left column) the basic angle assignment algorithm remains the same as for the single MINIBALL module.
For two-module NSEs (panel 2b) the middle of the segmentation line between the segments is selected, as long as the γ-energy is below 450 keV, above the segment with the higher energy deposition is selected as the reference segment. For two-module two-segment no-neighbour events (panel 3b), the two-module common point is selected, as long as the γ-energy is below 600 keV, above the segment

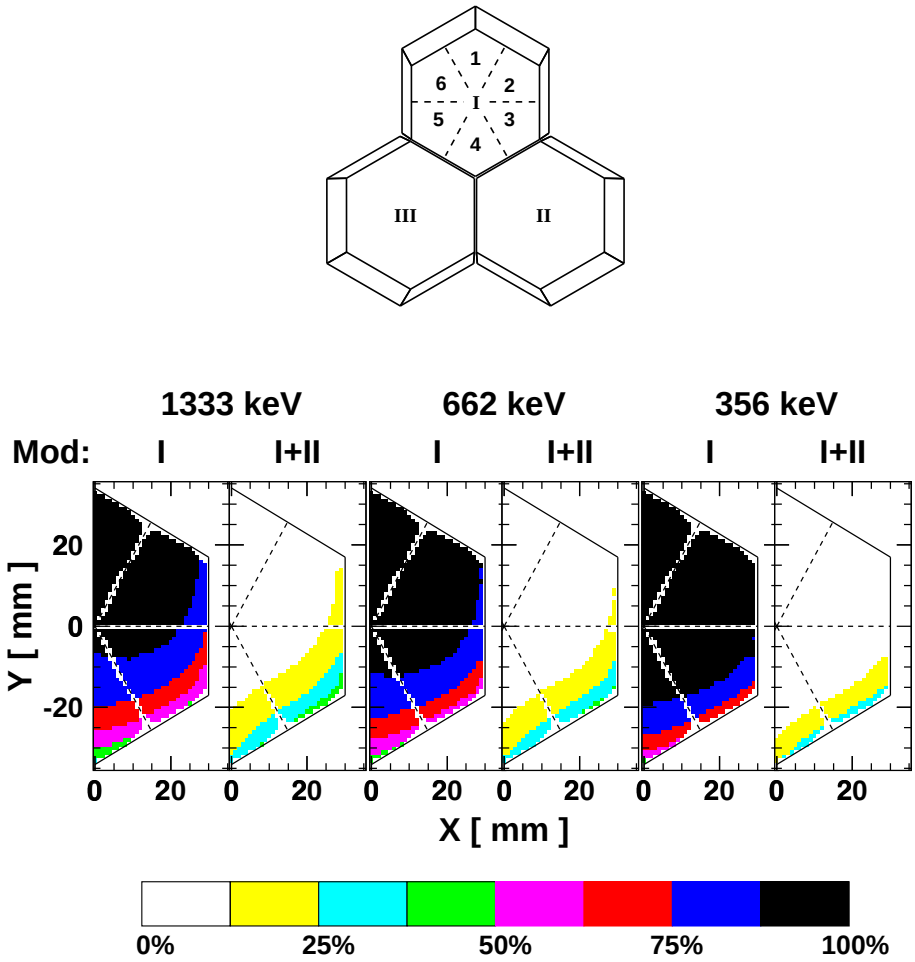

Figure 4.24: Position dependent module response for γ-ray entry positions on a 1 mm grid for the MINIBALL aligned 3-Cluster.
For different entry positions the fraction of FEEs, which is contained in one module, and the fraction, which scatters in the lower right neighbouring module is shown for energies at 356, 662, and 1333 keV.

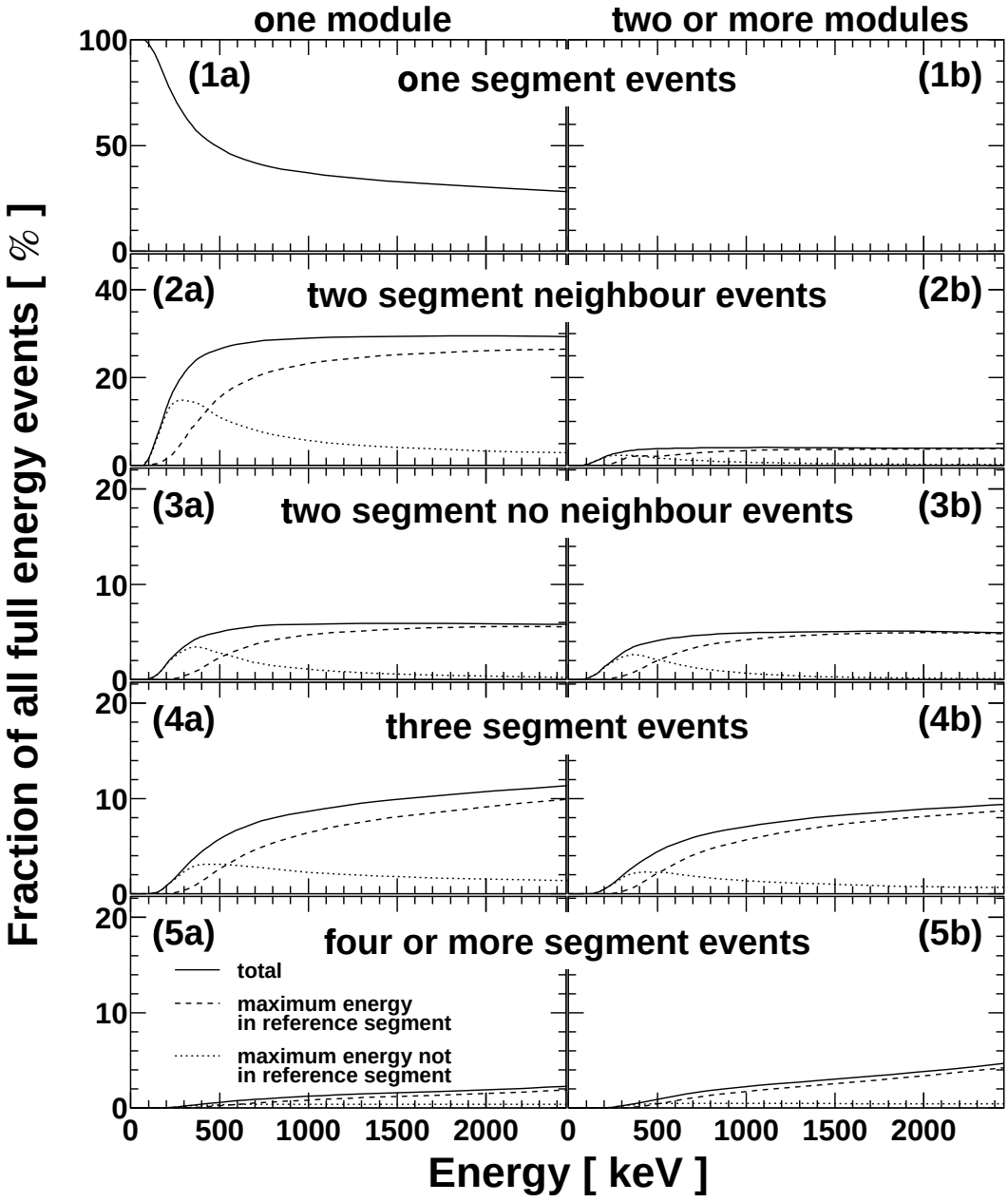

Figure 4.25: Energy-dependent segment and module multiplicity for the MINIBALL 3-Cluster. The energy-dependent fraction of all FEEs, which are OSEs, NSEs, two-segment no-neighbour events, three-segment events, and four-segment events is shown for a module multiplicity of one and above one. For each segment multiplicity above one, the fraction of FEEs, which have the maximum energy deposition in the reference segment and which do not have the maximum energy deposition in the reference segment is depicted separately, so that the limiting energy, at which the reference segment can be assigned to the segment with the maximum energy deposition, can be deduced.

with the higher energy deposition is selected as the reference segment. For three-and-more-segment events in at least two modules with a γ-energy above 600 keV (panels 4b and 5b), the segment with the maximum energy deposition is selected as the reference segment, below 600 keV the two-module common point is selected for two-module events and the three-module common point for three-module events, respectively.

A summary of the assigned segments and modules is listed in Table 4.2. Depending on the γ-energy, the segment multiplicity, the number of modules which have fired (module multiplicity), and the number of hit neighbours of the segment with the maximum energy deposition within the module and outside the module, respectively, either an angle or a certain position on the cryostat is assigned. Whenever possible an additional segment PSA algorithm to obtain an angular refinement is used. The PSA algorithms used for the aligned 3-Cluster are identical with the algorithms used for the single module, however, instead of the entry segment the reference segment is used. The basic angle algorithm together with the conditional refinement by segment PSA is called the full angle algorithm. It is important to note that all FEEs are processed by this full algorithm, so that no statistics is lost. Depending on the segment hit pattern the algorithm will provide good or only moderate angular information. As both the basic angle algorithm for the 3-Cluster and the angle refinement algorithms do not use the radius information, they are independent of the results of the radius algorithm. Therefore a failure of the radius algorithm does not affect the angle algorithm. The full angle algorithm only relies on basic pattern matching and the additional refinement algorithms, which use PSA, so that the computing time consumed is small enough for real-time processing.

4.3.3 Angular Resolution in MINIBALL Experiments

Angular and Arc-Length Resolution Predictions

The full angle algorithms consisting of angular assignment and angular refinement (see Tables 4.1,4.2) have been presented. They were applied to all FEEs except those where R=0 was assigned to obtain a simulated angular and arc-length resolution for a single MINIBALL module and the aligned MINIBALL

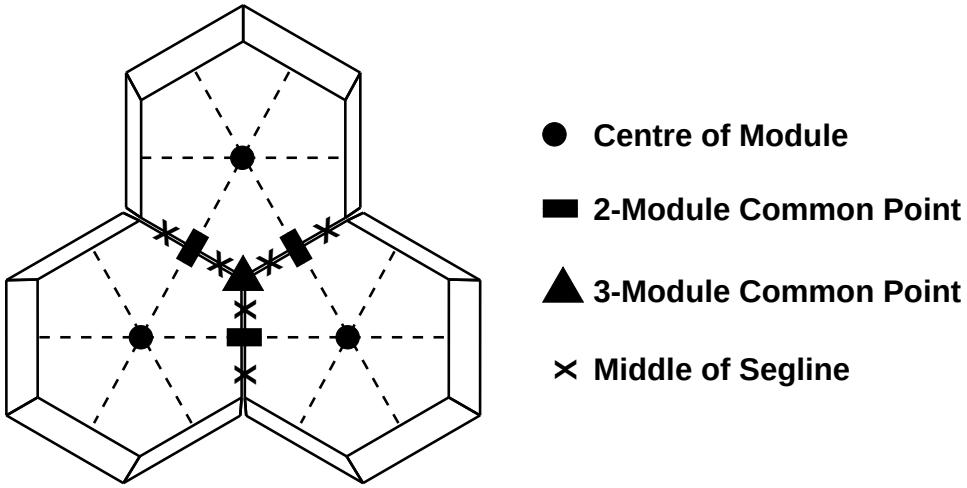

Multiplicity		neighbours		energy	assigned angle	segment PSA
Seg.	Module	Mod.	other			
1	1	no	no	*	ϕ(MaxSeg)	Alg.1
2	1	1	no	<450keV	ϕ(Segline)	-
2	2	no	1	<450keV	middle of Segline	-
2	1	1	no	>450keV	weighted ϕ(Segline)	-
2	2	no	1	>450keV	ϕ(MaxSeg)	Alg.1
2	1	no	no	<600keV	Centre of Module	-
2	2	no	no	<600keV	2-Mod. Common Point	-
2	*	no	no	>600keV	ϕ(MaxSeg)	Alg.1
3+	1	*	no	<600keV	Centre of Module	-
3+	2	*	*	<600keV	2-Mod. Common Point	-
3+	3	*	*	<600keV	3-Mod. Common Point	-
3+	*	2	*	>600keV	ϕ(MaxSeg)	-
3+	*	1	*	>600keV	ϕ(MaxSeg)	Alg.2
3+	*	no	*	>600keV	ϕ(MaxSeg)	Alg.1

* means: does not depend on this value

Table 4.2: Multiplicity-dependent angle algorithm for the aligned 3-Cluster. The segment and module multiplicity, the number of neighbours of the reference segment and the γ-energy determine, which angle to assign and which refinement algorithm to use.
ϕ(MaxSeg), ϕ(Segline), and weighted ϕ(Segline) are defined in Table 4.1 on page 76. The "2-Mod. Common Point", the "3-Mod. Common Point", the "Centre of Module" and the "Middle of Segline", which is the middle of the line two neighbouring segments in different modules share, are shown in the sketch above.

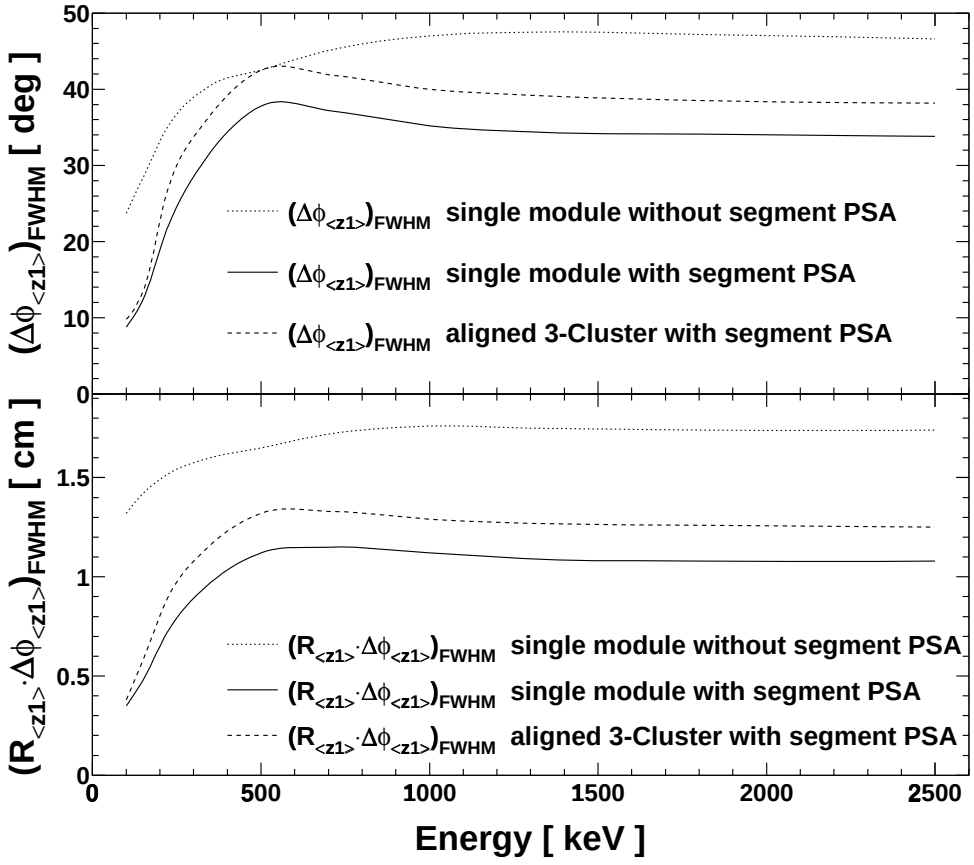

Figure 4.26: Angular resolution $\Delta\phi$ and Arc-Length Resolution $R_{\langle z_1\rangle}\cdot\Delta\phi$ of the full angle algorithm. Only FEEs are processed.

3-Cluster. For the simulations an irradiation geometry with a distance between source and module of 10.6 cm was used. For the single module, the source was aligned with respect to the module's centreline, for the 3-Cluster with respect to the common edge of all three modules (centreline of the 3-Cluster). The simulation gave prediction for the angular and arc-length resolution with respect to the reference depth $z_{\mathrm{ref}}=\langle z_1(E_\gamma)\rangle$. The resolution was obtained by fitting a Gaussian curve to the angular and arc-length deviation plots and taking the FWHM of the Gaussian fit.

As can be seen in Figure 4.26 both the angular resolution and the arc-length resolution show a sharp rise between 100 keV and 500 keV from 10° to ∼40° and from 0.4 cm to ∼1.2 cm, respectively. If the angular refinement by segment PSA

is used, they have a maximum at about 500 keV with angular resolution values of 36° and 42° and with arc-length resolution values of 1.1 cm and 1.3 cm for the single module and the aligned 3-Cluster, respectively. Then a decrease to an almost constant level slightly below the maximum value is observed. Without the segment PSA the magnitudes of these resolutions continue to grow and approach a limit, which is much higher (∼50°, 1.8 cm). The resolution improves by 30% and 40% for the angle and arc-length, respectively, if segment PSA is employed. It has been shown that a reasonable (compare with Figure 4.6) angular and arc-length resolution is obtained from the full angle algorithms for the single module and the aligned 3-Cluster. These algorithms consist of two parts, the basic angle assignment and, if applicable, the angular refinement. The assignment algorithm only relies on the segment hit pattern, whereas the refinement is obtained from segment PSA. While the basic assignment is directly obtained from the analysis of the hit pattern, correlation functions $\phi_{\mathrm{fine}}(q_-, q_+, \phi_{\mathrm{coarse}})$ and $\phi_{\mathrm{fine}}(q_\pm, q_{\mathrm{seg}}, \phi_{\mathrm{coarse}})$ are needed for the first and the second refinement algorithm, respectively. In order to use these algorithms in experiment, one now has to discuss how the results obtained in the simulations can be transferred to experiments.

Application of the Algorithms in Experiments

Since the reliability of the GEANT simulations is considerably better than the reliability of the pulse simulations (e.g. no assumption about an "average detector"), the basic angle assignment algorithm can be transferred to experiment as it is, no adjustments are needed. Unfortunately, this is not true for the refinement algorithms. The correlation functions obtained from simulation are not good enough and the same procedure needed to generate the correlation function for the steepest-slope algorithm has to be applied (see page 70). In a calibration beam-time γ-singles with the correct hit patterns have to be recorded (γ-energy, T_{slope}, segment energies, $|q_\pm|$ and q_{seg} or $|q_+|$ and $|q_-|$) for an offline-evaluation. The parameters of the correlation function have to be deduced from an optimization of the energy resolution after Doppler correction. While the basic angle assignment algorithm has been successfully applied to the data of the experiment described in chapter 5, the angular refinement has not yet been tested in an in-beam experiment, as the electronics available at that time has not been able to

record the segment pulses.

4.4 Expected Energy Resolution for MINIBALL Experiments

4.4.1 Estimated Energy Resolution

The energy-dependent radial and arc-length resolutions have been compiled, and can be used to predict the energy resolution after Doppler correction. However the radial and arc-length resolution values obtained in sections 4.2, 4.3 have been determined with respect to the reference depth $z_{\mathrm{ref}}=\langle z_1(E_\gamma)\rangle$, while the predictions for the energy resolution after Doppler correction given in section 4.1.4 on page 53 are determined with respect to the detector frontal plane z=0. Therefore the radial resolution $\Delta R_{\langle z_1\rangle}$ and arc-length resolution $R_{\langle z_1\rangle}\cdot\Delta\phi_{\langle z_1\rangle}$ have been scaled to obtain approximate values for ΔR_0 and $R_0\cdot\Delta\phi_0$:

$$\Delta R_0 \approx \Delta R_{\langle z_1\rangle}\times\frac{d}{d+\langle z_1(E_\gamma)\rangle} \quad \text{and}$$

$$(R_0\cdot\Delta\phi_0)\approx(R_{\langle z_1\rangle}\cdot\Delta\phi_{\langle z_1\rangle})\times\frac{d}{d+\langle z_1(E_\gamma)\rangle},$$

where $d=10.6$ cm is the distance between the target and the centre of the frontal plane of the detector modules. The scaled energy-dependent arc-length and radial resolutions are shown in the upper and in the middle panel of Figure 4.27. Furthermore the estimated relative energy resolution after Doppler correction for a γ-emitting nucleus travelling in beam direction with β=0.065 and the germanium detector positioned at an angle ϑ_{det}=90° is depicted in the lower panel. The energy resolution has been deduced using Figure 4.6 on page 55. The small difference between E_γ and $E_{\gamma-\mathrm{lab}}$ for a detector at $\theta_\gamma\approx 90°$ has been neglected. As can be seen in Figure 4.27-middle panel, the radial resolution has a peak at about 350 keV; at these energies the width of the radial resolution is larger than the width of the arc-length resolution (see upper panel). While the radial resolution improves significantly at higher energies, the arc-length resolution reaches a maximum at 500 keV and only slightly retreats to an almost constant value of about 1 cm. Comparing these results with Figure 4.6, it follows that the energy resolution is limited by the radial resolution only for energies below 350 keV,

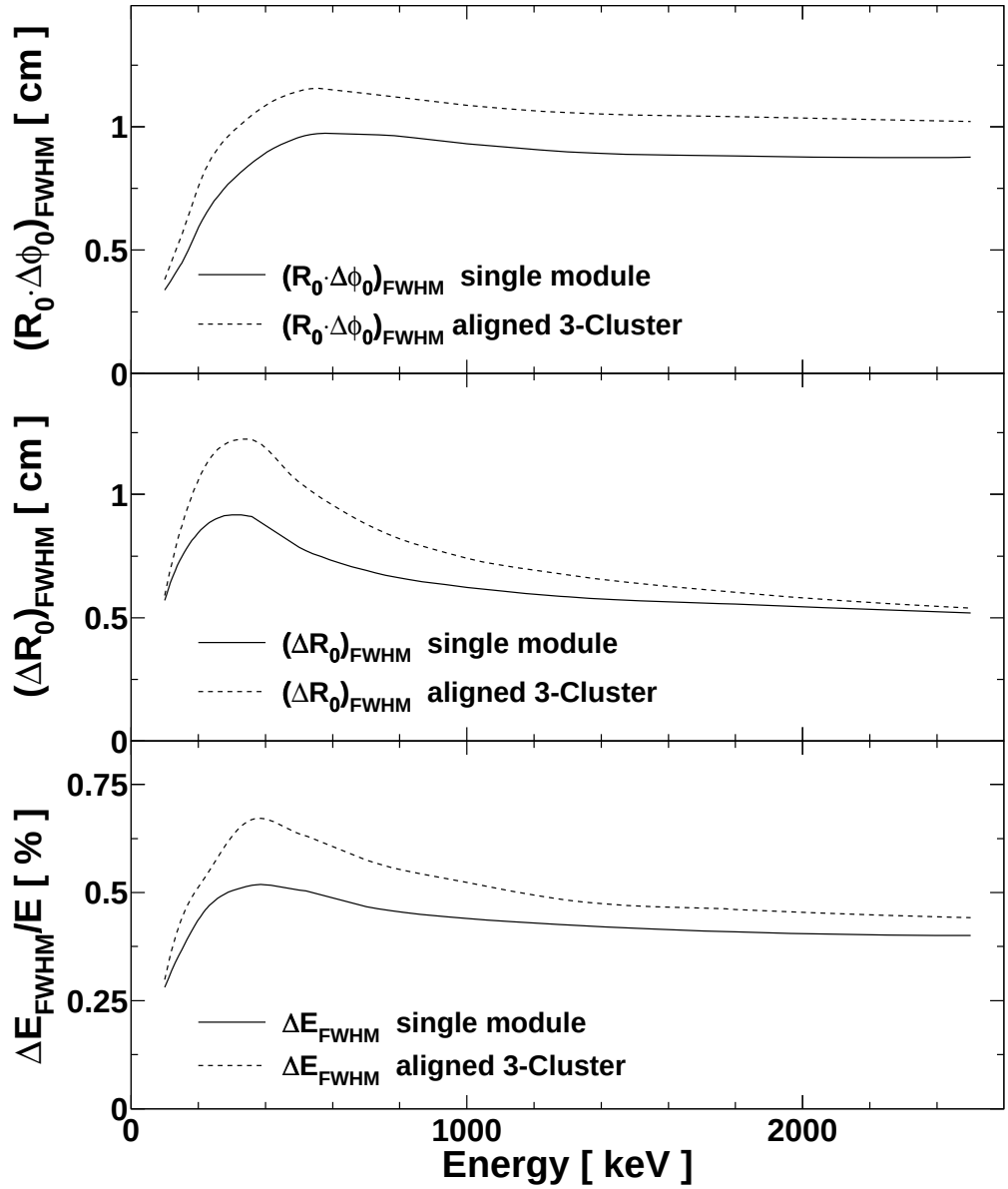

Figure 4.27: Simulated position resolution and resulting relative energy resolution after Doppler correction for the single MINIBALL module and the MINIBALL 3-Cluster. In the upper panel the arc-length resolution $R_0 \cdot \Delta\phi_0$ is shown, in the middle panel the radial resolution ΔR_0 is depicted. The resulting energy resolution after Doppler correction for a γ-emitting nucleus travelling in beam direction with β=0.065 and the germanium detector positioned at an angle ϑ_{det}=90° is shown in the lower panel. The typical irradiation geometries for the single module and the 3-Cluster are used (target distance of 10.6 cm, target aligned with respect to the module centreline and the cryostat centreline, respectively). $R_0 \cdot \Delta\phi_0$ and ΔR_0 are obtained by scaling from Figure 4.26 and Figure 4.14. The energy resolution is calculated using Figure 4.6.

at energies above 500 keV the arc-length resolution will limit the energy resolution. Only a moderate energy resolution has to be expected for energies between 300 keV and 600 keV where the FWHM widths of both the radial and the arc-length resolutions are close to their maximum.

4.4.2 Simulated Energy Resolution

The determination of the radial and arc-length resolution is not necessary to obtain an energy resolution. It is also possible to directly simulate the energy resolution by individually processing each FEE. The radius and the angle are obtained from the respective algorithms, for the z-coordinate the mean interaction depth $\langle z_1(E_{\gamma-\mathrm{lab}})\rangle$ of the γ-energy in the laboratory system is used. The energy values obtained from the Doppler correction using these coordinates are filled in a histogram for comparison with the correct γ-energy.
For the simulations a flight direction along the beam axis with β=0.065 has been assumed for the γ-emitting nucleus and the typical irradiation geometry of the detector system has been used (single module/3-Cluster). The histograms obtained from the simulations (solid lines) are shown in Figure 4.28 for three different γ-energies and a detector angle ϑ_{det}=90°. For comparison the simulated spectra obtained when an unsegmented (EUROBALL) module is used and the first interaction is assumed to occur at the point (R=0, ϕ=0, z=$\langle z_1(E_{\gamma-\mathrm{lab}})\rangle$) are added in the plot (dashed lines). The segmentation and pulse shape analysis used in MINIBALL provides a reduction of the line width by a factor of about three. Before the relative energy resolution as a function of the γ-energy is presented, it has to discussed in detail, how the energy resolution has been determined and how it describes the actual line shape obtained after Doppler-correction. As can be seen in the spectra for 700 keV in Figure 4.28, the Doppler-corrected γ-peaks do not have a Gaussian shape. The line has a sharper peak and larger tails than a Gaussian distribution. The Gaussian fit is nevertheless considered to give a good description of the energy resolution, as the actual FWHM of the peak is about 25% smaller than the one of the Gaussian peak, but the standard deviation σ of the energy distribution has about the same size as the FWHM of the energy distribution due to the extended tails. The simulated relative energy resolution obtained from the FWHM of the Gaussian fit is shown in Figure 4.29 for two dif-

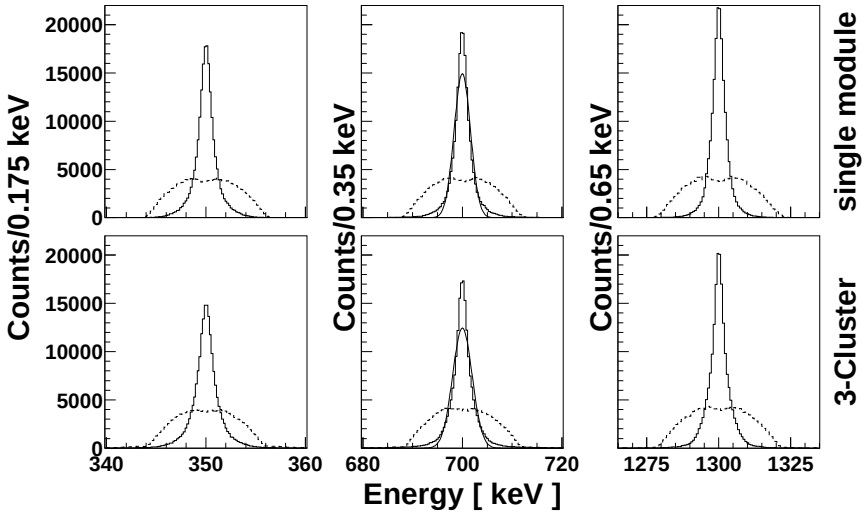

Figure 4.28: Simulated Doppler-corrected γ-lines for three different γ-energies. The γ-emitting nucleus travels in parallel to the beam with a velocity of β=0.065 and the detector is positioned at 10.6 cm target distance at an angle ϑ_{det}=90°. With the MINIBALL modules a good Doppler correction can be achieved (solid lines), whereas only very broad peaks are obtained, when an unsegmented (EUROBALL) module is used (dashed lines). As can be seen in the spectra for 700 keV the MINIBALL line-shape has a sharper peak and larger tails than a Gaussian distribution.

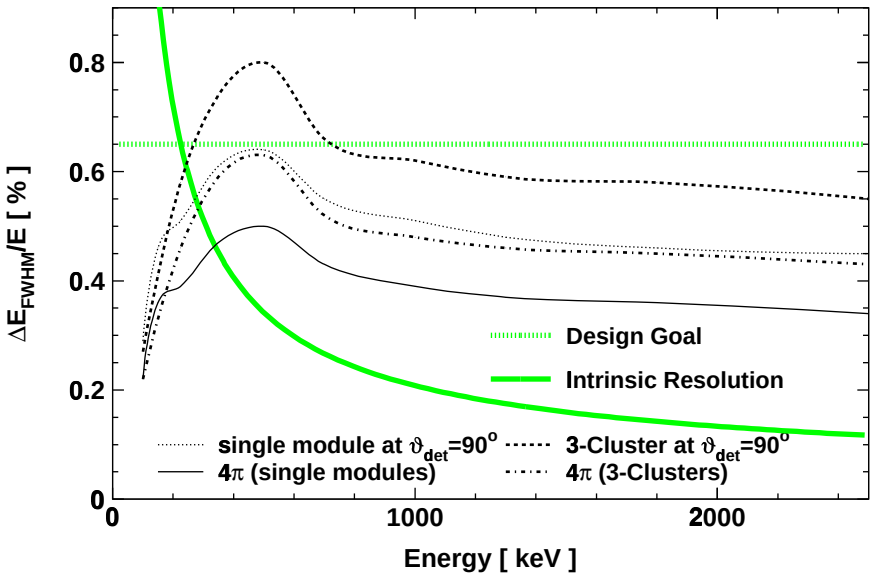

Figure 4.29: Simulated Energy Resolution of single MINIBALL modules and MINIBALL 3-Clusters for β=0.065. The reaction products are assumed to be travelling in beam direction. The expected relative resolution for an experimental setup with the detectors placed at ϑ_{det}=90° (θ_{γ}=90°) and for a setup with a 4π array arrangement of the detectors is shown. For comparison the intrinsic resolution and the design goal for the energy resolution after Doppler correction are included in the plot.

ferent detector setups for a single MINIBALL module and the aligned 3-Cluster. In one setup it is assumed that the detectors are only placed at ϑ_{det}=90° and that the beam particles are hardly scattered in the reaction, so that ϑ_{det}=θ_{γ}=90° holds. This is the most problematic setup for Doppler correction. In the other setup a full 4π array and an isotropic irradiation is assumed. The design goal of a relative energy resolution of $0.1\times\beta$ is achieved by 3 setups. The only setup that does not reach this goal for all γ-energies is an array of aligned 3-Clusters at ϑ_{det}=90°, where the relative energy resolution exceeds the limit for γ-energies between 200 keV and 700 keV by up to 20%.

A comparison of the predicted energy resolution (Figure 4.27) with the simulated values for the setup with ϑ_{det}=90° reveals that the prediction underestimates the actual energy resolution, which can be achieved. This behaviour is probably caused by the calculation of the arc-length deviation, because events, which are assigned to the centre of the module do by definition not have an angular deviation and, because a Gaussian curve does not describe the tails of the $R_{\langle z_1\rangle}\cdot\Delta\phi_{\langle z_1\rangle}$ distribution very well, which has the same sharp peak and the same extended tails as the $R_1\cdot\Delta\phi$ distribution (compare with Figure 4.18).

The independent radius and angle algorithms, which have been presented, permit a sufficient angular and radial resolution. They are kept as simple as possible, so that they need little processing time and can be implemented on either the FPGA or the DSP of the XIA-module. An implementation on the DSP is in progress now in order to have the algorithms available for online-processing. In a further step it is recommended to implement them on the FPGA, so that the valuable processing time of the DSP can be used for other tasks.

Chapter 5

The REX-ISOLDE Test Experiment

One of the main applications for MINIBALL will be the REX-ISOLDE project at CERN[Hab94]. Here the radioactive isotopes produced and accelerated in the ISOLDE facility will be accumulated and postaccelerated to an energy of up to 2.2 MeV·A to permit γ-ray spectroscopy following Coulomb excitation and transfer reactions in inverse kinematics on light target materials. The aim is the investigation of the collective and single-particle structure of low-lying levels of nuclei with extreme N/Z-ratios.

As low beam intensities are expected for the most exotic nuclei close to the dripline and the reaction products move with high velocities ($\beta \sim 0.07$), it was decided to perform an experiment at the MPI-K tandem facility in Heidelberg to investigate the problems related to γ-spectroscopy under these conditions and possible solutions for them. Transfer reactions, similar to the ones which will be performed at REX-ISOLDE, were selected for the experiment, since absolute cross sections for neutron transfer reactions had already been calculated by Lenske and Schrieder[Len98a]. In the experiment a ^{36}S beam with an energy of 2.2 MeV·A was used as projectile, while deuterium enriched polythene and ^{9}Be were used as target materials. Mainly the neutron-pickup to ^{37}S was investigated and compared with other reaction channels.

The main aim of the experiment was to determine the in-beam energy resolution after Doppler correction for the MINIBALL modules. In particular the energy resolution for transfer reactions, where the flight direction of the γ-emitting nu-

cleus was not measured, were investigated. The second aim was to examine, how the few reaction γ-rays of low-intensity experiments could be separated from the intense background. For this purpose the REX-ISOLDE Parallel Plate Avalanche Counter[Cub99] (PPAC) was included in the experimental setup permitting a coincidence measurement. Furthermore it was aimed to study the single-particle properties of ^{37}S, and the high transfer cross sections predicted for single neutron transfer at REX-ISOLDE beam energies [Len98b] had to be proven.

5.1 Reaction Kinematics and Differential Cross Sections

As the low neutron binding energy hinders the neutron transfer to an already neutron rich nucleus and as neutrons themselves are not available as target material, the very few stable nuclei which have a weakly bound neutron should be used for the target for neutron transfer experiments.
Two light target materials were available, which permitted neutron-transfer reactions at REX-ISOLDE energies, deuterium and beryllium. For these two target materials possible reaction channels, the reaction kinematics and the predicted differential cross sections had to be studied, so that the experimental setup could be adapted to the requirements of the experiment.
The deuteron consists of a proton and a neutron bound with an energy of 2.2 MeV. Besides the neutron pickup ^{2}H(^{36}S,^{37}S)p, the proton pickup channel ^{2}H(^{36}S,^{37}Cl)n exists, which has the same reaction kinematics. Furthermore other reaction channels are possible, but can hardly be observed. The fusion evaporation reaction ^{2}H(^{36}S,^{37}Cl n) yields the same nucleus as the proton transfer channel. The single nucleon stripping reactions ^{2}H(^{36}S,^{35}S)^{3}H and ^{2}H(^{36}S,^{35}P)^{3}He are energetically suppressed and the ^{2}H(^{36}S,^{34}P)^{4}He reaction is unlikely, as two nucleons have to be transferred.
With a neutron separation energy of 1.67 MeV and a proton separation energy of 16.9 MeV ^{9}Be could also be considered to be a perfect neutron target. In contrast to deuterium, where the proton and neutron pickup channels cannot be distinguished unless the proton is detected or the level scheme of one of the two transfer products is already known, the proton pickup is strongly suppressed for

the beryllium target. Yet there exist several reaction channels, where more than one nucleon is transferred from ^{9}Be to the projectile nucleus (see section 5.5 and Figure 5.16).

The reaction kinematics of both target nuclei are shown in Figure 5.1 for the population of the $3/2^-_1$-level at 646 keV and the $1/2^-$-level at 2.64 MeV.

It shows that in the ^{2}H(^{36}S,^{37}S)p reaction the ^{37}S-nucleus is deflected by less than 2.5° degrees and travels at about beam velocity regardless of the deflection angle. In contrast, the kinematics of the reaction with the beryllium target show a significantly larger deflection of up to 14° and a considerable energy loss at large c.m. scattering angles. Hence one can expect to achieve a sufficient Doppler correction when using a deuterium target even without detecting one of the scattered reaction products, while at least a partial kinematic reconstruction is necessary to calculate the Doppler shift when a Beryllium target is used.

In order to determine differential cross sections $\left(\frac{\mathrm{d}\sigma}{\mathrm{d}\Omega}\right)_{\mathrm{cm}}$ one option is to trace one of the reaction products (the other option is line-shape analysis of the spectra of γ-ray detectors in forward and backward direction). For the deuterium target the small energy and scattering angle variations of the heavy reaction product do not allow a determination of differential cross sections, in contrast it is possible to obtain differential cross sections by measuring both the scattering angle and the energy of the heavy reaction product when the beryllium target is used. Furthermore it is possible to deduce differential cross sections by detecting the light reaction product. Here the determination of the scattering angle ϑ_{lab} is sufficient, as for both target materials and both excited states an unambiguous ϑ_{cm} can be deduced, but the energy of the particles emitted in backward direction is so small that they can hardly be detected. From conservation of energy and momentum one derives that for

$$Q > E_{\mathrm{beam}} \cdot \left(\frac{M_{\mathrm{p}}}{M_{\mathrm{pt}}} - 1\right) \tag{5.1}$$

the light particle can be emitted in backward direction, where E_{beam} is the energy of the beam particles and $M_{\mathrm{p}}/M_{\mathrm{pt}}$ is the ratio of the projectile masses before and after transfer. For the ^{2}H(^{36}S,^{37}S)p-reaction, this condition is fulfilled for excited states up to an energy of 4.23 MeV, as the reaction has a Q-value of 2.08 MeV for the population of the ground state. For the ^{9}Be(^{36}S,^{37}S)^{8}Be reaction the condition is fulfilled for states up to 4.79 MeV, as a Q-value of 2.64 MeV for the population

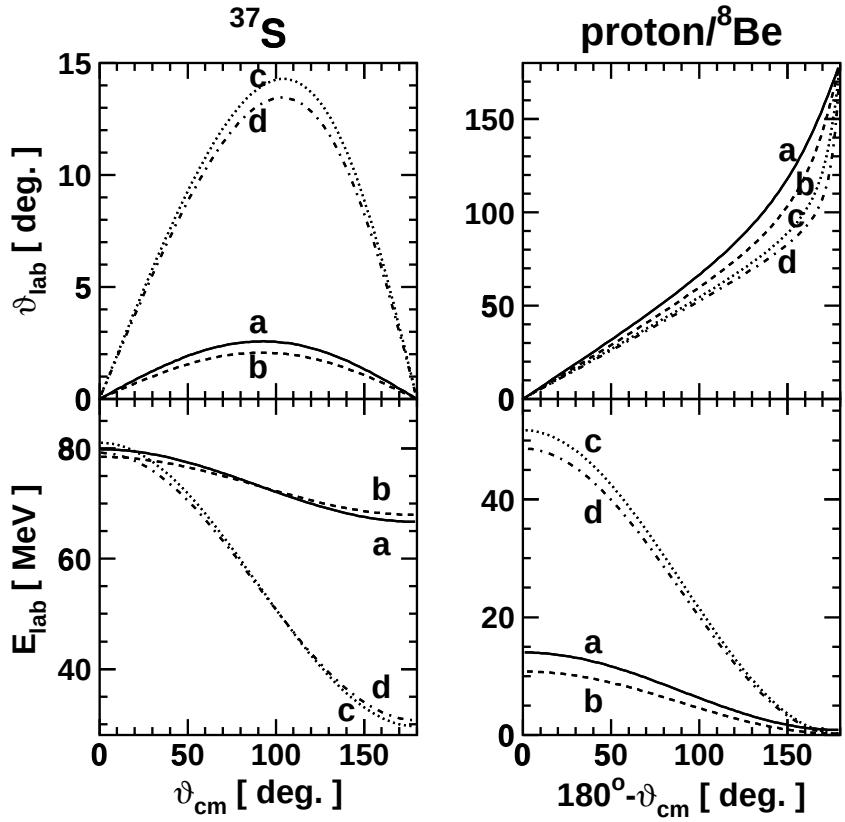

Figure 5.1: Kinematics of the ^{2}H(^{36}S,^{37}S)p and ^{9}Be(^{36}S,^{37}S)^{8}Be reaction populating the ^{37}S $(3/2)^{-}$ level at 646 keV and the $(1/2)^{-}$ level at 2.64 MeV. All angles are measured with respect to the beam axis, with ϑ_{cm} denoting the scattering angle of ^{37}S in the c.m. system, and ϑ_{lab} standing for the laboratory angles of the reaction products.

a) ^{2}H(^{36}S,^{37}S($3/2^{-}$ 646 keV))p
b) ^{2}H(^{36}S,^{37}S($1/2^{-}$ 2.64 MeV))p
c) ^{9}Be(^{36}S,^{37}S($3/2^{-}$ 646 keV))^{8}Be
d) ^{9}Be(^{36}S,^{37}S($1/2^{-}$ 2.64 MeV))^{8}Be

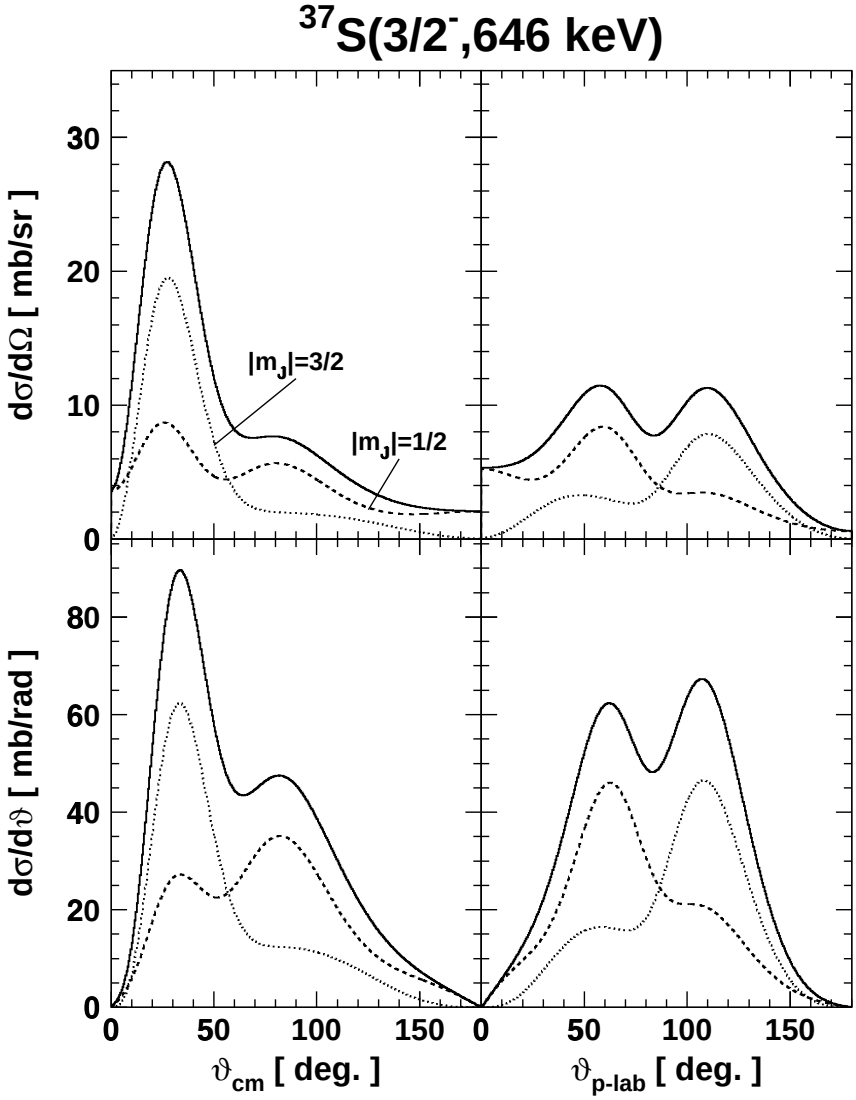

Figure 5.2: Calculated differential cross sections for the total population and the population of the m-substates of the $3/2^-_1$ level at 646 keV in the lab- and cm-system for the ^{2}H(^{36}S,^{37}S)p-reaction [Len98b]. Although the differential cross sections of the m-substates are quite different, the total (angle integrated) cross sections to populate the m-substates are almost equal.

of the ground state is observed. As can be seen, the nucleon transfer enables a backward emission of the light particle even for small negative Q-values.
One aim of the experiment was the measurement of the differential cross section of the ^{2}H(^{36}S,^{37}S)p-reaction for comparison with theoretical predictions (see Figure 5.2). As it was impossible to determine these cross sections by detecting the heavy reaction product, auxiliary particle detectors in both forward and backward direction had to be added in the experimental setup to detect the light reaction product and to complement the germanium detectors and the PPAC. The overall experimental setup will be discussed in the following section.

5.2 Setup of the REX-ISOLDE Test Experiment

5.2.1 Overall Setup

The overall setup is shown in Figure 5.3. Two 6-fold segmented MINIBALL germanium modules were used and placed at an angle of ϑ_{det}=90° with respect to the beam axis with a target distance of 10.6 cm, which is the minimum target distance at REX-ISOLDE. It should be noted that for the ^{2}H(^{36}S,^{37}S)p reaction this angle corresponds to the most unfavourable condition for the Doppler correction, since $\theta_{\gamma} \approx \vartheta_{\mathrm{det}} \approx 90°$ (the ^{37}S is scattered by less than 2.5°).
The position-sensitive REX-ISOLDE PPAC was positioned at zero degrees with the entry foil 11 cm behind the target. With a thickness of 20 mm and diameter of 40 mm, the scattering angles from ϑ=0° to ϑ=9° were covered, so that all heavy reaction products of the ^{2}H(^{36}S,^{37}S)p reaction passed through the detector (see Figure 5.1, $\vartheta_{^{37}\mathrm{S-lab}} < 2.5°$). At low beam intensities it was thus possible to count every single beam particle and to obtain a coincidence signal for background suppression. At higher count rates the detector was used as a current monitor. In order to avoid damage to the PPAC a mechanical shutter could be inserted in front of the PPAC, when the beam intensities exceeded the maximum current the PPAC foils could stand.
Two auxiliary silicon particle detectors were employed. A silicon ring detector with a thickness of 2 mm was placed at a distance of 12 mm away from the target covering backward angles from ϑ=120° to ϑ=150°. The detector was used to

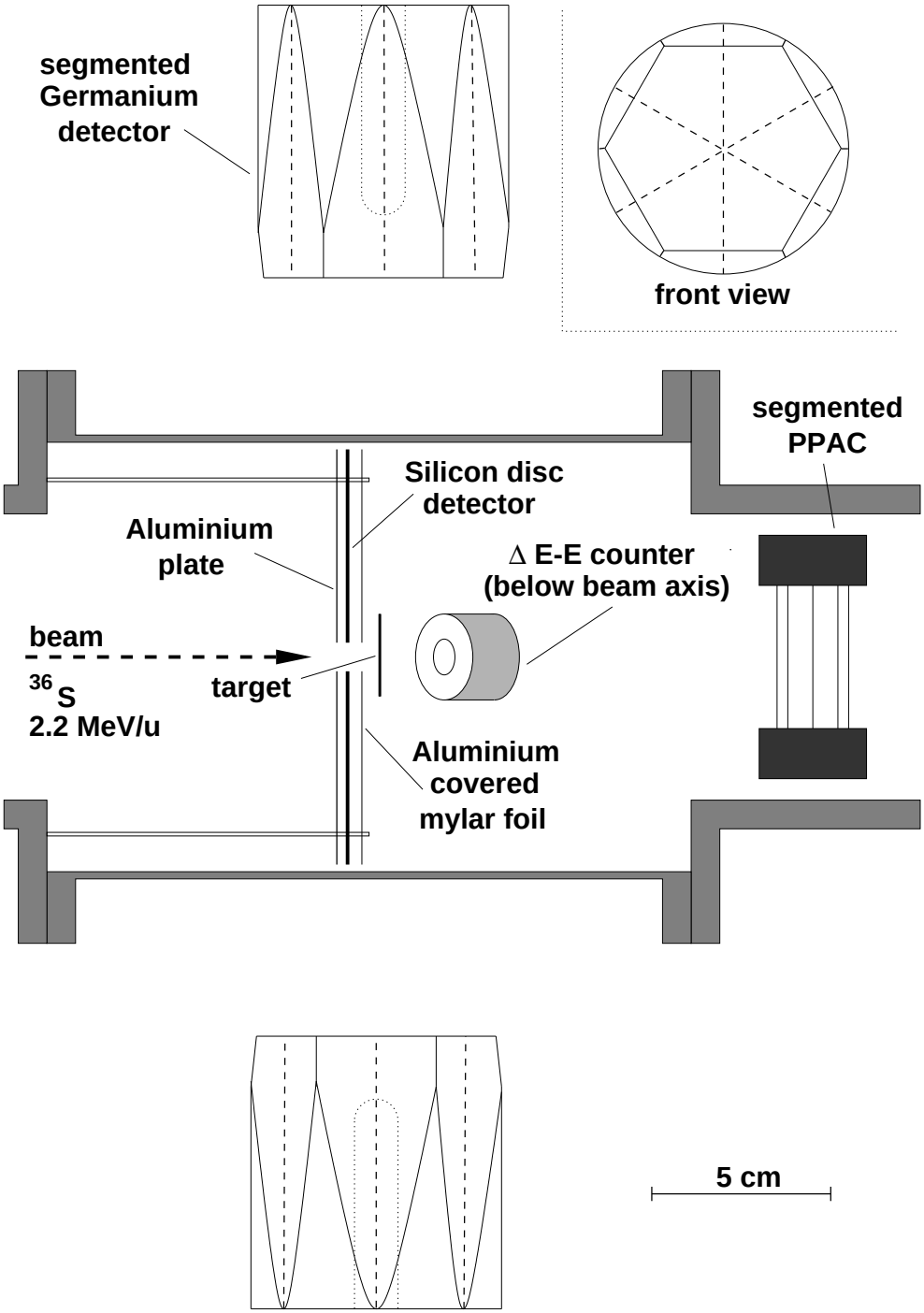

Figure 5.3: Schematic view from above on the experimental setup of the REX-ISOLDE test experiment. The target chamber is shown as cut in half. The ΔE-E-counter is positioned below the cutting plane at an angle of 40° with respect to the beam axis.

detect light reaction products, which were scattered in backward direction. The expected energies of these particles were too low to permit the use of a silicon telescope detector.

In forward direction a small ΔE-E-counter with an active area of 50 mm^2 and thicknesses of 50 μm and 1500 μm, respectively, was located at a distance of 30 mm away from the target at an angle of $\vartheta_{\Delta E-E}$=40° from the beam axis. The main application of this detector was the selection of reaction channels by identifying particles created in the reaction. At REX-ISOLDE this small telescope will be replaced by a large annular silicon disc telescope detector.

Both silicon detectors were covered with aluminized mylar foils (areal density 0.2 mg/cm^2) to prevent electrons and heavy ions from entering the detectors. The silicon disc detector was protected against the beam by an aluminium shield on the back side.

A sulfur beam was provided from the MPI-K tandem accelerator. The linear postaccelerator was used to bunch the beam with a frequency of 13.56 MHz (74 ns) and a bunch width of ∼1 ns and to select the desired isotope. A $^{36}S^{8+}$ beam with an energy of 79.2 MeV (2.2 MeV·A) was used as the projectile, while deuterium enriched polythene (∼99% CD_2, ∼0.5 mg/cm^2) and ^{9}Be (0.54 mg/cm^2) were used as target materials. The CD_2 targets (0.48 and 0.55 mg/cm^2) had a gold backing (0.17 mg/cm^2) to both cool the CD_2 and to monitor the beam intensity by Rutherford scattering using the silicon telescope detector. A target anchor with three frame holders was used; one CD_2 target, the beryllium target and an additional collimator were mounted simultaneously. The beam intensity was varied between $2{\cdot}10^5$ and $6{\cdot}10^8$ particles per second (pps).

5.2.2 The Data Acquisition Electronics

The setup of the VME-based data acquisition system is shown in Figure 5.4. It was started by a particle-single trigger from one of the silicon detectors or by a γ-single trigger from one of the germanium detectors. The timing of the trigger was determined by the accelerator RF pulse.

Both the silicon ring detector and the silicon ΔE-E-detector delivered energy and timing signals. The energy signals were obtained from the preamplifier pulse using a main amplifier (MA), the timing signals were generated in constant frac-

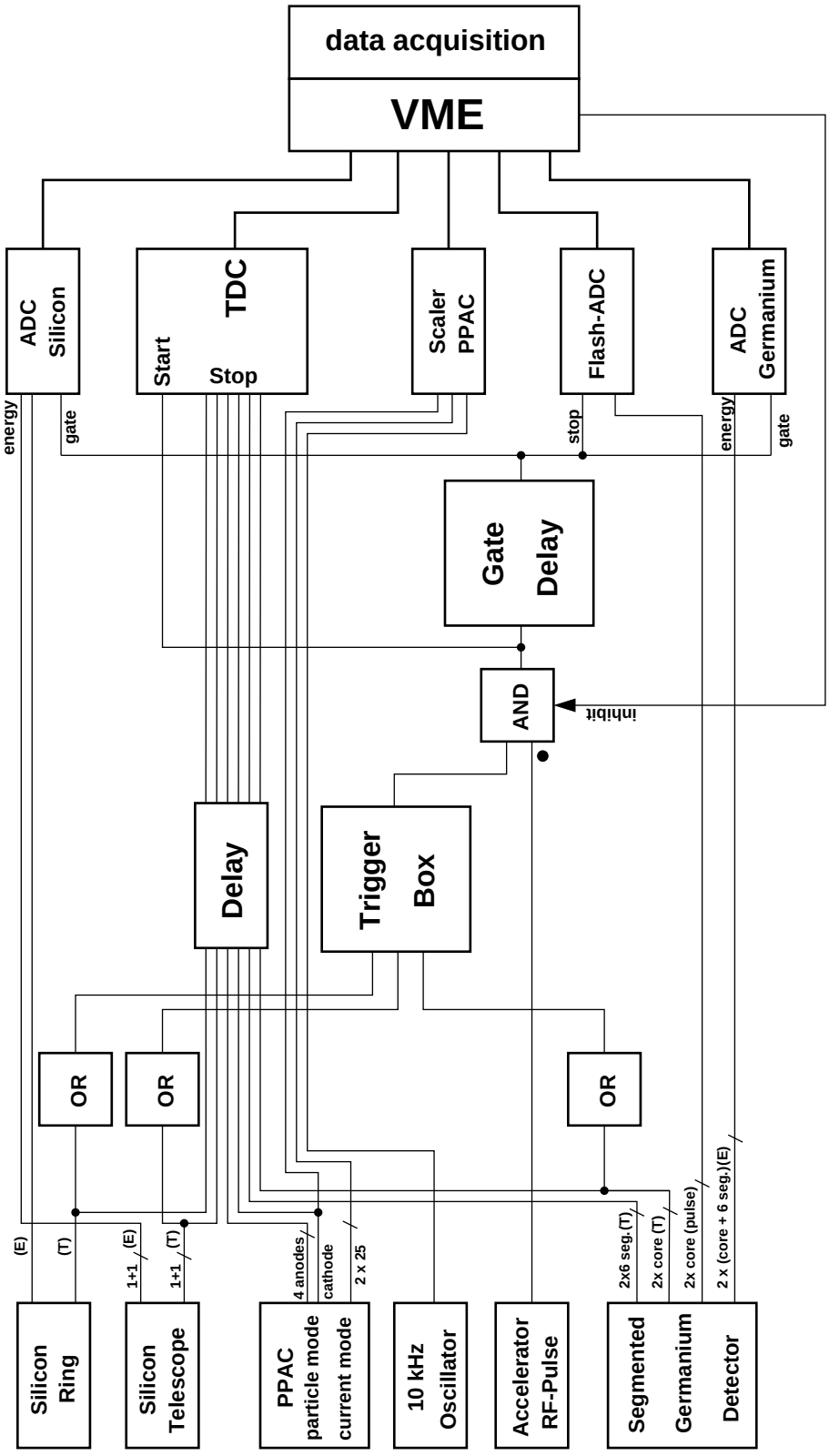

Figure 5.4: Block diagram of the data acquisition electronics

tion discriminators (CFD) from the differentiated preamplifier signals produced in a timing filter amplifiers (TFA). For clarity all main amplifiers, timing filter amplifiers, and constant fraction discriminators are not explicitly drawn in the diagram. The energy signals were converted in 12-bit ADCs, the timing signals were used both as trigger signals and as stop signals for time-to-digital converters (TDC).
The PPAC was operated either in particle or in current mode (see following section). In either mode the PPAC did not contribute to the trigger.
When operated in particle mode the PPAC provided a TDC-stop signal from the cathode for every beam particle detected. The position of the beam particle could be derived from the four anode stop signals. All timing signals were generated by directly connecting a CFD to the amplified PPAC pulse. In addition the cathode signal was connected to the scaler to directly count the number of incident beam particles.
In current mode every anode strip was connected to a current-to-frequency converter. The different frequencies were monitored in a scaler. As the scaler was not read out regularly, it was necessary to feed one scaler channel with a 10 kHz signal to be able to calculate absolute frequencies for the other channels.
Each germanium detector delivered 7 energy and timing signals, one for the core and 6 for the segments. These signals were generated by using main amplifiers and TFA-CFD-chains, respectively. Furthermore the preamplifier signal of the core was differentiated in an additional timing filter amplifier (T_{diff}=50 ns, T_{int}=20 ns) and continuously digitized in a 250 MHz 8-bit Flash-ADC, so that the core current pulses were readily available for the steepest-slope algorithm. Only the core timing signals were used in the trigger. The energy signals were analyzed by high resolution (13-bit, for germanium) ADCs, all timing signals were used as stop signals for TDCs.

5.2.3 The Position Sensitive PPAC

In experiments with extremely low beam intensities the background γ-rays detected in the germanium array outnumber the nuclear reaction γ-rays by orders of magnitude. It is therefore mandatory to detect at least one charged particle produced in the reaction and to use a time coincidence to achieve a sufficient

background suppression.

At ISOL facilities like REX-ISOLDE high quality beams (low energy spread, sharp focus) are available. In order not to compromise these properties, the beam particle should not pass a detector before the target. For inverse transfer reactions on light target materials it is more favourable to detect the heavy particle (whose momentum hardly differs from the momentum of the beam particles), than the light particle, which, depending on the reaction, can travel at extremely low speed and in almost any direction, so that it is difficult to detect. The only limitation of this method is usually the high count rate in the forward detector, however, the count rate does not present a serious problem here, as the beam intensities are already low. A new position sensitive PPAC for REX-ISOLDE has therefore been developed at the TU-Darmstadt [Cub99].

The PPAC consists of 5 metallized foils and is operated with isopropane at a gas pressure of 5 mbar. The circular active area has a diameter of 40 mm, the areal density (<1.5 mg/cm^2 mylar) is sufficiently low to allow particles to traverse the detector without stopping, so that the γ-background from β-decays of the projectiles can be kept as low as possible.

The central cathode foil in the middle of the detector is uniformly metallized on both sides and connected to the high voltage supply. Depending on the count rates the PPAC is operated at voltages between -350 V for high count rates and -700 V for low count rates. The signal from this foil has the best timing resolution ($\Delta t_{\mathrm{FWHM}} \sim 5$ ns at -350 V) and is therefore used for timing purposes.

Two foils segmented with aluminium strips with a pitch[1] of 1.6 mm are used as anode foils. The two foils are oriented perpendicularly permitting x- and y-resolution. The resulting position resolution is limited by the pitch of the strips ($\Delta x, \Delta y \approx 1.6$ mm).

In order to guarantee a reliable operation of the PPAC homogeneous electric fields are necessary between the anode and cathode foils. Thus an entry foil and an exit foil are necessary to prevent the anode foils from bending due to the pressure difference inside and outside the PPAC.

The electronics of the anode foils can be operated in two modes. In the *particle mode* the strips are connected via delay lines and 2 preamplifiers are used for each

[1] the distance between the middles of two strips

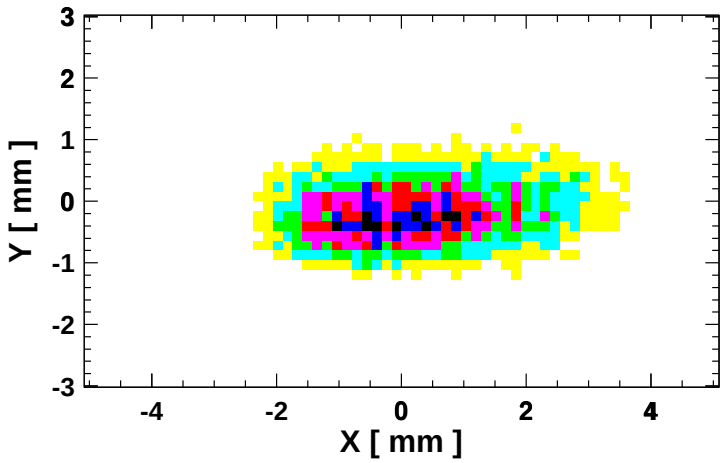

Figure 5.5: Beam spot of the ^{36}S-beam measured with the REX-ISOLDE PPAC at a beam intensity of 10^6 pps.

foil. The entry position of the particle can be derived from the CFD-time differences between the preamplifier signals, as can be seen in Figure 5.5. In *current mode* each strip is connected to a current-to-frequency converter and a scaler, so that the x- and y-projection of the beam can be derived from scaler spectra. This mode is especially useful for positioning the beam at high rates. It can be used between 10^4 and $5{\cdot}10^7$ pps.

In single particle readout mode an efficiency of more than 99% was measured with α-particles (1.4 MeV$\cdot A$) from an Am-source at a particle rate of 10^3 pps. In the in-beam experiment a certain loss of efficiency was observed at very high rates. At a particle rate of 10^6 pps an efficiency of 70% was found for the PPAC. This efficiency was determined by comparing the peak area of the strongest ^{37}S γ-line at 646 keV produced in the ^{2}H(^{36}S,^{37}S)p reaction in a spectrum in coincidence with the PPAC with the peak area in a spectrum without this coincidence. The efficiency rapidly decreased to 50% at a measured rate of $1.5{\cdot}10^6$ pps, finally a saturation rate of about $3{\cdot}10^6$ detected particles per second was reached.

Similar limitations exist for the position resolution of the PPAC. At a particle

rate of 10^3 pps the position can be determined for almost all events, but above 10^5 pps the anode signals of the PPAC degrade and a position determination is only possible for a small fraction of all events.
The REX-ISOLDE PPAC is ideally suited to obtain a time coincidence and to count beam particles. It is not recommended to use the PPAC in particle mode with rates above 10^6 pps, as too many particles pass the detector undetected. The position information can only be used below 10^5 pps, for higher rates the fraction of events with at least one missing anode time exceeds the number of events with full position information.

5.2.4 The Segmented Germanium Detector

Two MINIBALL modules were employed to measure the γ-rays emitted from the excited nuclei produced. In order to obtain a spectrum with a good low-energy resolution one module was operated with an energy range from 0 MeV to 1.5 MeV, the other module covered the whole spectrum up to 4 MeV, so that it was also possible to detect high energy γ-rays. Unfortunately, the cold FET of the module covering the low-energy range broke down during the experiment, so that this module was only available for the measurements with the beryllium target, which were performed first.
The module covering the small energy range was calibrated using a fifth order polynomial derived from a spectrum measured with a ^{152}Eu source. The ^{152}Eu source was also employed to obtain the low energy data for the calibration of the other module, it was however more challenging to calibrate the upper energy range of the high energy detector, as no suitable high energy γ-sources were available. Besides a ^{24}Na source (E_γ=1369 keV,2754 keV), which was employed only once at the end of the beamtime, only the natural background γ-rays of ^{214}Bi (E_γ=1765 keV) and ^{208}Tl (E_γ=2614 keV) were available for the calibration. It was nevertheless possible to obtain a good calibration even for higher energies, as the β-decay of ^{37}S ($\sim$5 min halflife) produced in the reaction yielded a high energy γ-line at 3103 keV, when the shutter was inserted in front of the PPAC. The ^{152}Eu spectrum together with the high energy lines obtained from the background and the β-decay were used to derive a fifth order polynomial for the calibration of the high energy module.

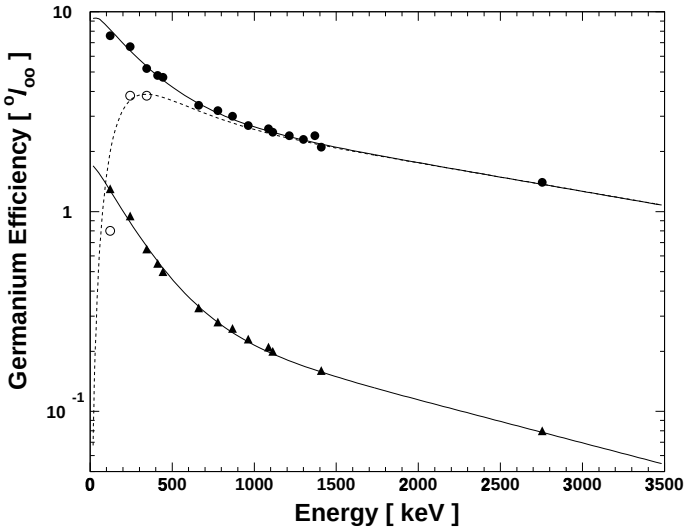

Figure 5.6: Efficiency of a single MINIBALL crystal operated at a target distance of 10.6 cm. The FEP efficiency of the core contact is shown by filled circles, the efficiency of a segment is shown by filled triangles. Both efficiencies were determined using a long coincidence time window (350 ns). When a narrow time window (50 ns) is applied, the FEP efficiency of the core strongly decreases for low energies (hollow circles).

The stability of the electronics and in consequence the calibration is usually a major concern in γ-ray spectroscopy. However, this was not the case in this experiment. As the low beam intensity ensured that the germanium spectrum was dominated by background γ-rays, the calibration was monitored continuously. It would have been possible to calibrate the spectra even without using γ-sources. γ-ray spectroscopy with radioactive beams requires a germanium array with an excellent full-energy-peak efficiency (FEP efficiency) at moderate γ-multiplicities. MINIBALL was especially designed for this kind of experiment. For a single MINIBALL germanium crystal operated at a target distance of 10.6 cm the energy-dependent in-beam efficiency of the core and one segment was measured as a function of energy (see Figure 5.6). Sources with a calibrated activity (^{137}Cs, ^{152}Eu) and γ-γ-coincidence sources (^{24}Na,^{152}Eu)[2] were used. Furthermore the γ-γ-coincidence calibrations were employed to investigate the influence of coincidence-

[2]In the coincidence calibration γ-cascades are required. The first γ-ray is detected in a trigger detector, the second one in the germanium detector to be tested. Only coincidence events, where the transition populating (or depopulating) the intermediate state is observed in the trigger detector, are used to accumulate the γ-spectrum of the detector under test. For the efficiency calculations one has to account for the angular correlation of γ-rays in the cascade.

time windows on the efficiency. For this purpose the FEP efficiency of the core was determined for a wide and a narrow time window of 350 ns and 50 ns, respectively. For the core an in-beam efficiency of 0.23 % has been measured at 1.3 MeV, as can be seen in Figure 5.6. Compared with the results from the simulations and the calibrated-source measurements (Figure 4.2) the in-beam efficiencies are almost 50% lower than the simulated efficiencies. These losses cannot only be attributed to a module with reduced efficiency[3] or events caused by glitches[4], which can reduce the efficiency of the electronics. They demonstrate, how excess material in the target chamber, in this case the target holder, the chamber wall and the silicon ring detector, can considerably reduce the overall γ-detection efficiency of an experimental setup.

A comparison of the FEP efficiency of the core for a narrow and a wide coincidence window reveals, how strong the FEP efficiency in the energy range below 500 keV depends on the width of the coincidence window. For a very small coincidence window the low-energy FEP efficiency is dramatically decreased. The reason for this behaviour is a delay of the timing signal caused by the CFD. Pulses with a long rise time and a small peak height take very long to surpass the threshold the CFD needs to separate signal from noise.

As all components of the experimental setup are presented, it is now possible to proceed with the results of the experiment. At first, the Doppler correction, which can be achieved in REX-ISOLDE experiments using the MINIBALL γ-spectrometer, will be discussed, then the background suppression, which can be obtained by employing the REX-ISOLDE PPAC, will be presented, finally the performance of the particle detectors needed for the determination of differential cross sections will be depicted.

[3] in EUROBALL, where the same crystals are employed, a variation of the efficiency of 10 % has been observed [Tho95]

[4] e.g. accidental electric interference on the main power lines due to switching of large devices.

5.3 Feasibility Studies for REX-ISOLDE Experiments

5.3.1 Doppler Correction

In MINIBALL the detectors are positioned very close to the target. At large recoil velocities Doppler broadening is therefore considerable, and the width of a Doppler broadened peak grows with the solid angle covered by a single detector module.

In order to examine the capabilities of the segmented germanium detectors and to determine reliable line widths, the ^{2}H(^{36}S,^{37}S)p reaction without particle information was used allowing a high beam intensity of 40 pA (electrical, corresponding to $3{\cdot}10^{7}$ pps). In the analysis the scattering angle of the ^{37}S of up to 2.5° was neglected. Accounting for an energy loss of 10% in the target a β of 6.5% was used for the Doppler correction.

In the experiment it was not possible to position the MINIBALL modules with an accuracy of better than a few millimeters and, when the data were analyzed, the energies of all Doppler-corrected γ-lines proved to be too small. In order to obtain correct peak positions, the positions of the germanium detectors used in the analysis program therefore had to be shifted backwards in parallel to the beam axis by 2 mm and 5 mm respectively. The shift by 2 mm corresponds to a positioning of the detector at an angle of ϑ_{det}=91°, the shift by 5 mm to an angle of ϑ_{det}=93°. The position correction in the analysis program will also be necessary for MINIBALL, unless the detectors can be positioned with an accuracy of better than 1° deviation between the real and the assumed axis from the target to the detector. If a position correction is necessary, the correct detector positions have to be determined in an in-beam measurement with known γ-lines. Without any internal position information, an energy resolution of only 13.6 keV can be achieved for the ^{37}S line at 646.2 keV, as can be seen in Figure 5.7. This width is already reduced to 6.7 keV, as soon as the angle algorithm without segment pulse-shape analysis[5] (PSA) is applied to the segment energy pattern. If an

[5] Segment-pulse-shape analysis was not yet available in this measurement.

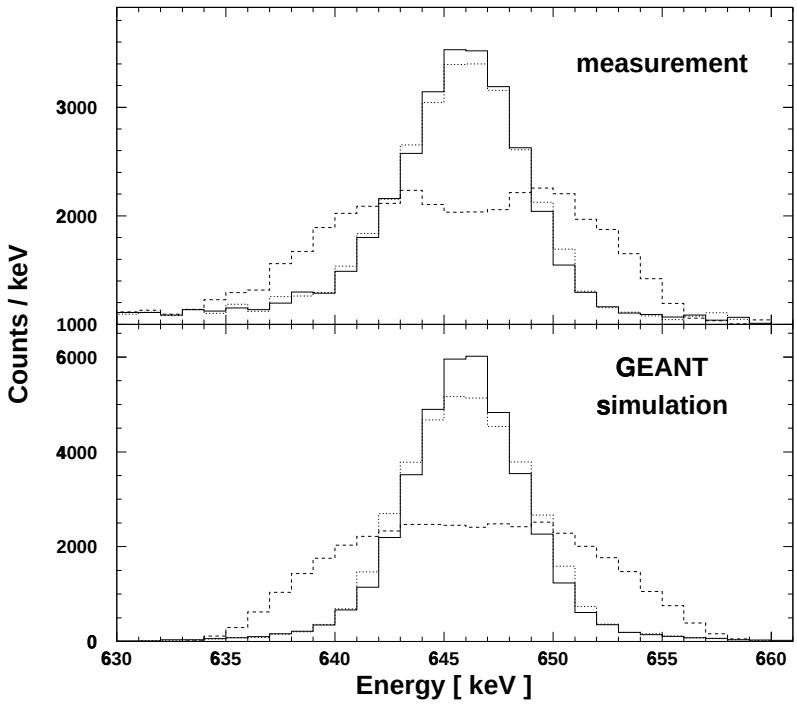

Figure 5.7: Measured and simulated Doppler correction for the ^{37}S line at 646.2 keV at a target distance of 10.6 cm, β=6.5%, and ϑ_{det}=90° (91°). The measured γ-single spectrum was accumulated in 9 hours beamtime with an intensity of 40 pA (electrical, corresponding to $3{\cdot}10^7$ pps). The kinematics of the transfer reaction was used for the Doppler correction, for the measurements the scattering angle of ^{37}S was neglected, for the simulations it was included.
Dashed line: Doppler correction without angular information of the segments.
Dotted line: Doppler correction using segment information only.
Solid line: Doppler correction using both segment and radius information.

additional radius information[6] derived by the steepest-slope-algorithm is used, the width can be further enhanced to 6.2 keV. At this energy the intrinsic resolution is 1.7 keV, so that an actual Doppler broadening of 6.0 keV is obtained. Allowing for a radius uncertainty of ± 5 mm the GEANT simulation gives similar results (13.5 keV, 6.3 keV, 5.6 keV). The differences between the simulation and the measurements are probably due to the scattering of the projectile of up to 2.5°. A simulation including the scattering angle resulted in differences of $\approx$0.1 keV. A full pulse simulation including the basic angle algorithm, pulse-shape analysis of the radius, and pulse-shape analysis for angular refinement has been performed. From this simulation an energy resolution after Doppler correction of 3.6 keV is derived, if the flight direction of the γ-emitting nucleus is exactly known. A simulation which includes the unknown scattering of the projectile yields an energy resolution after Doppler correction of 4.7 keV, however both values are unrealistic, as the intrinsic energy resolution of the module will be no longer negligible.

5.3.2 Background Suppression

The background suppression achieved with the REX-ISOLDE PPAC has been determined by investigating the ^{2}H(^{36}S,^{37}S)p reaction at a low intensity of 10^6 pps. The results of these measurements are illustrated in Figure 5.8. As can be seen in the raw germanium spectrum, the deexcitation γ-line of the first excited state of ^{37}S populated in the ^{2}H(^{36}S,^{37}S)p reaction is hardly visible between the sharp natural background peaks.

Then the Doppler correction has been applied (in which the scattering angle of the ^{37}S has been neglected). While the width of the deexcitation γ-line is strongly reduced, so that the line becomes more prominent, the natural background lines are broadened. The assignment to different segments or segmentation lines results in a double-humped structure of the background lines caused by the false Doppler correction. The sharp dip between the humps also reflects the reduced efficiency in the centre of the detector that is caused by the core hole.

[6]The radius information was only used in this measurement, for all other spectra a fixed radius of 2.0 cm was assumed, as the radius determination was only available for the energy region between 600 keV and 700 keV. (see section 4.2)

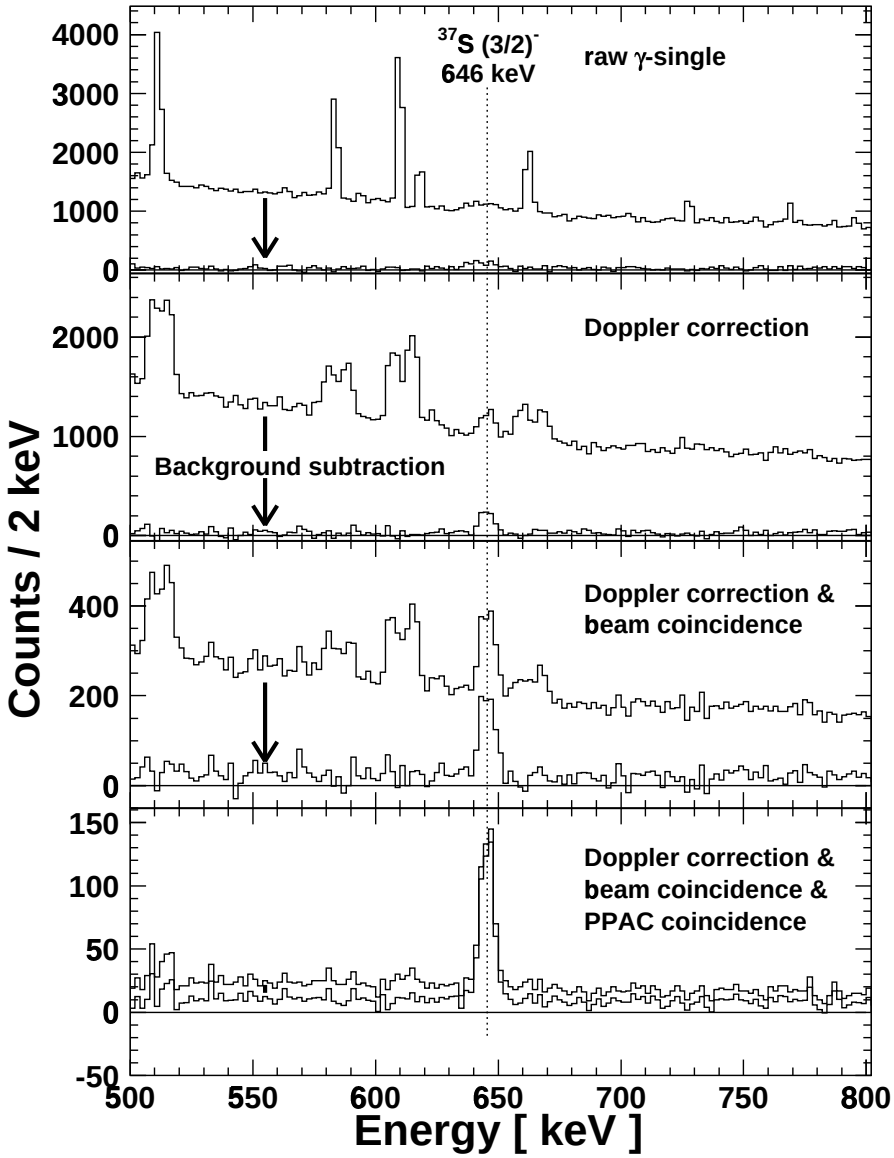

Figure 5.8: γ-spectra of the ^{2}H(^{36}S,^{37}S)p reaction for one germanium module (target distance 10.6 cm, ϑ_{det}=91°) after a beamtime of 7 hours with an intensity of 10^6 pps. The top spectrum shows the raw γ-single spectrum with no coincidences and no Doppler correction. In the second Doppler-corrected γ-single spectrum the 646 keV line of ^{37}S becomes visible. For the Doppler correction the transfer kinematics has been used, a β of 0.065 has been assumed and the scattering angle of the ^{37}S has been neglected. An additional coincidence with the accelerator RF yields the improved peak-to-background ratio of spectrum 3. The bottom spectrum shows that the additional coincidence with the PPAC yields an essentially background-free spectrum. For all spectra the spectrum after background subtraction is depicted to demonstrate how the different steps of background suppression reduce the background still contained in the spectrum.

With the aid of the Doppler correction the deexcitation line can be separated from the background, yet only a peak-to-background ratio of 10% is achieved. Therefore a coincidence of the germanium signal with the RF of the accelerator has been required. The background is then reduced by more than a factor of 5. The peak areas of both spectra agree within statistical limits, i.e. the detector efficiency is not reduced by the background reduction.
An additional coincidence with the PPAC has been used to obtain further background reduction. Due to the lower efficiency of the PPAC at high particle rates, the peak area has suffered from a loss of 30%, yet the background is reduced by another factor of 13. This reduction is equivalent to the ratio of the beam bunch frequency of 13.56 MHz to the particle rate of 10^6 pps. This means that only every 13th beam bunch is filled and the background γ-rays accumulated are rejected when an empty beam bunch arrives.
For all spectra a background subtraction has been performed. These background-subtracted spectra are shown to visualize the pure background, which is the difference between the two curves in each spectrum. The background spectrum has been derived from the same data gathered in the ^{2}H(^{36}S,^{37}S)p reaction at a low-intensity of 10^6 pps by requiring an anti-coincidence with both the PPAC and the accelerator RF, the weighting factor for the subtraction has been derived by requiring that the spectrum had to be flat at the position of the strongest background line (^{40}K)[7]. While the background dominates the first raw germanium spectrum, the peak-to-background ratio can be reduced by applying the Doppler correction and the coincidence with the accelerator RF. When finally the coincidence with the PPAC is required only a negligible background is observed.

5.3.3 Particle Detection

In order to determine differential cross sections for the reaction with the deuterium target (^{2}H(^{36}S,^{37}S)p) the detection of the light reaction product in both forward and backward direction is compulsory (see section 5.1), as the information about the kinematics of an event can hardly be extracted from the heavy reaction product.

[7] If the spectrum still showed the double hump, the factor would be too small, if a double valley occurred, the factor would be too big.

As can be seen in Figure 5.9, the unambiguous identification of the protons emitted in forward direction is ensured, as soon as a silicon telescope detector is used to separate the proton and the deuteron signals. The energy deposition of a proton in the second silicon counter (E-ΔE) is so high that the signal obtained is well separated from noise. An easy detection of the light reaction product is therefore guaranteed, as soon as the particle is emitted in forward direction ($\vartheta < 90°$).
In order to detect light particles emitted in backward direction a silicon disc detector (see Figure 5.3) was used, as the low energy of particles emitted in backward direction impedes the use of a silicon telescope. For to be able to identify the protons detected in the disc detector, a two-dimensional plot of energy versus time for signals from the silicon disc detector (mounted in backward direction) observed in the ^{2}H(^{36}S,^{37}S)p reaction was produced for events with an energy deposition (in the silicon disc detector and) in the germanium detector.
When a γ-energy of 646 keV was required (upper panel of Figure 5.10), which corresponds to the first excited state of ^{37}S, the separation of protons from noise became visible – a cross check with a germanium spectrum filled with events, which had a silicon disc detector time between -50 ns and 50 ns and an energy deposition between 1 MeV and 2 MeV yielded an almost pure line at 646 keV –, however for higher γ-energies (lower panel) only noise was observed, although states with a higher excitation energy were populated in the ^{2}H(^{36}S,^{37}S)p reaction.
A more detailed analysis of the measurement revealed that it was almost impossible to separate noise from pulses due to incident particles. Only very few protons emitted in the population of the $3/2^{-}_{1}$ level at 646 keV could be identified when a higher state was excited the low-energy protons could not be observed. The noise level of the detector and the electronics available for the experiment was too high to permit a quantitative measurement of the protons scattered in backward direction. Hence, a silicon detector with an extremely low noise level is needed for future experiments to measure the protons in backward direction.
In the end the determination of a measured differential cross section was omitted. It proved to be too difficult to quantitatively measure the protons emitted in backward direction. Furthermore the analysis of the proton data of the detector in forward direction caused problems, which had not been considered when the

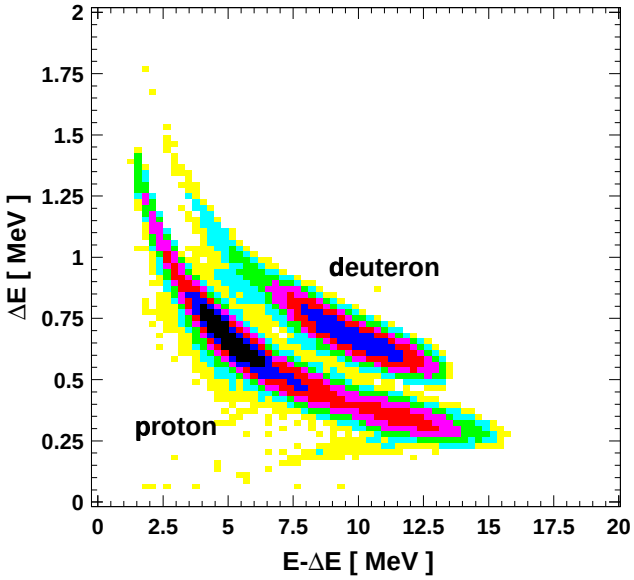

Figure 5.9: Two-dimensional energy spectrum (ΔE vs. E-ΔE) of the two silicon detectors in the telescope. The protons produced in the ^{2}H(^{36}S,^{37}S)p reaction are well separated from the elastically scattered deuterons.

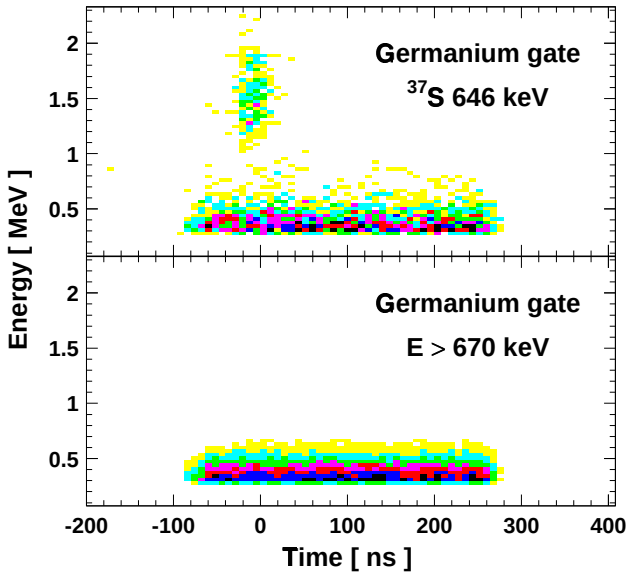

Figure 5.10: Two-dimensional plot of energy versus time for signals from the silicon disc detector (mounted in backward direction) observed in the ^{2}H(^{36}S,^{37}S)p reaction. Only events, which are coincident with a γ-ray are depicted (broad coincidence window: $\sim$400ns), the time is measured relative to the germanium detector. In the upper panel all events, which are coincident with the ^{37}S deexcitation line at 646 keV are depicted, in the lower panel all events, which are coincident with a γ-ray of at least 670 keV are shown.

experimental setup was planned. As only one germanium detector and only one point-like particle detector were used, the angular correlation between the direction of proton emission and γ-emission had to be considered in the calculation of the differential cross section, however the angular correlation was also unknown.

The feasibility of REX-ISOLDE experiments with a beam of low intensity and an energy of 2.2 MeV$\cdot A$ has been demonstrated. The Doppler correction of a single MINIBALL module has been tested using the basic angle algorithm and the steepest-slope algorithm for position resolution within the module. For a module positioned at the most unfavourable angle a relative energy resolution of $< 1\%$ has been obtained for the deexcitation line of the first excited state of ^{37}S at an energy of 646 keV. In MINIBALL a further improvement is expected, as segment PSA will be available, and not all modules will be positioned at the most unfavourable angle. The background reduction obtained with the aid of the REX-ISOLDE PPAC has been tested. As the PPAC allows to reject background γ-rays accumulated, when an empty beam bunch arrives, a major improvement of the background reduction will be obtained from this device. However it is difficult to satisfy all requirements in one experimental setup. As the Doppler correction becomes easier, when a deuterium target is used, the determination of differential cross sections gets more demanding, because the heavy reaction product cannot be used for the reconstruction of the kinematics, and the protons emitted in backward direction can hardly be detected.

5.4 Deuteron Induced Transfer

The feasibility studies of γ-ray spectroscopy experiments at REX-ISOLDE are completed, now the nuclear physics results of the experiment are to be discussed and the cross section predictions for the ^{2}H(^{36}S,^{37}S)p reaction have to be compared with their corresponding experimental values.

5.4.1 Reaction Channels of the CD_2-Target

When a deuterium target is used, the two strongest reaction channels are the neutron and the proton pickup. As REX-ISOLDE is designed to explore new regions

of unknown nuclei, this is an important advantage, as the observed γ-transitions need to be assigned to the population of only two possible nuclei. Furthermore the deuteron is the lightest of all possible neutron donors, so that the resulting transfer nucleus travels at about the same speed and in the same direction as the beam particles allowing a Doppler correction even without particle detection.
As it is difficult to use a pure deuteron target, deuterium enriched polythene $(CD_2)_n$ is widely used as a target material. Polythene is easy to handle and foils of any desired thickness can be produced.
In Figure 5.11 the Doppler-corrected germanium γ-spectrum in coincidence with the PPAC and the accelerator RF is shown. For the Doppler correction the transfer reaction kinematics with a β of 0.065 have been used, and the scattering angle of the heavy reaction product has been neglected. Two different kinds of peaks can be distinguished. A series of double-humped background peaks, which have been broadened due to the false Doppler correction, are visible. In addition sharp lines can be seen.
In the neutron transfer channel to ^{37}S two strong deexcitation lines are observed. The transition at 646 keV corresponds to the deexcitation of the first excited state of ^{37}S, the $3/2^-_1$ level at 646 keV, into the ground state (see Figure 5.13 and Table 5.1). The transition at 1993 keV is a doublet, both the deexcitation of the $1/2^-_1$ at 2638 keV into the $3/2^-_1$ level and the deexcitation of the $3/2^-_2$ level at 1992 keV into the ground state yield γ-rays at this energy. An additional weaker line is visible at 1347 keV corresponding to the transition of the $3/2^-_2$ into the $3/2^-_1$ level.
In the proton transfer channel, which leads to ^{37}Cl, the population of four states is observed, which all decay into the ground state. At 1727 keV a ^{37}Cl line is visible ($1/2^+_1 \rightarrow 3/2^+_{gs}$). The peak at 3.1 MeV is too broad for a single line, it is related to a doublet of ^{37}Cl lines at 3086 keV ($5/2^+_1 \rightarrow 3/2^+_{gs}$) and 3103 keV ($7/2^-_1 \rightarrow 3/2^+_{gs}$). An additional small line occurs at 3748 keV ($7/2^-_1 \rightarrow 3/2^+_{gs}$).
The lines at 890 keV, at 1122 keV, and at 1289 keV could not be assigned to either the two isobars (^{37}S, ^{37}Cl) nor to any other reaction of ^{36}S with the deuteron. They were due to transitions in ^{46}Ti ($2^+_1 \rightarrow 0^+_{gs}$, $4^+_1 \rightarrow 2^+_1$, $6^+_1 \rightarrow 4^+_1$) populated in the fusion evaporation reaction ^{12}C(^{36}S,^{46}Ti2n), as could be demonstrated by comparing the spectrum Doppler-corrected for one-nucleon transfer kinematics

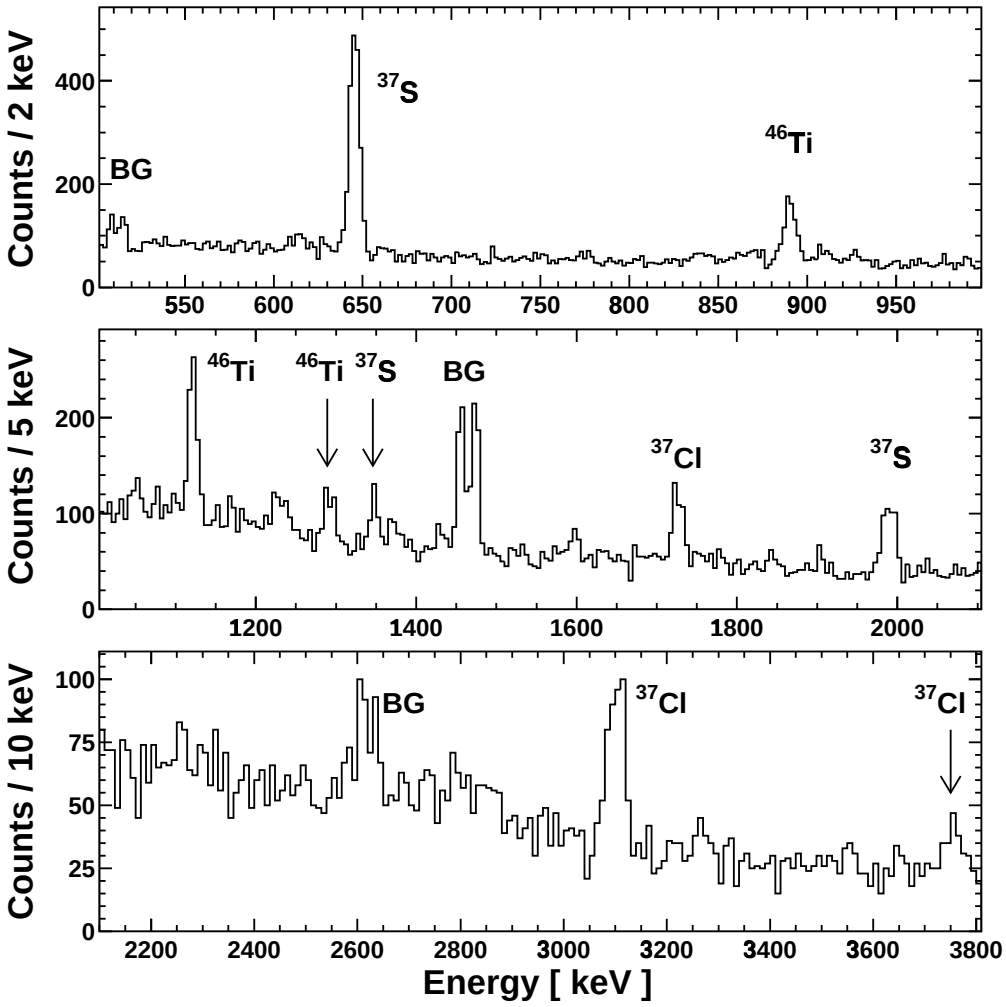

Figure 5.11: Doppler-corrected PPAC-gated germanium spectrum observed in the ^{36}S$\longrightarrow$(CD$_2$)$_n$ reaction at 2.2 MeV$\cdot A$. The spectrum was taken in 24 hours beamtime at a rate of $1{\cdot}10^6$ pps with a single germanium detector at ϑ_{det}=91°. For the Doppler correction the transfer kinematics were used, a β of 0.065 was assumed and the scattering angle of the ^{37}S was neglected. The spectrum corresponds to the fourth spectrum of Figure 5.8 (coincidence with the PPAC and the accelerator RF), however, the full statistics are shown.

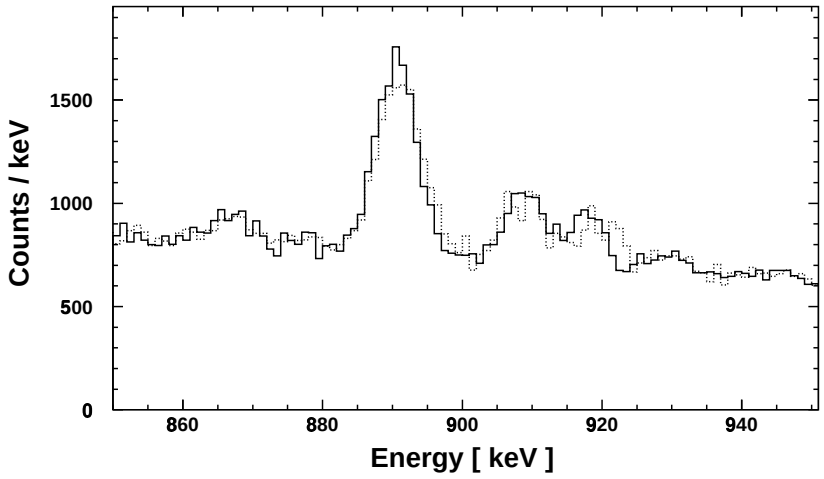

Figure 5.12: Doppler-corrected γ-single spectrum observed in the $^{36}S \longrightarrow (CD_2)_n$ reaction at 2.2 MeV·A. The spectrum was accumulated in 9 hours beamtime with an intensity of 40 pA (electrical, corresponding to $3 \cdot 10^7$ pps). The width of the line at 889 keV, which is due to a transition in ^{46}Ti produced in the fusion evaporation reaction $^{12}C(^{36}S,^{46}Ti2n)$, can be reduced from 7.6 keV to 6.8 keV when the proper kinematics for the fusion reaction (solid line) are used for the Doppler correction instead of the transfer kinematics (dotted line).

with the spectrum corrected for fusion-evaporation kinematics (see Figure 5.12). When the γ-line of ^{46}Ti is Doppler corrected using the transfer kinematics, a width of 7.6 keV is obtained, whereas a width of 6.8 keV is obtained, when the correct fusion-evaporation kinematics is applied. For the position of the two lines a shift of -0.4 keV is expected, as the different values for β (β_{trans}=0.065, β_{fus}=0.057) result in different γ-factors for the Doppler correction (γ_{trans}=1.0021, γ_{fus}=1.0016). The Doppler-shift difference caused by the positioning of the germanium detector at ϑ_{det}=91° accounts for less than -0.1 keV. The measured shift of -0.5(1) keV (890.7 keV, 890.2 keV) agrees reasonably well with this prediction. Two different methods are possible to distinguish between transfer and fusion channels. When γ-lines produced in fusion reactions are Doppler corrected with the transfer kinematics a false peak position will be obtained especially for modules in forward and backward direction. As a result the fusion lines in the Doppler-corrected sum spectrum of all detectors will be broadened. Yet this method will be problematic if the content of a questionable peak is too small to show significant broadening. In this case a measurement with a carbon test target can

be used to unambiguously identify the line.
In the $^{36}S \longrightarrow (CD_2)_n$ reaction three reaction channels have been observed. Besides the neutron and the proton transfer channels of the ^{36}S with the deuteron, the fusion evaporation channel $^{12}C(^{36}S,^{46}Ti2n)$ has been encountered. Three γ-lines can be attributed to transitions in ^{37}S, four to transitions in ^{37}Cl, and three to transitions in ^{46}Ti. The fusion-evaporation channel can be separated from the transfer channels using kinematic considerations.

5.4.2 Cross Section Calculations

The different reaction channels observed, when the CD_2 target is used, have been presented. In the following the determination of cross sections will be discussed. The experimental setup allowed to easily determine absolute cross sections, since all pulses from the REX-ISOLDE PPAC were counted in a scaler, so that the total number of ^{36}S ions which had passed the target during beamtime was available. In addition the number of counts in the 646 keV line of ^{37}S was determined in a γ-spectrum coincident with the PPAC. With the known deuterium areal density of the CD_2 target and the efficiency of the germanium detectors ε_{Ge} it was possible to calculate the absolute cross sections for the population of the excited states of ^{37}S as follows:

$$\sigma_\gamma(E_\gamma) = \frac{N_{\gamma-\mathrm{PPAC}}(E_\gamma)/(\varepsilon_{\mathrm{Ge}}(E_\gamma)\cdot\varepsilon_{\mathrm{PPAC}})}{(N_{\mathrm{PPAC}}/\varepsilon_{\mathrm{PPAC}})\cdot(N/A)_{\mathrm{deuteron}}} = \frac{N_{\gamma-\mathrm{PPAC}}(E_\gamma)/\varepsilon_{\mathrm{Ge}}(E_\gamma)}{N_{\mathrm{PPAC}}\cdot(N/A)_{\mathrm{deuteron}}} \qquad (5.2)$$

Here $\sigma_\gamma(E_\gamma)$ is the total cross section for the occurrence of a γ-line at the energy E_γ, $N_{\gamma-\mathrm{PPAC}}(E_\gamma)$ is the number of γ-rays, which were observed in the germanium detector in coincidence with the PPAC, $\varepsilon_{\mathrm{Ge}}(E_\gamma)$ is the energy dependent FEP efficiency of the germanium detector, $\varepsilon_{\mathrm{PPAC}}$ is the particle detection efficiency of the PPAC, N_{PPAC} is the number of beam particles counted in the PPAC, and $(N/A)_{\mathrm{deuteron}}$ is the deuteron areal density in the target given in particles/cm^2. The areal density of the CD_2 target, 0.55 mg/cm^2, corresponds to $(N/A)_{\mathrm{deuteron}} = 4.1 \times 10^{19}\mathrm{cm}^{-2}$ and $(N/A)_{^{12}\mathrm{C}} = 2.1 \times 10^{19}\mathrm{cm}^{-2}$.
It is important to note that the efficiency of the PPAC cancels out so that this method allows to derive absolute cross sections without the knowledge of the efficiency of the PPAC. One should also be aware that in equation 5.2, a possible angular correlation of the emitted γ-rays with the heavy reaction product is

neglected; the formula is exact for an isotropic γ-ray emission, for other angular distributions a correction factor is needed. A correction factor is not needed for the full MINIBALL array, as the array permits an isotropic detection of the emitted γ-rays. Using this method and the data accumulated in the 24 hour beamtime with a particle rate of 10^6 pps, an absolute cross section of 230(46) mb has been derived for the occurrence of the 646 keV γ-line of ^{37}S. The error comprises statistical errors, the error of the target thickness (5%), and the error of the germanium detector efficiency (15%).

Alternatively, it was possible to derive the number of beam particles which had passed the target by counting the ^{36}S particles that were Rutherford scattered by the gold backing. The energy spectrum of the ΔE counter, in which the ^{36}S particles were fully stopped, showed a high energy peak attributed to these particles. In addition the number of counts in the 646 keV line of ^{37}S was determined in a γ-spectrum coincident with the beam pulse (a coincidence with a particle detector was not required for this method). As the areal density of the deuterium in the target and the gold in the backing and the efficiency of the germanium detector was known the absolute cross section could be derived using

$$\sigma_\gamma(\mathrm{E}_\gamma) = \frac{(\mathrm{N}_\gamma(\mathrm{E}_\gamma)/\varepsilon_{\mathrm{Ge}}(\mathrm{E}_\gamma)) \cdot \sigma_{\mathrm{Rutherford}} \cdot (\mathrm{N/A})_{\mathrm{Au}}}{\mathrm{N}_{\Delta\mathrm{E}}(^{36}\mathrm{S}) \cdot (\mathrm{N/A})_{\mathrm{deuteron}}}. \tag{5.3}$$

$$\text{with} \quad \sigma_{\mathrm{Rutherford}} = \int_{\vartheta_{\Delta E-\min}}^{\vartheta_{\Delta E-\max}} \int_{\phi_{\Delta E-\min}(\vartheta)}^{\phi_{\Delta E-\max}(\vartheta)} \left(\frac{d\sigma}{d\Omega}\right)_{\mathrm{Rutherford}} d\phi \sin(\vartheta) d\vartheta$$

Here $N_\gamma(E_\gamma)$ is the number of γ-rays, which were observed in the germanium detector in coincidence with the accelerator RF, $\sigma_{\mathrm{Rutherford}}$ is the cross section for ^{36}S particles to be scattered in the solid angle covered by the ΔE silicon detector, $N_{\Delta\mathrm{E}}(^{36}\mathrm{S})$ is the number of ^{36}S particles counted in the ΔE silicon detector and $(N/A)_{\mathrm{Au}}$ is the areal density of gold given in particles/cm^2 (an areal density of 0.17 mg/cm^2 corresponds to $(N/A)_{\mathrm{Au}} = 5 \times 10^{17}\mathrm{cm}^{-2}$).

As before, the formula given in equation 5.3 is only exact for an isotropic γ-emission and a correction factor is needed to account for other angular distributions. For the occurrence of the 646 keV γ-line of ^{37}S a value of 175^{+175}_{-88} mb results from this method. The large error is due to large geometric uncertainties in the present experimental setup. As the beam spot of the experiment has a finite radius, the Rutherford-scattering method tends to underestimate the cross

section due to the positive second derivative of the Rutherford differential cross section. In REX-ISOLDE the large segmented ΔE-E silicon disc counter in forward direction will enable a more detailed analysis of the Rutherford scattered ^{36}S particles. It will thus be possible to use two alternative methods to obtain absolute cross sections.

As the absolute cross section for the occurrence of the strongest γ-line had been determined, it was aimed to deduce absolute cross sections for all γ-lines from relative cross sections. In a 9 hour beamtime with a current of 40 pA (electrical, corresponding to $3{\cdot}10^7$ pps) a germanium spectrum with high statistics was accumulated, so that relative cross sections could be determined. Together with the known absolute cross sections for the 646 keV line of ^{37}S it was thus possible to calculate absolute cross sections for all detected γ-lines.

A list of all γ-transitions observed is compiled in Table 5.1. As the detector shift is included in the Doppler correction, all measured energies agree reasonably well with the literature values [Fir96]. For prominent lines the error is determined by the positioning uncertainty of the detector module (e.g. the tilt angle of a detector with respect to the axis from the target to the detector, which is not included in the Doppler correction). Larger errors for smaller lines reflect the difficulty to exactly locate these lines in the spectrum. The high energy line at 3748 keV has the largest error, as the energy calibration above 3.2 MeV is questionable. For each line the content was determined (second column) and the relative cross section with respect to the ^{37}S line at 646 keV was determined. An absolute cross section of 230 mb, the value of the first method, was assumed for the 646 keV line, as the errors of the value obtained from the second method were too large. Finally absolute cross sections were derived for all γ-lines observed (last column).

While the cross sections $\sigma_\gamma(E_\gamma)$ for the occurrence of a γ-ray at a certain energy E_γ are directly accessible in γ-ray spectroscopy measurements the relevant spectroscopic data is the cross section $\sigma_E(E)$ to directly populate certain excited levels of a nucleus. Both kinds of cross sections are linked by the branching ratios for the different deexcitation channels of a certain excited state. While the branching ratios for the decay of excited states of ^{37}S populated in this experiment are already known, information about the level scheme and the branching ratios of unknown nuclei investigated in REX-ISOLDE experiments have to be

E_γ [keV]	$N_{\gamma-\text{observed}}$	reaction & transition	$\frac{\sigma_\gamma(E)}{\sigma_\gamma(646)}$	$\sigma_\gamma(E_\gamma)$[mb]
646(1) (*646*)	19500 (5%)	$^{37}S : 3/2^-_1 \rightarrow 7/2^-_{gs}$	1	230(46)
(*751*)	<500	$^{37}S : 3/2^+_1 \rightarrow 3/2^-_1$	<3%	<5
1347(3) (*1346*)	1000 (40%)	$^{37}S : 3/2^-_2 \rightarrow 3/2^-_1$	8%	20(10)
(*1377*)	<400	$^{37}S : 7/2^-_1 \rightarrow 3/2^-_1$	<3%	<5
1993(2) (*1992*)	3100 (10%)	$^{37}S : 3/2^-_2 \rightarrow 7/2^-_{gs}$	29%	65(15)
doublet		$^{37}S : 1/2^-_1 \rightarrow 3/2^-_1$		
(*2023*)	<300	$^{37}S : 7/2^-_1 \rightarrow 7/2^-_{gs}$	<3%	<5
1727(3) (*1727*)	1800 (20%)	$^{37}Cl : 1/2^+_1 \rightarrow 3/2^+_{gs}$	16%	35(10)
3101(5) (*3086*)	3200 (10%)	$^{37}Cl : 5/2^+_1 \rightarrow 3/2^+_{gs}$	45%	105(25)
doublet (*3103*)		$^{37}Cl : 7/2^-_1 \rightarrow 3/2^+_{gs}$		
3748(10) (*3741*)	300 (50%)	$^{37}Cl : 5/2^-_1 \rightarrow 3/2^+_{gs}$	5%	10(5)
890(1) (*889*)	6800 (8%)	$^{46}Ti : 2^+_1 \rightarrow 0^+_{gs}$	85%	200(45)
1049(3) (*1049*)	800 (40%)	$^{46}Ti : 3^-_1 \rightarrow 4^+_1$	11%	25(10)
1122(1) (*1121*)	5500 (10%)	$^{46}Ti : 4^+_1 \rightarrow 2^+_1$	77%	180(40)
1289(2) (*1289*)	1900 (20%)	$^{46}Ti : 6^+_1 \rightarrow 4^+_1$	28%	65(20)

reactions: ^{37}S – $^{2}H(^{36}S,^{37}S)p$, ^{37}Cl – $^{2}H(^{36}S,^{37}Cl)n$, ^{46}Ti – $^{12}C(^{36}S,^{46}Ti2n)$

Table 5.1: Strongest γ-lines detected in the reaction $^{36}S \longrightarrow CD_2$ at an energy of 2.2 MeV·A. One MINIBALL germanium module at ϑ_{det}=91° was used for the measurements. The data were taken in a 9 hour beamtime with a current of 40 pA (electrical, corresponding to $3 \cdot 10^7$ pps).
In the first column the energies extracted from Doppler-corrected spectra are compared with the literature values (in parenthesis). For the Doppler correction the appropriate kinematics were applied (see third column). The 1992 keV transition in ^{37}S is a "real" doublet, the ^{37}Cl transition with energies of 3086 keV and 3103 keV are located too close together to be completely resolved. Three possible ^{37}S lines, which were not observed in this measurement, are included in the Table. For each γ-line the content of the peak was determined (second column) permitting the determination of relative cross sections (fourth column). As the absolute cross section for the occurrence of the 646 keV line of ^{37}S was determined experimentally, it was possible to calculate absolute cross sections for all γ-rays observed (fifth column, values rounded to multiples of 5).

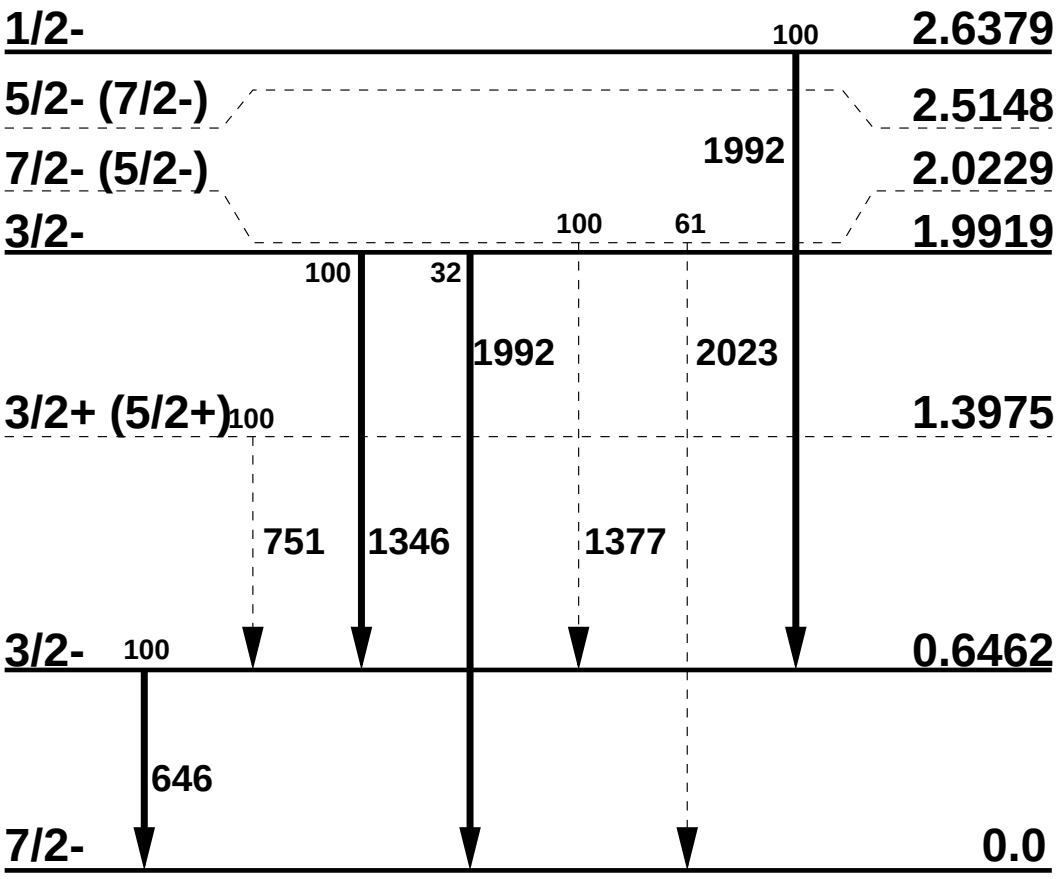

Figure 5.13: Level scheme of ^{37}S[Fir96]. γ-transitions detected in the experiment are marked with thick arrows.

E_{level}[keV]	spin	$\sigma_{\mathrm{exp.}}$[mb]	$\sigma_{\mathrm{theo.1}}$[mb]	$\sigma_{\mathrm{theo.2}}$[mb]
646	$3/2^-$	150(49)	180	105
1992	$3/2^-$	25(11)	-	-
2638	$1/2^-$	60(16)	95	75

Table 5.2: Comparison of the experimental and calculated [Len98b] cross sections for the population of the $(3/2)^-$ and $(1/2)^-$ states in ^{37}S, which are dominated by $2p_{3/2}$ and $2p_{1/2}$ single neutron configurations, respectively.

extracted from the measurement (relative intensities, angular distributions, γ-γ-coincidences, γ-γ-angular correlations and so on).

With the aid of the level scheme and the branching ratios of ^{37}S (see Figure 5.13) it has been possible to calculate the population cross sections. The population of three negative parity low spin levels has been observed: The cross section for the population of the second $(3/2)^-$ level can be directly derived from the cross section of the γ-line at 1346 keV and the known branching ratio. For the cross section of the $(1/2)^-$ level, the population of the second $(3/2)^-$ level needs to be known, as the γ-line at 1992 keV is a doublet. In order to determine the direct population cross section of the first excited state, the $(3/2)^-$ level at 646 keV, the feeding from the $(1/2)^-$ and the $(3/2)^-_2$ level has to be subtracted from the total cross section to observe the 646 keV γ-line.

The absolute cross section for the population of the $(3/2)^-_1$-level at 646 keV is 150(49) mb, for the $(3/2)^-_2$-level at 1992 keV it is 25(11) mb and for the $(1/2)^-$ level at 2638 keV it is 60(16) mb. A summary of the cross sections is compiled in Table 5.2. The two states which are most strongly populated correspond to the ^{36}S core plus a single neutron in the $2p_{3/2}$ and $2p_{1/2}$ shell, respectively. As expected, neutron pickup reactions on the deuteron target mainly populate single particle states. A simple classical estimate, which assumes a ^{36}S-nucleus, a single neutron, and a relative velocity corresponding to an energy of 2.2 MeV$\cdot A$, reveals that the most probable angular momentum transfer is $1\hbar$. Hence, transfer to excited states with high orbital angular momentum is suppressed; as a consequence the population of the $1f_{5/2}$ and $1f_{7/2}$ single neutron states has not been observed.

The measured cross sections were compared with the theoretical predictions by Lenske [Len98b]. Skyrme-Hartree-Fock calculations were used to derive the nuclear structure of the nuclei. The results were used to obtain transfer probabilities using the Distorted-Wave-Born-Approximation (DWBA) and the Exact-Finite-Range-Distorted-Wave-Born-Approximation (EFR-DWBA). When the level energy was used as a free parameter of the theoretical model cross sections of $\sigma(3/2_1^-) = 180$ mb and $\sigma(1/2^-) = 95$ mb were calculated, whereas cross sections of $\sigma(3/2_1^-) = 105$ mb and $\sigma(1/2^-) = 75$ mb were found when the level energies were fixed at their experimental values.

For the calculations of the experimental cross sections an isotropic angular distribution of the γ-rays emitted from the excited nucleus has been assumed. While this assumption is always true for J=(1/2) states, the same applies for the $(3/2)_1^-$ level only, if all m-substates are equally populated. Although the differential cross sections to populate the |m|=1/2 states and the |m|=3/2 states differ significantly, as can be seen in Figure 5.2 on page 105, the absolute probabilities to populate these substates are 48 % and 52 % respectively and the angular distribution of the emitted γ-rays deviates by less than 1% from an isotropic distribution. Even if one assumed complete alignment, the deviation would be less than 14%.

Two different methods have been presented to determine absolute cross sections for the observation of a γ-ray, they were applied to the first excited state of ^{37}S at 646 keV. Relative cross sections for the occurrence of weaker γ-lines were calculated using a spectrum with high statistics; with the aid of the known absolute cross section for the line at 646 keV absolute cross sections for all γ-lines could be deduced. The absolute cross sections for the population of excited states in ^{37}S were derived from the cross section to detect a γ-ray at a certain energy using the known level scheme and branching ratios of ^{37}S. Finally the measured cross sections for the population of the $(3/2)_1^-$-level at 646 keV and the $(1/2)^-$-level at 2638 keV were compared with theoretical predictions and a good agreement was found.

In REX-ISOLDE experiments the low beam intensities will not allow high intensity runs to obtain relative cross sections, the absolute cross sections for all γ-lines will be derived directly. As the MINIBALL array allows an almost isotropic detection of the γ-rays, the population of m-substates does not have to be known

to determine absolute cross sections for the occurrence of γ-lines, however, the level scheme and branching ratios of the investigated nucleus will be unknown and have to be deduced together with the population cross sections of excited states. For this task lifetime measurements, angular distribution measurements, γ-γ-angular correlation measurements, and particle-γ-angular correlation measurements will be available to permit a determination of the details (energy, spin, parity, lifetime) of the excited states.

5.5 ^{9}Be Induced Transfer

In contrast to the deuterium target, where both the neutron and the proton transfer channel are observed, the beryllium target allows to distinguish between these reaction channels, as the proton transfer is suppressed. However, ^{9}Be exhibits two significant disadvantages. In the germanium spectrum, Figure 5.14, which is Doppler corrected for the single neutron transfer kinematics with neglected scattering angle of the heavy reaction product (mean β=0.056), the large number of peaks indicates that there are several other reaction channels apart from ^{9}Be(^{36}S,^{37}S)^{8}Be. Furthermore ^{9}Be is significantly heavier than deuterium and the reaction products are deflected by a larger angle and lose more energy (compare with Figure 5.1 on page 104), so that only a moderate Doppler correction can be achieved without particle tracking, as neither the reaction nor the kinematics are known; for instance for the 646 keV line of ^{37}S an energy resolution of 11.5 keV is obtained.

As shown in Figures 5.15/5.16, the silicon ΔE-E detector is a major aid to identify different reaction channels. It is possible to distinguish between the neutron pickup and several break-up and fusion evaporation channels.

In Figure 5.16 the Doppler-corrected germanium spectra for different particle gates in the telescope detector are depicted. For the Doppler correction the kinematics were calculated using the known direction and identity of the light reaction product. The particle identification allowed to assign a reaction. (e.g. ^{9}Be(^{36}S,^{44}K)p, the evaporation of neutrons is not included in the kinematic calculations). Here the well defined scattering angle of the two αs from the ^{8}Be decay allowed an energy resolution of 7.0 keV for the ^{37}S-line at 646 keV.

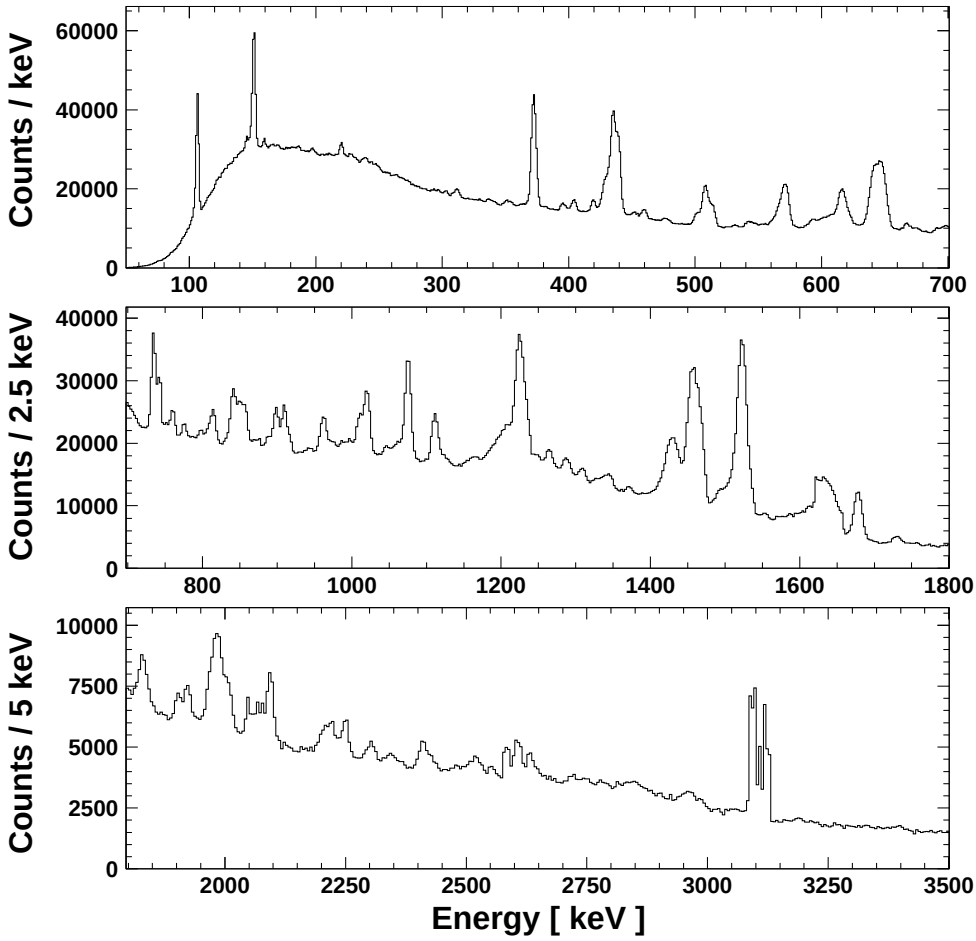

Figure 5.14: Doppler-corrected γ-single spectrum of the ^{36}S$\longrightarrow^{9}$Be reaction at 2.2 MeV$\cdot A$. For the Doppler correction the single neutron transfer kinematics were used and the scattering angle of the heavy reaction product was neglected (mean β=0.056). The spectrum was taken in 8 hours beamtime at a beam current of 800 pA (electrical, corresponding to $6\cdot10^{8}$ pps) with two germanium detectors, one detector covering the low energy range from 0 to 1.6 MeV, one covering a wider range from 0 to 4 MeV. The PPAC was covered by the shutter.

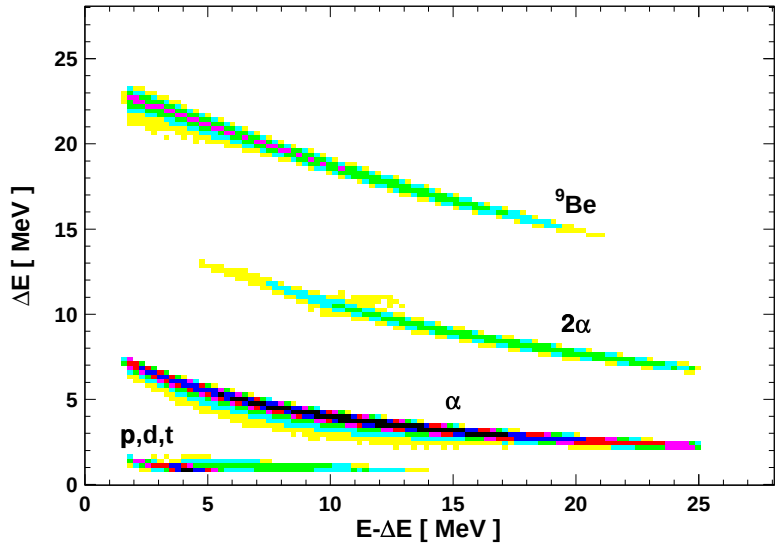

Figure 5.15: ΔE-E spectrum of the silicon telescope detector for the ^{36}S⟶^{9}Be reaction at 2.2 MeV·A. Different light reaction products can be identified.

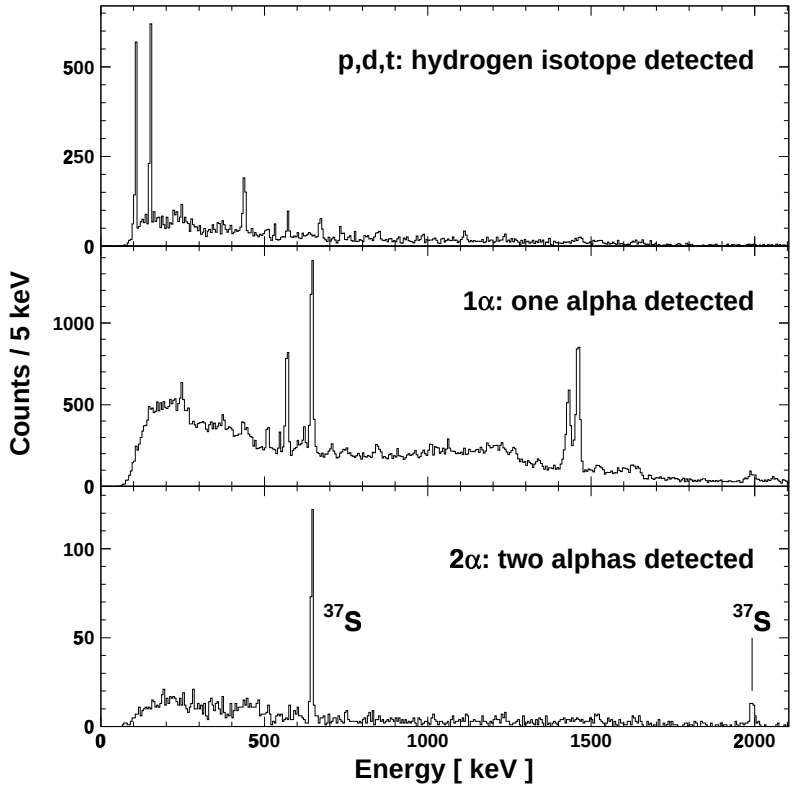

Figure 5.16: Doppler-corrected telescope-gated γ-spectra of the ^{36}S⟶^{9}Be reaction at 2.2 MeV·A. For the Doppler correction the full kinematic information of the light particle scattering angle and identity is used (see text). The γ-lines corresponding to different reaction channels can be assigned by selecting different gates on light reaction products (see text).

In panel 1 of Figure 5.16 it is shown that a telescope gate on hydrogen isotopes yielded several γ-transitions mainly at low energies which could be assigned to potassium isotopes. When a gate on one α-particle was set, γ-rays of argon isotopes and of ^{37}S occurred. It was necessary to detect both αs originating from the ^{8}Be decay to exclusively select the ^{37}S neutron-pickup channel. The remaining γ-transitions not shown in the gated spectra could be assigned to calcium isotopes from the fusion evaporation channel. As no ^{8}Li was detected in the silicon telescope detector and no γ-lines were observed, which could be assigned to chlorine isotopes, it was concluded that the proton-transfer channel was too weak to be measured.

An overview of the strongest γ-transitions observed is given in Table 5.3. For the Doppler correction the appropriate kinematics were applied. If applicable, the measured energy values were extracted from the telescope-gated spectra. As the detector shift was included in the Doppler correction, all measured energies agree well with the literature values [Fir96]. For prominent lines the error is determined by the positioning uncertainty of the detector module, a larger error for smaller lines reflects the difficulty to exactly locate these lines in the spectrum.

It is interesting to note, that the ^{43}K line at 738 keV has a long halflife of 200 ns. As the beam particles travel about 2 cm/ns, the line is only visible as a *sharp* peak, when no Doppler correction is applied and the PPAC is *covered* with the shutter. This also proves that the beam particles are not stopped in the PPAC. Furthermore the measured energies of γ-lines with a halflife of $\sim$1ns are all lower than their literature values. Here the assumption that the γ-ray is emitted close to the target is no longer true, so that the Doppler correction yields too small values. For REX-ISOLDE the population of excited states with a long lifetime (>200 ps) will pose similar problems and the use of a shutter will not be possible as the beam particles would accumulate on the shutter and create an enormous β-background.

As the beryllium target had no gold backing and no low intensity measurements with the PPAC were performed when the beryllium target was used, it was not possible to calculate absolute cross sections for the ^{9}Be(^{36}S,^{37}S)^{8}Be reaction, however the relative cross sections for the production of the different nuclei populated in the ^{36}S$\longrightarrow^{9}$Be reaction were determined (Figure 5.17).

E_γ[keV]	part. gate	Reaction & Transition	$T_{\frac{1}{2}}$[ps]	$\frac{\sigma_\gamma(E)}{\sigma_\gamma(646)}$[%]
106(1) (*107*)	p,d,t	$^{42}K : 3^-_1 \rightarrow 2^-_{gs}$	285	≈20
151(1) (*151*)	p,d,t	$^{42}K : 4^-_1 \rightarrow 3^-_1$	130	18
248(3) (*250*)	1α	$^{39}Ar : 3/2^+_1 \rightarrow 3/2^-_1$	950	2
373(1) (*373*)	-	$^{43}Ca : 5/2^-_1 \rightarrow 7/2^-_{gs}$	33	40
439(1) (*441*)	p,d,t	$^{42}K : 5^-_1 \rightarrow 4^-_1$	41	51
570(1) ((*572*)	1α	$^{40}Ar : 6^+_1 \rightarrow 4^+_1$	680	39
646(1) (*646*)	1α, 2α	$^{37}S : 3/2^-_1 \rightarrow 7/2^-_{gs}$	-	100
673(5) (*677*)	p,d	$^{42}K : 6^+_1 \rightarrow 5^-_1$	1100	5
738(1) (*738*)	p	$^{43}K : 7/2^-_1 \rightarrow 3/2^+_{gs}$	$2{\cdot}10^5$	27
1021(3) (*1022*)	-	$^{43}Ca : 5/2^+_1 \rightarrow 5/2^-_1$	2.4	14
1077(2) (*1076*)	-	$^{43}Ca : 15/2^-_1 \rightarrow 11/2^-_1$	24	31
1114(3) (*1112*)	p	$^{43}K : 11/2^-_1 \rightarrow 7/2^-_1$	4.6	16
1228(2) (*1228*)	-	$^{42}Ca : 4^+_1 \rightarrow 2^+_1$	3.0	31
1266(4) (*1267*)	1α	$^{39}Ar : 3/2^-_1 \rightarrow 7/2^-_{gs}$	<500	5
1431(2) (*1432*)	1α	$^{40}Ar : 4^+_1 \rightarrow 2^+_1$	2.4	54
1460(2) (*1461*)	1α	$^{40}Ar : 2^+_1 \rightarrow 0^+_{gs}$	1.1	101
1525(2) (*1525*)	-	$^{42}Ca : 2^+_1 \rightarrow 0^+_{gs}$	0.82	86
1681(3) (*1679*)	-	$^{43}Ca : 11/2^-_1 \rightarrow 7/2^-_{gs}$	1.0	32
1992(3) (*1992*)	1α, 2α	$^{37}S : 3/2^-_2 \rightarrow 7/2^-_{gs}$	-	20
doublet		$^{37}S : 1/2^-_1 \rightarrow 3/2^-_1$		

reactions: ^{37}S – $^{9}Be(^{36}S,^{37}S)2\alpha$, ^{39}Ar – $^{9}Be(^{36}S,^{39}Ar)\alpha 2n$
^{40}Ar – $^{9}Be(^{36}S,^{40}Ar)\alpha n$, ^{42}K – $^{9}Be(^{36}S,^{42}K)p2n,^{2}Hn,^{3}H$,
^{43}K – $^{9}Be(^{36}S,^{43}K)pn$, ^{42}Ca – $^{9}Be(^{36}S,^{42}Ca3n)$, ^{43}Ca – $^{9}Be(^{36}S,^{43}Ca2n)$

Table 5.3: Strongest γ-transitions detected in the reaction $^{36}S \longrightarrow {}^{9}Be$ at an energy of 2.2 MeV·A. Two MINIBALL germanium modules at ϑ_{det}=91° and ϑ_{det}=93° were used for the measurements. The data were taken in 8 hours of beamtime with a current of 800 pA (electrical, corresponding to $6{\cdot}10^8$ pps).
In the first column the energy extracted from Doppler-corrected spectra is compared with the literature values (in parenthesis). For the Doppler correction the appropriate kinematics were applied, except for the ^{43}K-line at 738 keV, which was extracted from an uncorrected spectrum (see text). In the second column the particle gates to select certain reaction channels are depicted. The excited state corresponding to the measured γ-energy can be obtained from the third column [Fir96]. The halflife and the relative cross section to observe the γ-ray are shown in the fourth and fifth columns, respectively.

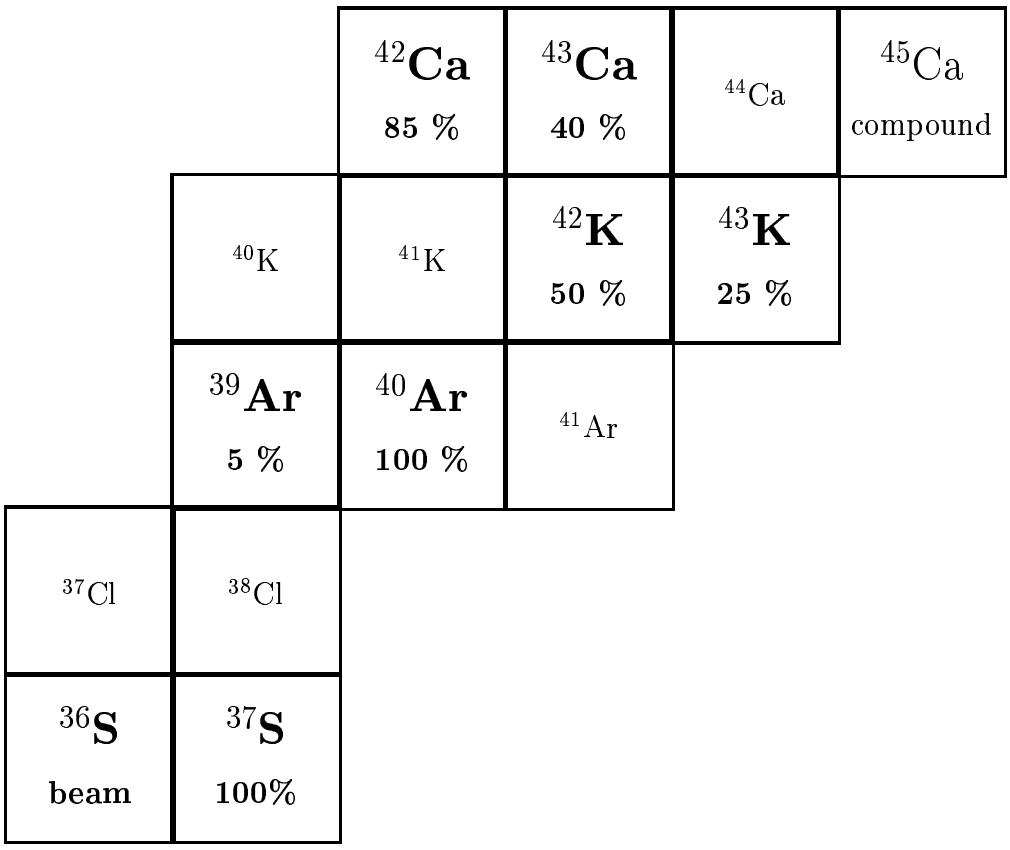

Figure 5.17: Relative population probabilities of the reaction ^{36}S$\longrightarrow^{9}$Be at an energy of 2.2 MeV·A. The probability to populate ^{37}S is set to 1. The nuclei with faint letters have not been observed (relative population probability below 2%).

The fusion-evaporation channel is the strongest channel leading mainly to ^{42}Ca and ^{43}Ca. The α-emission channel is only slightly weaker; ^{40}Ar and a small amount of ^{39}Ar are produced. The third strongest channel is the neutron-pickup leading to ^{37}S. Two potassium isotopes (^{42}K,^{43}K) are produced in an incomplete fusion reaction (^{2}H, ^{3}H observed in the silicon telescope).

A large variety of reaction channels was observed when the ^{9}Be target was used. Due to the the large unknown scattering angle of the heavy reaction product a Doppler correction without particle detection proved to yield only moderate results. A silicon telescope detector was needed to identify the light reaction product. The detection of the light particle allowed to distinguish between different reaction channels. Furthermore the kinematics could be calculated, so that an improved Doppler correction was obtained. With the aid of the telescope detector several break-up, incomplete-fusion and fusion-evaporation channels besides the neutron transfer to ^{37}S were identified leading to argon, potassium and calcium isotopes. As expected the proton-transfer channel was too weak to be observed. In the measurement the problem of long lifetimes of excited states was encountered. For lifetimes above 200 ps the assumption that the γ-ray is emitted close to the target is no longer true, so that the width of the Doppler-corrected γ-line is broadened and shifted. If the lifetime exceeds $\sim$10 ns, a considerable amount of excited nuclei emit their γ-ray after leaving the target chamber.

The experimental setup of REX-ISOLDE is prepared for the use of beryllium targets. A large annular silicon telescope detector will be available permitting the necessary particle identification and sufficient Doppler correction. The beryllium target will be used for two reasons: As the proton-transfer channel is strongly suppressed, when a beryllium target is used, it is possible to distinguish between the neutron and proton transfer channel. For measurements of differential cross sections the large scattering angle of the heavy reaction product will be an advantage of the beryllium target.

Chapter 6

Conclusions

6.1 MINIBALL

The design goals of the MINIBALL γ-ray spectrometer have been presented. It has been explained how they can be deduced from the requirements of γ-ray spectroscopy experiments at ISOL-type radioactive beam facilities with beam energies of up to 5 MeV$\cdot A$. For such experiments an extremely high full-energy-peak efficiency and a high granularity for Doppler correction is needed, while only a moderate γ-ray multiplicity has to be handled. The arrangement of the array has to be kept as flexible as possible to allow for different experimental setups. Furthermore the compatibility with EUROBALL Cluster modules is required to keep new development work at a minimum and to allow a combination of both germanium arrays.

A six-fold segmentation of the initial EUROBALL module together with new sampling electronics that permit pulse-shape analysis (PSA) of the core and the segment pulses has been adopted as the best method to improve the detector granularity while maximizing the full-energy-peak efficiency of a close geometry. Three segmented modules will be operated in an aligned 3-Cluster cryostat to obtain additional efficiency by addback. A four-module cryostat is under development.

In order to simulate the properties of the new detector module and the cryostat a set of simulation tools has been developed. The first tool which is based on the GEANT code delivers the energy deposition of the γ-rays in the detector material for the desired experimental setup. The second tool is used to calculate electric

fields and weighting potentials within the detector. The third tool calculates the detector pulses and emulates the data acquisition electronics, so that simulated pulse samples with a sampling time of 25 ns can be obtained. Various data analysis programs have been used to extract the desired information from simulated data. Whenever possible, the simulations have been verified by measurements.
The GEANT simulations predict a full-energy-peak efficiency of 20% at $E_\gamma = 1$ MeV and 17% at $E_\gamma = 1.3$ MeV when an array of 14 aligned 3-Clusters is used in addback mode. Without addback efficiencies of 17% and 14% respectively are expected. The values without addback have been verified in an experiment with calibrated γ-sources.
In order to determine the granularity of the MINIBALL module the concept of first interaction and main interaction has been introduced. It can be shown that for a wide range of γ-energies there is a high probability that the first interaction and the main interaction are located very close together or even coincide. For the remaining energies the angular deviation between the direction from the target to the main interaction and the direction of γ-emission is usually small enough, so that an acceptable Doppler correction remains possible. The main interaction dominates the shapes of the detector pulses and can therefore be located more easily than any other interaction. In consequence, a very good physical limit of the granularity can be predicted for γ-energies below 200 keV and above 600 keV, in-between a moderate granularity has to be expected.
As the current MINIBALL modules are not segmented in z-direction, a 3-dimensional position determination of the main interaction is impossible, so that the physical limit of the granularity cannot be reached. Instead one tries to determine the radius and the angle with respect to a given reference depth.
The segmentation is the most important measure to enhance the granularity of the MINIBALL module, without the segmentation there is no angular information at all and the radius determination is meaningless. The basic angle algorithm that is only based on the energy information of the segments already reduces the width of a Doppler-corrected γ-line by more than a factor of 2. A further significant improvement of the angle algorithm can be achieved by segment PSA. The radial resolution is obtained by PSA of the core contact signal. The steepest-slope algorithm can provide a considerable radial resolution even at medium energies

between 200 keV and 600 keV, the resolution improves for larger energies. As the arc-length resolution remains almost constant at energies above 1 MeV and the radial resolution declines, a reduction of the Doppler-shift related width of the relative energy resolution is expected for larger γ-energies.

The MINIBALL detector modules will be mounted in aligned 3-Cluster cryostats, which are a compromise between efficiency and granularity. The efficiency improvement by addback has to be paid for by a more difficult position determination, since the modules' centrelines do not point at the target, so that the segmentation lines appear to be displaced and smeared out. As a result the correlations between the time-to-steepest-slope and the γ-ray entry radius differ for different segments. It is therefore necessary to relate the radius and angle determination to the position, where the initial γ-ray direction penetrates the reference plane $z_{\mathrm{ref}} = \langle z_1(E_\gamma) \rangle$. The radius and angle algorithms then become independent of each other and the radial and arc-length resolution is optimized. Nevertheless the resolutions cannot quite match the corresponding resolutions of a single module pointing at the target.

A Doppler-shift related contribution to the relative energy resolution of less than $0.1 \times \beta$ is a design goal for MINIBALL. This limit would only be exceeded, if an inverse reaction on a very light target was investigated, all detector modules were put in aligned 3-Cluster cryostats, and all cryostats were positioned at the most unfavourable detection angle ϑ_{det}=90°. It is important to note that $0.1 \times \beta$ corresponds to an accuracy of the angle determination between the flight direction of the nucleus and the direction of γ-emission of $\pm 3°$. In order to fully exploit the excellent granularity and high energy resolution of MINIBALL it is therefore essential to determine the flight direction of the γ-emitting nucleus with an accuracy of at least $\pm 2°$.

The radius and angle algorithms presented permit sufficient angular and radial resolution. The aim is to keep these algorithms as simple as possible so that they need little processing time and can be implemented on either the FPGA or the DSP of the XIA-module. This implementation is in progress in order to have the algorithms available for online-processing on the XIA-module for the first measurement campaigns.

With the implementation the development of angle and radius algorithms is not

ended. The improved computing power of expected future electronics modules will allow the use of better algorithms, which can then have a higher complexity. While there have been several tests of single MINIBALL modules, test measurements with calibrated and collimated sources are still necessary for the aligned 3-Cluster, in order to determine and document the properties of this new detector system.

6.2 The REX-ISOLDE Test Experiment

An in-beam experiment was performed to test the MINIBALL germanium modules in conjunction with the REX-ISOLDE PPAC in a real experimental setup and to compare theoretical cross section predictions for single-neutron transfer reactions with experimental data.

Two single modules of the MINIBALL germanium array were used. In the measurements only standard electronics, which did not permit segment PSA, were available. After Doppler correction the relative energy resolution of the segmented germanium detector was found to be $< 1\%$ for a velocity β=0.065 at a target distance of $d_{\mathrm{target}} = 10.6$ cm, even though the detectors were placed at the most unfavourable angle ϑ_{det}=90°, which corresponded to $\theta_\gamma \approx 90°$. This was an improvement of the line width by more than a factor of 2 as compared to a module without segmentation and when no PSA is used. In a simulation without segment PSA the line widths of the experiment were reproduced.

The new position-sensitive REX-ISOLDE PPAC delivered a time reference signal for particle-γ-coincidence measurements allowing to perform γ-spectroscopy at very low rates. The γ-rays detected without a beam particle were rejected, so that the peak-to-background ratio became independent of the beam particle rate. Furthermore the PPAC allowed to count individual beam particles up to a rate of 10^6 particles/sec. Hence an easy method to determine absolute cross sections was available. As the efficiency of the PPAC affected the scaler which counted the particles and the coincidence unit equally, the method was also independent of the PPAC efficiency.

Neutron-pickup, proton-pickup and a fusion-evaporation reaction with ^{12}C were

observed when a CD_2 target was used. Due to different γ-line shapes it was possible to distinguish between fusion and pickup. The identification of the n-pickup channel required either knowledge of the p-transfer product or the comparison with a measurement with a ^{9}Be target or the detection of the proton. Two models were used to predict the n-pickup cross section of the first excited state of the ^{2}H(^{36}S,^{37}S)p reaction. The model, which used the level energy as a free parameter, yielded 180 mb, whereas the model, where the level energy was fixed to its experimental value, yielded 105 mb. An experimental value of 150(49) mb was observed.

The ^{9}Be target gives complementary information about the neutron-pickup reaction. In addition several other nuclei are populated. It is very helpful to have a silicon telescope available to detect the light reaction product and to distinguish between the different reaction channels.

The in-beam experiment together with the simulations, proven by experimental tests, has confirmed that it is possible to investigate exotic nuclei at REX-ISOLDE using pickup reactions and the MINIBALL γ-ray spectrometer. When MINIBALL is fully set up and a CD_2 target with an areal density of 0.5 mg/cm^2 is used, it will take 20 hours to accumulate 400 counts in a first excited level at 1 MeV assuming a particle rate of 10^4 particles/sec, an absolute cross section of 100 mb, and a full MINIBALL efficiency of 14%.

In the first REX-ISOLDE test experiment only parts of the REX-ISOLDE detector and data acquisition system have been used. In a second test experiment, the functionality of all detector systems and electronics will be tested at Köln. The energy resolution after Doppler correction and the overall efficiencies will be measured and the whole system will be optimized allowing a fast transition to ISOLDE at CERN.

The feasibility of γ-ray spectroscopy experiments with extremely low-intensity beams has been demonstrated. The background suppression by time coincidences allows to separate the γ-transitions from background; theoretical calculations can give estimates about the excitation energies and cross sections. It is important to note, that the quality of these predictions will decline considerably for nuclei far-off the valley of stability, unless the experimental results obtained are immediately reincluded in the theoretical models. As the theoretical predictions

will influence the predicted beam time requirements and the experimental results will influence the models, a close cooperation between theory and experiment is necessary for REX-ISOLDE to achieve the greatest success possible.

Bibliography

[CERN93] CERN Application Software Group
GEANT 3.21 - Detector Description and Simulation Tool, CERN, Genf, 1993

[Cub99] J. Cub et al.
A Position Sensitive PPAC for Single-Particle and Current Readout, Nucl. Instr. & Meth. A, to be published

[Deb88] K. Debertin and R.G. Helmer
Gamma- and X-ray Spectrometry with Semiconductor Detectors, North Holland Publishing Company, Amsterdam, 1988

[Dru71] W.E. Drummond and J.L. Moll
Hot Carriers in Si and Ge Radiation Detectors, Jour. of Appl. Phys., volume 42, No 13, 1971, page 5556

[Ebe97] J. Eberth et al.,
Development of segmented Ge detectors for future gamma-ray arrays, Prog. in Part. & Nucl. Phys., volume 38, 1997, page 29

[Gut96] D. Gutknecht (EURISYS MESURES),
Impurity concentrations of the detector crystals, private communication, 1996

[Fir96] R.B. Firestone (editor)
Table of Isotopes, John Wiley & Sons, New York 1996

[Fis97] C. Fischbeck
Untersuchungen zum Ansprechverhalten des sechsfach segmen-

tierten MINIBALL Ge-Detektors, Diplomarbeit, LMU München, München, 1997

[Gro94] Ch. Großmann and H.-G. Roos
Numerik partieller Differentialgleichungen, Verlag B.G. Teubner, Stuttgart, 1994

[Gun97] C. Gund
Eigenschaften des zweifach segmentierten Prototypen eines MINIBALL Cluster Moduls, Diplomarbeit, Max-Planck-Institut für Kernphysik, Heidelberg, 1997

[Hab94] D. Habs et al.
Radioactive Beam Experiments at ISOLDE: Coulomb excitation and neutron transfer reactions of exotic nuclei. REX-ISOLDE, CERN ISC 94-25; ISC P 68,

[Hac93] W. Hackbusch
Iterative Lösung großer schwachbesetzter Gleichungssysteme, Verlag B.G. Teubner, Stuttgart, 1993

[Hun92] S. Hunklinger
Einführung in die Festkörperphysik, Vorlesungsskript (reprint), Universität Heidelberg, Heidelberg, 1992

[Jac81] C. Jacobini et al.
Electron drift velocity and diffusivity in germanium, Phys. Rev. B, volume 24, No 2, 1981, page 1014

[Jac83] J.D. Jackson
Klassische Elektrodynamik, 2nd edition, Verlag Walter de Gruyter, Berlin, 1983

[Kno89] G.F. Knoll
Radiation detection and measurement, John Wiley & Sons, New York, 1989

[Käp98] F. Käppeler et al.
Current Quests in Nuclear Astrophysics and Experimental Approaches, Annu. Rev. Nucl. Part. Sci., volume 48, 1998, page 175

[Len98a] H. Lenske and G. Schrieder
Probing the structure of exotic nuclei by transfer reactions, Eur. Phys. Jour. A, volume 2, No 1, 1998, page 41

[Len98b] H. Lenske
Neutron-transfer cross sections for the ^{2}H(^{36}S,^{37}S)p *reaction*, private communication, 1998

[Mih98] L. Mihailescu
The importance of the crystal orientation in HPGe detectors for gamma-ray tracking, TMR User meeting on Gamma-Ray Tracking detectors, Padova, Oct. 1998

[Muk76] T. Mukoyama
Range of Electrons and Positrons, Nucl. Instr. & Meth., volume 134, 1976, page 125

[Neu73] A. Neukermans and G.S. Kino
Measurement of the Electron Velocity-Field Characteristics in Germanium using a New Technique, Phys. Rev. B, volume 7, No 6, 1973, page 2693

[Pal97] L. Palafox
A New Method for the Determination of the Entry Position of γ-rays in HPGe Detectors by Current Pulse Analysis, PhD thesis at Max-Planck-Institut für Kernphysik and Cranfield University, Heidelberg/Cranfield, 1997

[Rau82] T.W. Raudorf et al.
Pulse shape and risetime distribution calculations for HPGe coaxial detectors, IEEE Trans. on Nucl. Sci., volume 29, No 1, 1982, page 764

[Reg76] L. Reggiani
The Anisotropy of the Hot-Hole Drift Velocity in Ge, Jour. Phys. Chem. Solids, volume 37, 1976, page 293

[Reg77] L. Reggiani et al.
Hole drift velocity in germanium, Phys. Rev. B, volume 16, No 6, 1977, page 2781

[Reik62] H.G. Reik and H. Risken
Drift velocity and Anisotropy of Hot Electrons in n-Germanium, Phys. Rev. volume 126, No 5, 1962, page 1737

[Sas56] W. Sasaki and M. Shibuya
Experimental Evidence of the Anisotropy of Hot Electrons in n-type germanium, Jour. Phys. Soc. Japan, volume 11, 1956, page 1202

[Sie65] Kai Siegbahn (editor)
Alpha-, Beta-, and Gamma-Ray Spectroscopy, volume 1, North-Holland Publishing Company, Amsterdam, 1965

[Sto90] J. Stoer and R. Bulirsch
Einführung in die numerische Mathematik II, 3rd edition, Springer Verlag, Heidelberg, 1990

[Sze81] S.M. Sze
Physics of Semiconductor Devices, 2nd edition, John Wiley & Sons, New York, 1981

[Tho95] H.-G. Thomas
Entwicklung eines Germanium-Cluster-Detektors für das Gamma-Spektrometer EUROBALL, Verlag Dr Köster, Berlin, 1995

[Wal92] P. von Walter and A. Rausch
A 1 GHz Flash-ADC Module in VMEbus, IEEE Trans. on Nucl. Sci., volume 39, No 4, 1992, page 776

[Wei] D. Weisshaar
PhD thesis, Universität zu Köln, in preparation

[XIA] X-ray Instrumentation Associates
DGF-4C: 4 Channel, High Speed Digital Gamma-ray Spectrometer, USER Manual and Programmer Manual, http://www.xia.com

[Zul70] H.R. Zulliger and D.W. Aitken
Fano Factor Fact and Fallacy, IEEE Trans. on Nucl. Sci., volume 17, No 3, Jun 1970, page 187